EXPERIMENTAL AND COMPUTATIONAL STUDY OF THE PERFORMANCE OF A NEW SHROUD DESIGN FOR AN AXIAL WIND TURBINE

By

Abbas Jarullah Sangoor

Submitted in Partial Fulfillment of the Requirements

for the Degree of

Master of Science

in the

Mechanical Engineering

Program

YOUNGSTOWN STATE UNIVERSITY

MAY, 2015

EXPERIMENTAL AND COMPUTATIONAL STUDY OF THE PERFORMANCE OF A NEW SHROUD DESIGN FOR AN AXIAL WIND TURBINE

By

Abbas Jarullah Sangoor

Signature:

_____

Abbas Jarullah Sangoor, Student Date

Approvals:

_____

Dr. Hazel Marie, Thesis Advisor Date

_____

Dr. Stefan Moldovan, Committee Member Date

_____

Dr. Kyosung Choo, Committee Member Date

_____

Dr. Salvatore A. Sanders, Associate Dean of Graduate Studies Date

ABSTRACT

A new shroud design for horizontal wind turbine was shaped by revolving an airfoil E423 (high lift force) about an axis of symmetry. A lift force is generated by the flow through the shroud, and the effect of this lift is to increase the mass flow rate through the rotor plane. This study found that the efficiency of the augmentation velocity factor is substantially dependent on the shape and geometry of the shroud, particularly the length, angle of attack of airfoil E423, and area ratio. Results obtained from numerical simulation showed that the augmentation velocity factor increases linearly with increasing area ratio and the shroud length. The experimental investigations on an empty micro-shroud, using a low airspeed wind tunnel, showed good agreement with computational fluid dynamics (CFD) of velocity distribution at the throat area and augmentation velocity factor, with error 1.06%. In addition, six different shrouds were modeled with different configurations and analyzed computationally with the aim to understand the influence of the length, angle of attack, and area ratio on power augmentation, and the effects of external loads. This study also investigated experimentally the extracted power on a micro-shroud of an optimized shroud design with an area ratio of 2. Tests confirmed that placing the micro-wind turbine in the throat area of the shroud could strongly improve its performance by factor of 1.7-2.3 times as compared to a wind turbine without shroud. Further, it is shown theoretically that the output power boosts with increasing the area ratio of the shroud, and inlet air velocity. Finally, in order to design the sustainable shrouded wind turbine that would survive an extreme wind gust that is many times greater than normal wind speeds, the drag force effect was analyzed computationally on empty 3-Dimensional shroud models using ANSYS-FLUENT15.

ACKNOWLEDGEMENTS

I would like to express my deepest gratitude to my advisor, Dr. Hazel Marie for her excellent guidance, caring, patience, and providing me with an excellent atmosphere for doing research. I would not have been able to complete my research and experimental work without her. I found her a good person and the most motivating professor I have ever met. She is the funniest advisor and one of the smartest people I know. She is someone you will instantly love and never forget once you meet her. I would like to thank Dr. Hazel for the time she spent editing and proofreading my thesis and helping me to develop better writing. Also, I want to thank her, as the chair of mechanical engineering, for funding and support my laboratory experiments.

My sincere thanks as well goes to Dr. David Spera who is a consulting engineer at Green Energy Technologies Company, for his advice and for answering all my questions during my research.

I would like to thank Dr. Stefan Moldovan and Dr. Kyosung Choo for being on my thesis committee. I am also thankful for Dr. Kyosung Choo's thoughtful responses in computational analysis.

I am grateful for the HCED (Higher Committee Education Development) in Iraq for providing me financial support and giving me an opportunity to achieve a Master of engineering Science degree.

I would like to thank all the people who helped me to complete my experimental work especially Cameron A. Bagheri, an undergrad student. Also, I would like to thank Bharat Yelamanchi, who as a good friend, for helping me in the 3D printer lab. I am thankful for all my cousins and friends in my home city for their support in this

scholarship. Thanks to my friends and roommates for listening, offering me advice, and supporting me through this entire process.

I also place on record, my sense of gratitude to one and all who, directly or indirectly, have lent their helping hand in this venture.

Lastly, thanks to my parents for all the moral support and the amazing chances they have given me over the years. Thanks to my mom for praying for me all the time, and thanks to my brothers and sisters.

TABLE OF CONTECTS

ABSTRACT.....III

ACKNOWLEDGEMENTS..... IV

LIST OF FIGURES X

LIST OF TABLES.....XV

NOMENCLATURE XVII

CHAPTER 1 – INTRODUCTION.....1

1.1 Background 1

1.2 The Traditional Wind Turbine and Its Effect on the Local Environment.....7

1.3 The Shrouded Wind Turbine as a Replacement for Traditional Wind Turbine 7

1.4 Literature review 8

1.5 Scope of Work 17

CHAPTER 2- Methodology Views of the Shroud Design 20

2.1 Lift and Drag Characteristics of the Shroud Design.....21

2.2 The Interrelationship between Drag, Lift Force and Angle of Attack.....22

2.3 The Influence of the Drag Force on SAWT Cost.....24

2.4 Shroud Materials Alternative.....27

2.5 The Kutta Condition Satisfaction of the Shroud Design 28

2.6 Augmentation Factor vs Shroud Area Ratio and Its Length.....30

2.7 Exceeding Betz Limit 32

2.8 Relationship between the Shroud Power Augmentation Factor, Shroud Efficiency, and Shroud Area Ratio.....32

2.9 Geometric Influences on SAWT Performance (inlet, outlet, shroud resistance, blade number…etc.) 34

2.1 Inlet section 34

2.2 Outlet section 36

2.3 Shroud Resistance 37

2.4 The number of the turbine blades 38

CHAPTER 3- Mathematical Modeling of the SAWT Design 40

3.1 Pressure and Velocities inside an Empty Diffuser (Shroud) 42

3.2 Pressure and Velocities inside the Shroud with Presence Axial Turbine (Actuator Disk).....45

3.3 Power and Thrust Expressions for SAWT 47

3.4 Shroud Efficiency 48

3.5 Shroud Efficiency without Actuator Disk Based On CFD Analysis 49

3.6 Axial Momentum Balance and the Forces Acting On the Shroud and Rotor Plane....51

CHAPTER 4- Experimental Modeling.....57

4.1 Wind Tunnel 57

4.1.1 Wind Tunnel Configurations 58

4.1.2 Experimental Apparatus (Preparations and Tools) 60

4.1.2.A Data Acquisition Device 60

4.1.2.B Pitot - static tube and Pressure Sensors 61

4.1.2.C Unit Conversions and Velocity calculations 62

4.1.2.D Turnbuckle and Pitot tube clamps 64

4.1.3 Wind Tunnel Schematic 66

4.2 Measurement of Velocity Distribution inside Wind Tunnel.....66

4.3 Empty Micro-Shroud Experiment.....70

4.3.1 Manufacturing of the Experimental Shroud Model.....70

4.3.2 Experimental Setup and Method.....71

4.3.3 Operating conditions 72

4.4 Micro-Shroud Testing with Existing Small Turbine 73

CHAPTER 5- Computational Analysis of the Shroud E423 Design 76

5.1 Introduction 76

5.2 Governing Equations in CFD 77

5.2.1 Mass and Momentum Conservation Equations 77

5.2.2 Navier –Stokes' Equation for Axisymmetric Analysis 78

5.2.3 Turbulence Modelling – Eddy viscosity 79

5.2.3A. $K-\varepsilon$ (K- epsilon) Turbulence Model 79

5.2.3.B $K-\omega$ (k-Omega) Turbulence Model 80

5.3 Fluent Solver Algorithms 81

5.4 Pressure –Based Solver 82

5.5 Physical Modeling 84

5.6 Geometry of Computational Domain.....87

5.6.1 2-D Geometry of Computational Domain 87

5.6.2 3-D Geometry of Computational Domain 88

5.7 Mesh and Boundary Conditions 88

5.8 Solver Control and Turbulence Model 90

5.9 Scaling (similitude).....92

CHAPTER 6- The Results and Discussion.....94

6.1 Augmentation Factor AF0 and Radial Velocity Distribution Inside the Shroud Throat Area 95

6.2 Back-pressure ratio and radial velocity Distribution at the Exit Plane of the shroud 98

6.3 Pressure Distribution Along and inside the empty Shroud 100

6.4 Drag Force analysis.....102

6.5 Grid Convergence 105

6.6 Mathematical Power Calculations 106

6.7 Results validation (Experimental work) 109

6.7.1 Experimental Velocity Distribution in Throat Area of the Empty Shroud E423 (augmented velocity validation)..... 110

6.7.2 Experimental Measurements of the Extracted Power Using Micro-Shroud Wind Turbine (Power Validation)..... 113

CHAPTER 7- Conclusions and Future Work 116

Conclusions.....116

Recommendations and Future Work 118

References.....119

Appendix A.....126

Appendix B 128

Appendix C 134

Appendix D.....136

LIST OF FIGURES

Figure 1.1 Daniel Halladay's first windmill in 1854.....2

Figure 1.2 Charles Brush's windmill of 1888, used for generating electricity 3

Figure 1.3 Primary worldwide energy sources nonrenewable.....4

Figure 1.4 Map illustrating installed wind generating capacity for U.S. states at end of 2013 6

Figure 1.5 Illustration of the streamlines past the rotor and the axial velocity and Pressure Up- and downstream of the rotor 9

Figure 1.6 Circular control volume around a wind turbine 10

Figure 1.7 Ideal flows through a wind turbine in a diffuser 11

Figure 1.8 AMPAIR 300 Watt 13

Figure 1.9 Wind turbine with a flanged diffuser shroud.....15

Figure 1.10 Power coefficient C_w of the wind-lens turbine with C-type wind-lens (h= 0.1D).....16

Figure 2.1 Shroud E423 configurations.....20

Figure 2.2 Lift coefficient C_l against angle of attack α for airfoil (FX67-K-170).....22

Figure 2.3 Lift and drag coefficients vs angle of attack for airfoil E423.....23

Figure 2.4 Airfoil E423 profile under different angle of attack 24

Figure 2.5 Shrouded wind turbine cost estimates 27

Figure 2.6 Four different types of the flow around an airfoil profile 29

Figure 2.7 E423 airfoil profile at 8.96° of the angle of attack which shows flow streamline over the surface of airfoil 30

Figure 2.8 Augmentation Factor γ on the axis of symmetry for the simulated Geometries 31

Figure 2.9 Shroud power augmentation factor (r) versus the shroud area ratio 34

Figure 2.10 Sections of shroud E423 35

Figure 2.11 Simple shroud designs for wind turbine 35

Figure 2.12 The power coefficient vs tip speed ratio with using different number of turbine blades 39

Figure 3.1 velocity contour of the symmetric shroud E423, 2-Dimention. Separation layers appears only in the trailing edge 42

Figure 3.2 Pressure and velocity relationships in an empty shroud 42

Figure 3.3 Optimal pressure and velocity distribution for SAWT 45

Figure 3.4 Ideal shroud airspeed Amplification without turbine 50

Figure 3.5 illustration of the streamtube passing through a bare wind turbine rotor 51

Figure 3.6 Streamtube passing through the shroud in presence of the actuator disk, and the forces in the system 53

Figure 3.7 Frontal cross sectional area of SAWT E423 55

Figure 4.1 Low speed wind Tunnel at YSU 58

Figure 4.2 Axial Fan (Cincinnati Fan –Size 48, 10 hp) 59

Figure 4.3 LabVIEW software screen (Fan control screen) 59

Figure 4.4 Data Acquisition device (DAQ) 60

Figure 4.5 Experimental apparatus 61

Figure 4.6 LabVIEW diagram 62

Figure 4.7 LabVIEW operating panel 63

Figure 4.8 Experimental tools.....65

Figure 4.9 Multi-mount clamp 65

Figure 4.10 Schematic of the Wind tunnel setup 66

Figure 4.11 Traverse on round and square duct areas.....67

Figure 4.12 Test Sections inside Wind Tunnel 68

Figure 4.13 The pitot tubes installation 69

Figure 4.14 Air velocity distribution at section1 (reverse direction) 69

Figure 4.15 Configurations of the Experimental Shroud Model 70

Figure 4.16 Shroud manufacturing steps 71

Figure 4.17 shroud placed in test section1.....72

Figure 4.18 Pitot static tubes placed inside and outside the shroud.....72

Figure 4.19 Micro-wind turbines 73

Figure 4.20 Three different voltage-current Multi-meters 74

Figure 4.21 Both turbines placed in testing section of the wind tunnel.....75

Figure 5.1 Overall flowchart of fluent solver algorithms 82

Figure 5.2 Flowchart of two pressure-based solver algorithms 83

Figure 5.3 Shroud models (m1, m5, and m6) 85

Figure 5.4 Shroud models (M1, M2, M3, and M4) 85

Figure 5.5 Experimental shroud model (M7-Ex) 86

Figure 5.6 Computational domain and boundary conditions 87

Figure 5.7 3D Fluid domain in ANSYS-FLUENT15 for a portion (60°)

of empty shroud model 88

Figure 5.8 Unstructured triangle mesh with showing layers around the shroud.....89

Figure 5.9 Three-dimensional meshes for a portion (60°) of the empty shroud.....90

Figure 5.10 Solution methos setting 91

Figure 5.11 Illustrate general physics setup, and the boundary conditions monitors.....92

Figure 6.1 Solution calculations show the convergence at 1242 iterations of residual criteria 10^{-6} 95

Figure 6.2 Velocity contour of the Axisymmetric empty shroud E423 of M1 (AR=2) (Inlet velocity 5 m/s) 95

Figure 6.3 Non-dimensional, Radial velocity distributions in the throat shroud section (Empty Shroud).....97

Figure 6.4 Non-dimensional, Air velocity distributions in the exit area of the shroud E423 of the six Models 99

Figure 6.5 Non-dimensional pressure distributions along and inside the empty shroud E423 models in two different positions 100

Figure 6.6 Non-dimensional static pressure distribution over empty shroud E423 models' Surface 101

Figure 6.7 Static pressure contour of the empty shroud model M1.....102

Figure 6.8 Comparison of the empty shroud drag coefficient against angle of attack ...103

Figure 6.9 Drag coefficient of empty shroud against area ratio**,** for the six Models 104

Figure 6.10 The shroud length ratio versus the empty drag coefficient of the M1, M5, and M6 105

Figure 6.11 Output power versus different inlet air velocities for the six models and bare wind turbine.....108

Figure 6.12 Power coefficients of six models versus different induction factors a 109

Figure 6.13 Experimental results of the air velocity distribution in radial distance inside the experimental model M7_EX.....110

Figure 6.14 Validation of the simulation (CFD Vs Experimental results) 111

Figure 6.15 Plot of the velocity at the throat area of the shroud against the radial position for experimental model M7_EX at inlet velocity 113 m/s 113

Figure 6.16 Experimental comparison between shrouded wind turbine and bare wind turbine for extracted power 114

Figure A.1 Air velocity distribution in testing section1 (4 feet from the Fan) (air direction is blowing in reverse direction (backward)) 126

Figure A.2 Air velocity distribution in testing section2 (12 feet from the Fan) (air direction is blowing in reverse direction (backward)).....126

Figure A.3 Air velocity distribution in testing section1 (4 feet from the Fan) (air direction is blowing in forward direction).....127

Figure A.4 Air velocity distribution in testing section2 (12 feet from the Fan) (air direction is blowing in forward direction) 127

Figure A.5 shroud models (M1, M2, M3, and M4) (changing the angle of attack and keeping the length and throat radius constant) 130

Figure A.6 shroud models (M1, M5, and M6) (changing the shroud length and keeping the angle of attack and throat radius constant).....133

Figure A.7 Velocity contours for the six models 134

Figure A.8 Pressure contours for the models 135

LIST OF TABLES

Table 1.1 Comparison between bare propeller and the same propeller with an external Shroud system 14

Table 1.2 Parameters of C-type wind-lens. For C0-Cii diffuser (μ : The area ratio of (exist area/throat area).....16

Table 5.1 Configurations of the six models and experiment model.....86

Table 6.1 Augmentation factor for Empty shroud E423 models 96

Table 6.2 Back pressure ratios for the six models of the empty shroud E423 98

Table 6.3 Geometry configurations of empty shroud for the six models and drag coefficient 102

Table 6.4 The final numerical analysis for Grid2 for the six models, and percentage error with Grid3.....106

Table 6.5 Geometry and Grid information for convergence of Grid2 106

Table 6.6 Mathematical calculations of output power of the six models and bare wind turbine at different inlet air velocities.....108

Table 6.7 CFD Vs experimental work results of the augmentation factor.....112

Table 6.8 Experimental measurements of the extracted power for both bare wind turbine and shrouded wind turbine 114

Table A.1 Databases of the shroud models' geometries (M1,M2,M3,and M4) 128

Table A.2 Databases of the shroud models' geometries (M1, M5, and M6).....131

Table A.3 Grid convergence of model M1 136

Table A.4 Grid convergence of model M2 136

Table A.5 Grid convergence of model M3 136

Table A.6 Grid convergence of model M4 137

Table A.7 Grid convergence of model M5 137

Table A.8 Grid convergence of model M6 137

NOMENCLATURE

Abbreviations

SAWT	Shroud Augmented Wind Turbine.
DAWT	Diffuser Augmented Wind Turbine
HAWT	Horizontal Axial Wind Turbine
AR	Shroud Area Ratio
AF0	Augmentation Factor as described by Widnall
$AF0, W$	Widnall ideal augmentation factor
CFD	computational Fluid Dynamics

Greek characters

ε	Augmentation Factor as described by Phillips
$\mathcal{T}$	Turbulent time scale
μ	Air viscosity
v	Kinematic viscosity
β	Area shroud ratio
γ	Back pressure ratio
v_t	Kinematic turbulent viscosity
ρ	Air density
η_{diff}	Shroud efficiency with presence the rotor
$\eta_{empty,diff}$	Shroud efficiency without rotor (empty shroud)
η_{01}	Inlet diffusion efficiency
λ	Tip speed ratio
w	Angular velocity at blade tip

Subscripts

0	Station in ambient free-stream
1	Station at SAWT inlet
2	Station immediately upstream of the rotor plane
3	Station immediately downstream of the rotor plane
4	Station at diffuser exit plane
5	Station in far wake (well downstream of the turbine)
p_{total}	Total pressure in the system
p_1	Pressure in the inlet station
p_2	Pressure just before rotor plane
p_3	Pressure just after rotor plane
p_4	Pressure at exit shroud plane
V_0	Undisturbed air velocity
V_1	Velocity at inlet station
V_2	Velocity just before rotor plane
V_3	Velocity just after rotor plane
V_4	Velocity at exit shroud plane
V_5	Velocity at far wake
$A_{2,}A_3$	Area of throat plane
A_4	Area of exit plane
D_2	Diameter of throat section (station 3 or 2)
D_4	Diameter of exit section of the shroud

Symbols

A	rotor area
A_r	Area of rotor plane
a	Induction factor
C_p	Power coefficient in general form
$C_{p,d}$	Power coefficient of diffuser wind turbine
$C_{p,b}$	Power coefficient of bare wind turbine
$C_{p,rotor}$	Power coefficient at throat area (rotor is placed at throat section)
$C_{p,exit}$	Power coefficient at exit plane (if the rotor is placed at exit section)
$C_{T,total}$	Total Thrust coefficient
C_T	Thrust coefficient
C_{p4}	Shroud exit pressure coefficient
C_d	Drag coefficient
C_l	Lift coefficient
C_{P_b}	Base pressure coefficient
$C_{p_{23}}$	Diffuser pressure coefficient
D_r	Throat diameter (Described by Lubitz and Shomer)
D	Diameter of exit area (Described by Lubitz and Shomer)
F_{us}	Force acting on upstream flow
F_{ds}	Force acting on downstream flow
F_r	Thrust rotor force
F_d	Drag force (the force which is acting on the shroud)
f_x, f_y, f_z	External forces acting on the control volume
F_x	Total external force in *x*-direction

K	Resistance of coefficient
$\dot{m}$	Mass flow rate
P	Power
P_{shaft}	Power provided by the shaft
P_k	Production turbulent kinetic energy
$P_{dynamic}$	Velocity pressure (dynamic pressure) in inch of water
P_B	Barometric (or absolute) static pressure in inch of mercury
Q	Volume flow rate
r_{max}	Maximum power augmentation factor
R_{th}	Shroud throat radius
S_{ij}	Symmetric part of the mean strain rate tensor
T	Thrust Force
u_1	Velocity in wake (described by Hansen)
u	*x*-component of velocity vector, axial velocity at rotor plane (Described by Hansen)
U_i, U_j	Mean velocity in *x*, *y*-direction respectively
$\frac{\partial \rho}{\partial t}$	Rate of change of density inside the control volume
∇	Vector operation in Cartesian coordinates
$\nabla.\left(\rho\vec{V}\right)$	Net flow across boundaries of the control volume
u, v, w	x, y, z −Components of the velocity respectively
$\frac{\partial p}{\partial x}, \frac{\partial p}{\partial y}, \frac{\partial p}{\partial z}$	Differential pressure acting on the control volume
ΔP_T	The drop in total pressure

CHAPTER 1

INTRODUCTION

1.1 Background

For at least 3000 years before using wind to generate electricity, wind power had been used in land windmills, mainly for grinding grain or pumping water. At sea, the wind has been an important source of power for sailing ships for a long time. Windmills, which were designed in a horizontal –axis configuration, were an integral part of the rural economy. In addition over 2000 years ago, the Chinese invented vertical-axis windmills which are still used today. Over this long history of use, the wind has been strongly established as a means to create mechanical power.

Since the innovation of using wind to turn windmills was first found in Middle East back thousands of years, merchants from Europe and North America carried this idea back to their home land. Daniel Halladay is credited with invention of the first commercially successful, self-governing American windmill in 1854. Typically, it was used for pumping water, which includes a wheel, gearbox and tail assembly mounted on top of a tower as shown in **Figure 1.1**.

The wheel, which carries a number of vanes or sails, is connected to a gearbox, which converts rotary motion into vertical motion for pumping. The tail is offset from the wheel shaft to allow the tail to fold parallel to the wheel in high wind

conditions and effectively shut-down the mill and prevent destruction or damage due to high winds. (Rittner, 2010)

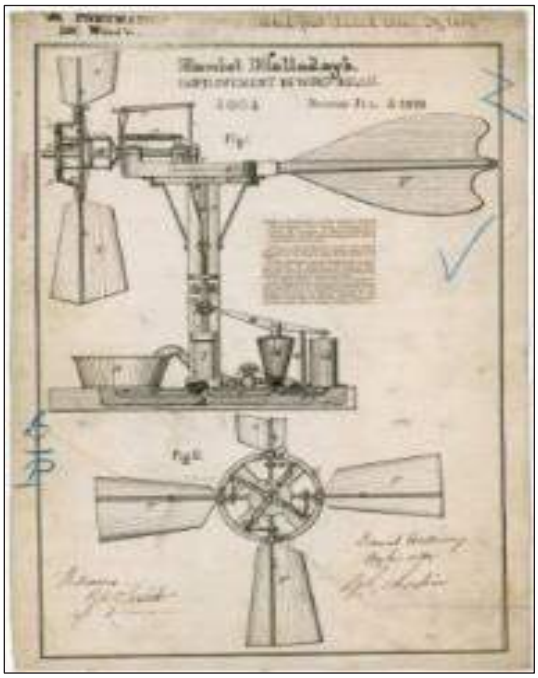

Figure 1.1 Daniel Halladay's first windmill in 1854 (Rittner, 2010)

A solid wheel as opposed to the sectional wheel was the second type of the American windmill. The blades were mounted together in a single rigid section and the control was maintained by moving the whole wheel to take advantage of wind flow direction (Spera, 2009).

Industrialization, first in Europe and later in America, led to mostly abandoning the windmill and replacing it with the stream engine for power operation. However, in 1888, Charles F. Brush, a famous inventor from Cleveland, Ohio, USA, had the idea to use large windmills to generate electricity; it is believed to be the first turbine operating automatically by using wind power. It was a 600 foot, 80,000 pound turbine, as shown in

Figure 1.2. It reportedly supplied 12 KW of power, 350 glowing lights, 2 arc lights, and a number of motors at his home for 30 years (Righter, 1996).

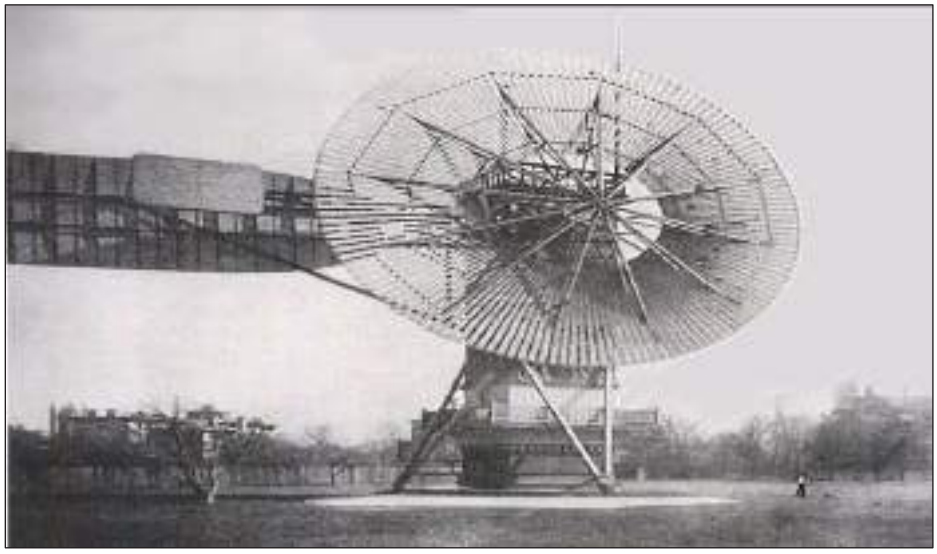

Figure 1.2. Charles Brush's windmill of 1888, used for generating electricity (Righter, 1996)

In relatively recent times, the usage of wind turbines has gained momentum. This is partially due to environmental threats from fossil fuel usage. It has become essential to look for energy sources which are renewable and clean to eliminate or reduce the environmental pollution and lower economic costs. In addition, expanding new economies from former third world countries have all contributed to an ever increasing need for energy and thus renewable energy technologies. According to Fuel Economy of the Official US Government Source (2012), highway vehicles release about 1.5 billion metric tons of greenhouse gases (GHGS) into the atmosphere each year-mostly in the form of carbon dioxide (CO_2) - contributing to global climate change. Each gallon of gasoline burned creates 20 pounds of CO_2; that is roughly five to nine tons of CO_2 each year for a typical vehicle.

The pie chart in **Figure 1.3** shows world energy usage by category for both renewable and nonrenewable sources. Renewable energy comes from sources with an unlimited supply. This includes energy from water, wind, the sun, and biomass. In the US, only about 10% of energy production comes from renewable sources and the majority of this is hydroelectric energy. Nonrenewable sources compose 85% of worldwide energy usage from sources that eventually will be depleted, such as oil, natural gases and coal (Rice University, 2006).

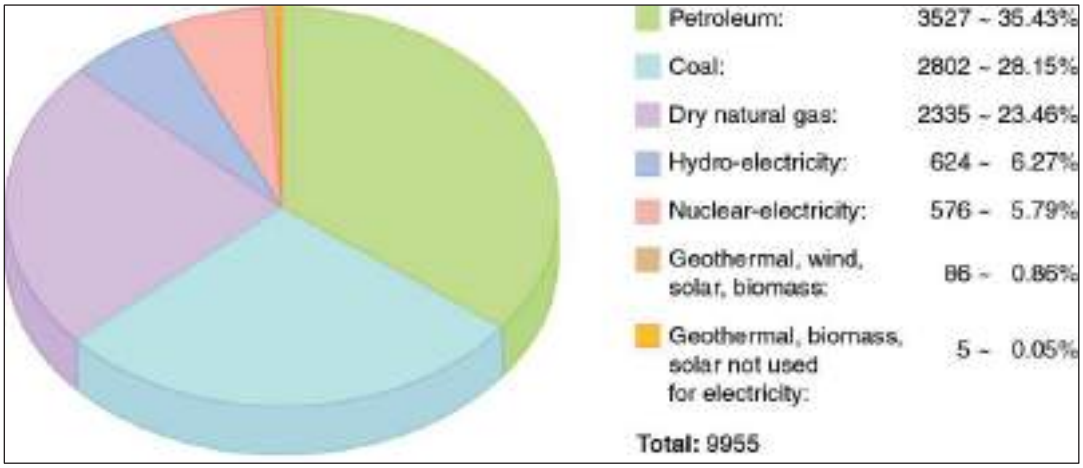

Figure 1.3. Primary worldwide energy sources nonrenewable (Rice University, 2006)

Therefore, the wind turbine has been used as renewable and alternative energy in addition to other sources such as hydropower, solar energy, and biofuel. The fundamental application of wind turbines is to extract energy from the wind. Hence, the aerodynamics is a very important aspect of wind turbines. Like many machines, there are many different types, all based on different energy extraction concepts. In order to optimize the wind turbine as efficient as possible, it is bilateral. First is the strategic positioning of the turbines within the wind farm, which have a suitable wind speed during the year, so that

the wake effects are minimized and therefore the expected power production maximized. Second is the determination of turbine configurations so that loading and therefore the stresses on various parts of the wind turbine can be calculated, in this state to ensure operation.

Hansen (2008) stated a wind turbine transforms the kinetic energy in the wind to mechanical energy in a shaft and finally into electrical energy in a generator. The maximum available energy, P_{max}, is thus obtained if theoretically the wind speed could be reduced to zero.

$$P = \frac{1}{2}\,\dot{m}V_0^2 \tag{1}$$

$$P = \frac{1}{2}\,\rho A V_0^3 \tag{2}$$

Where $\dot{m}$ is the mass flow rate, V_0 is the wind speed, ρ the density of the air and A the area of the rotor plane. Notice that, the power extracted from the wind power is proportional to the wind speed cubed. If there is a slight increase in velocity approaching the rotor area of wind turbine, it leads to a significant increase in output power. In reality and practically, it is impossible to lower the wind speed to zero behind the rotor turbine plane. A power coefficient C_p, is therefore defined as the ratio between the actual power obtained and the maximum available power, which is known as Betz limit. It is approximately equal to 0.59 for many of the modern turbine (Hansen, 2008).

Wind power is an affordable, efficient and abundant source of domestic electricity. It's pollution-free and cost-competitive with energy from new coal-fired and

gas-fired power plants in many regions. The wind industry has been growing rapidly in recent years.

In 2011 alone, according to NRDC (Natural Resourced Defense Council), 3,464 turbines went up across the United States. Today, American wind energy generates enough electricity to power more than 11 million homes, creates steady income for investors and landowners, and provides manufacturing, construction and operation jobs for at least 75,000 Americans. A typical 250 MW wind farm (around 100 turbines) will create 1,073 jobs over the lifetime of the project. By generating additional local and state tax revenues from lease payments, wind farms also have the potential to support other community priorities, such as education, infrastructure, and economic development. In some months, wind energy provides more than six percent of our nation's electricity, and experts estimate that in the future, wind energy could realistically supply five times that amount, thirty percent or more of our electricity needs.

Figure 1.4 illustrates the amounts of power extracted from wind by using traditional wind turbine in United States depending of the regions at the end of 2013.

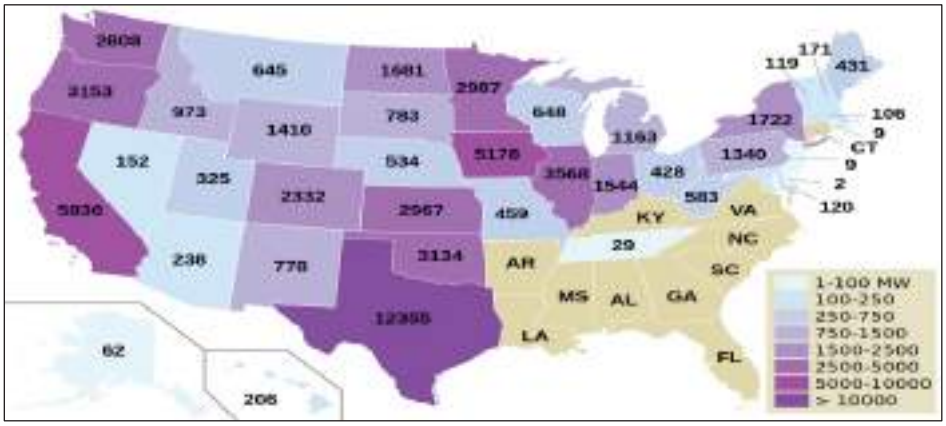

Figure 1.4 Map illustrating installed wind generating capacity for U.S. states at end of 2013 (Wind Power in United States: Wikipedia, 2014)

1.2 The Traditional Wind Turbine and Its Effect on the Local Environment

Traditional wind turbines have been built in two ways, in a horizontal axis orientation that are called HAWT, and in a vertical axis orientation called VAWT. The most common one of these two configurations is that with a horizontal axis. Although the traditional wind turbine has many desirable features, there are limitations and drawbacks to its usage. For the megawatt turbine, a strong average speed of at least 10 meter/second or greater is necessary in order to provide stable amount of electric energy economically. Also, while wind turbines are non-polluting, they do cause noise that affects the people who live close to those turbines, especially the megawatt wind turbine. According to Health Canada, in November 2012, Canada's installed wind turbine capacity was 5.9 Gigawatts, providing 2.3 percent of Canada's current electricity demands, but some public concern has been expressed about the potential health impacts of conventional wind turbine sound (WTS).

Other effects caused by convectional wind turbines are the threat to wildlife. The reason behind that comes from the large-scale construction of wind turbines. Many studies have looked at the effect of traditional wind turbines on birds and animals. Furthermore, in order to support the large turbines adequately, the foundation must extend deep into the earth, which affects the underground habitats.

1.3 The Shrouded Wind Turbine as a Replacement for Traditional Wind Turbine

Ducted or shrouded wind turbines have been invented and developed throughout the 20th century. The shrouded wind turbines have led to an increase in the extracted

power from the wind as compared to conventional wind turbines. In 1919, the German physicist, Albert Betz, derived a law from the principles of mass and momentum of the air stream flowing through an idealized “actuator disk” that extracts energy from the wind stream, called Betz’s Law. According to this law, no wind turbine in open flow can capture more than 59% of the available power (Hansen, 2008). However the shrouded wind turbines provide higher power coefficients about ($C_p = 2.5$), as compared to the power coefficient in conventional wind turbines ($C_p = 0.59$).

The size and geometric features of a shrouded wind turbine make it more environmentally friendly. The shrouded wind turbine generates less noise because of reduction of blade tip vortices. So, it can be installed in or near the urban or the residential area, or the farm areas near animals. Although there are a limited number of shrouded turbines in use, there also seems to be reduction of bird strikes, where no bird strikes have been reported. Also the shrouded wind turbine is comparably easy to install because it has less mass compared with the conventional wind turbine.

1.4 Literature review

This section reviews previous numerical and experimental analysis of shrouded wind turbines. Significant research has been carried out and technologies developed to improve the efficiency of shrouded wind turbines so that output power can be as high as possible.

Hansen (2008) mentioned that by using the assumption of an ideal rotor, it is possible to derive simple relationships between the upstream wind speed V_0, axial velocity at rotor plane u, velocity in wake u_1, the thrust T, and the absorbed shaft power.

These relationships can be obtained by using momentum theory on rotor plane analysis by applying Bernoulli equation. Close upstream of the rotor is a small pressure rise from the atmosphere level p_0 to p before a discontinuous pressure drop Δp over the rotor. Downstream of the rotor, the pressure recovers continuously to the atmospheric level, as shown in **Figure 1.5** (Hansen, 2008). The thrust is the force in the streamwise direction resulting from the pressure drop over the rotor, and is used to reduce the wind speed from V_0 to u_1:

$$T = \Delta p A \tag{3}$$

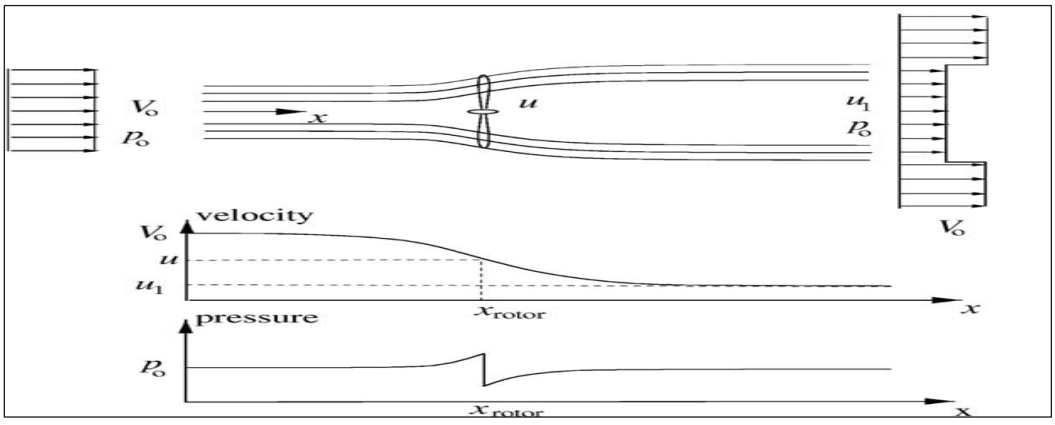

Figure 1.5 Illustration of the streamlines past the rotor and the axial velocity and Pressure Up- and downstream of the rotor (Hansen, 2008)

Where $A = \pi R^2$ is the area of the rotor, and Δp is the pressure drop across the rotor. The flow is assumed steady state, incompressible and frictionless. Therefore, the Bernoulli equation is valid from far upstream to just in front of the rotor and just behind the rotor to far downstream in the wake, and combining together, one can derive the expression for pressure drop:

$$\Delta p = \frac{1}{2}\rho(V_0^2 - u_1^2) \tag{4}$$

Hansen conducted a control volume analysis as shown in **Figure 1.6** of a bare wind turbine in order to establish power coefficient, *Cp*. The non-dimensional power coefficient C_p is represented by:

$$C_p = \frac{P_{shaft}}{P_{avail}} = \frac{T.u}{P_{avail}} \tag{5}$$

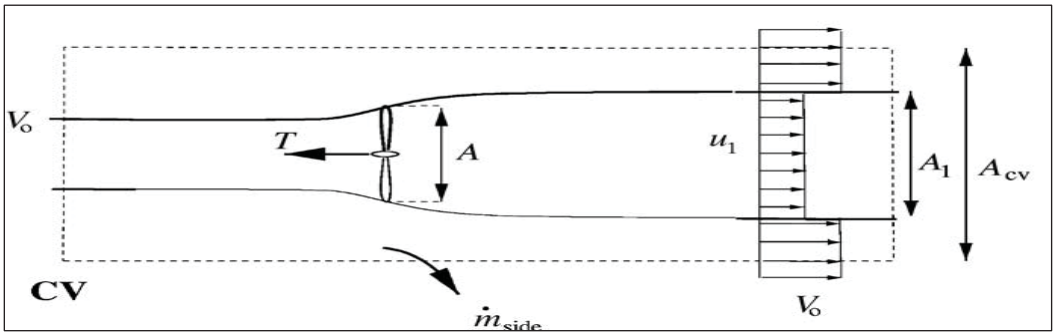

Figure 1.6 Circular control volumes around a wind turbine (Hansen, 2008)

The velocities in the rotor plane *u*, and the far wake u_1 are known in terms of induction factor *a*, and undisturbed velocity V_0 ,where *a* is fractional decrease in wind velocity between the free stream and energy extraction device*;* $u = (1-a)V_0$, and $u_1 = (1-2a)V_0$, respectively. The available power in a cross-section to the swept area *A* by the rotor is $P_{avail} = \frac{1}{2}\rho V_0^3 A$. Using these equations and substituting **Equations (3 & 4)** into **Equation (5)**, the power coefficient C_p of a bare wind turbine can be defined as:

$$C_p = 4a(1-a)^2 \tag{6}$$

Similarly, a thrust coefficient C_T is defined as:

$$C_T = \frac{T}{\frac{1}{2}\rho V_0^2 A} = 4a(1-a) \tag{7}$$

Differentiating C_p with respect to a, yields:

$$\frac{dC_p}{da} = 4(1-a)(1-3a) \tag{8}$$

Then it can be found the $C_{p,max} = {}^{16}/_{27}$ for $a = {}^{1}/_{3}$. This theoretical maximum for an ideal wind turbine without shroud is known as the Betz limit (0.59).

Hansen (2008) stated that it is possible to exceed the Betz limit by placing the wind turbine in a diffuser. If the cross-section of the diffuser is shaped like an airfoil, a lift force will be generated by the flow through the diffuser as seen in **Figure 1.7**.

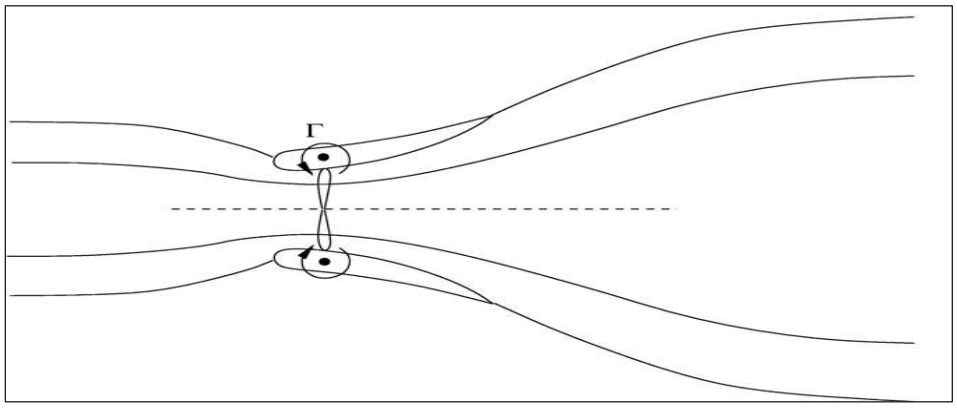

Figure 1.7 Ideal flows through a wind turbine in a diffuser (Hansen, 2008)

Now, the power coefficient in shrouded wind turbine $C_{p,d}$ becomes:

$$C_{p,d} = \frac{P}{\frac{1}{2}\rho V_0^3 A} = \frac{T.V_2}{\frac{1}{2}\rho V_0^2 \frac{V_0}{V_2} V_2 A} = C_T.\varepsilon \tag{9}$$

Where, ε is the augmentation defined as the ratio between the radial velocity in the rotor plane of ducted turbine V_2 and the upstream wind speed V_0 , i.e. $\varepsilon = V_2/V_0$. The power coefficient $C_{p,b}$ for an ideal bare wind turbine and thrust coefficient C_T from **Equations (6)** and **(7)** combining together give:

$$C_{p,b} = C_T(1 - a) \tag{10}$$

Combining **Equations (9)** and **(10)** yields:

$$\frac{C_{P,d}}{C_{P,b}} = \frac{\mathcal{E}}{(1 - a)} \tag{11}$$

From the mass flow through a turbine with a diffuser $\dot{m}_d$ and the mass flow through a bare turbine $\dot{m}_b$, it can produce:

$$\frac{\dot{m}_d}{\rho V_0 A} = \frac{\rho V_2 A}{\rho V_0 A} = \varepsilon \tag{12}$$

$$\frac{\dot{m}_b}{\rho V_0 A} = \frac{\rho(1 - a)V_0 A}{\rho V_0 A} = 1 - a \tag{13}$$

Hansen et al. (2000) found that the ratio of the power coefficient without shroud and with shroud is represented by the mass flow rate by combining **Equations (11), (12),** and **(13)**:

$$\frac{C_{p,d}}{C_{p,b}} = \frac{\dot{m}_d}{\dot{m}_b} \tag{14}$$

Equation (14) states that the relative increase in the power coefficient for a shrouded turbine is proportional to the ratio between the mass flow through the turbine in the

diffuser and the same turbine without diffuser. The results are that the Betz limit can be exceeded if a device increases the mass flow through the rotor is applied.

Jafari and Kosasih (2014) reported experimental and computational fluid dynamic (CFD) studies that have demonstrated significant power augmentation of a diffuser shrouded horizontal axis wind turbine compared to a bare one with the same swept area of the diffuser. These studies also found the degree of the augmentation is strongly dependent on the shape and geometry of the diffuser, such as the length and the expansion angle. The experiment was conducted by selecting a small wind turbine for simulation, which was AMPAIR 300 Watt as shown in **Figure 1.8**

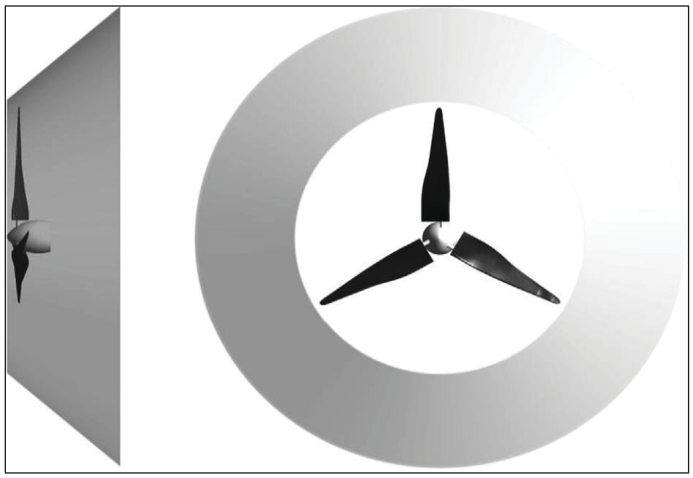

Figure 1.8 AMPAIR 300 Watt (Jafari and Kosasih, 2014)

Jafari and Kosasih concluded in their investigation that the amount of wind energy of air passing the rotor area is proportional to its mass flow rate. There are some methods to increase this mass flow. One method mentioned is by shrouding the rotor with a diffuser, which has an outlet area larger than its inlet. However, an easier method is

increasing the swept area of the rotor by enlarging its diameter. The computational results were validated by power output reported from the manufacturer in different wind speeds.

Grassmann, et al. (2003) made a comparison between a bare wind turbine and the shrouded wind turbine in their study on the physics of partially static turbines. The study used CFD simulation for both turbines, and by using specific boundary conditions, taking inlet wind speed 5 m/s, the result are shown in **Table 1.1**.

Table 1.1 Comparison between bare propeller and the same propeller with an external shroud system (Grassmann et al., 2003)

propeller	Bare propeller	Shrouded
V_2	4.20 m/s	7.95 m/s
F	7.45 N	16.9 N
Available power	31.1 W	135 W
Useful power (P_{shaft})	20.9 W	108 W

Where:

V_2 : Wind velocity in the rotor plane

F : The force in horizontal axis caused by velocity V_2

Another perspective of the shrouded wind turbine, Ohya and Karasudani (2010) developed a shrouded wind turbine by creating a broad-ring brim (flange) at the exit periphery and a wind turbine inside it. Experimental prototype equipped with a brimmed diffuser shroud rated power 500 W and the rotor diameter of 0.7 m. The diffuser length of this model was 1.47 times as long as the diameter of the diffuser throat D ($L_t = 1.47\ D$),

and the width the brim was (h=0.5D), **Figure 1.9**. The shrouded wind turbine with a brimmed diffuser demonstrated power augmentation factors between 2 and 5 compared with a bare wind turbine for a given turbine diameter and wind speed. In addition to the increase in the output power, the experimental investigations showed significant features such as a significant reduction in wind turbine noise, better tracking of the turbine with wind direction, and less over all turbine damage from broken blades during high speed.

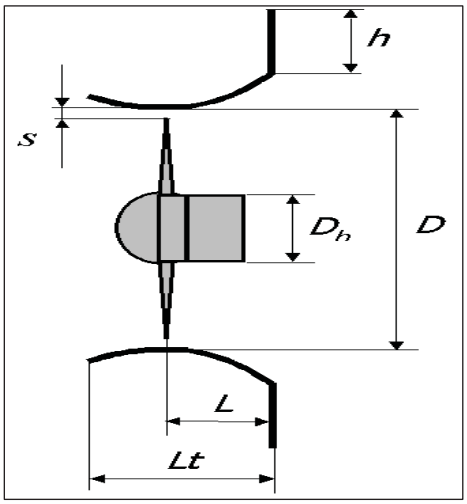

Figure 1.9 Wind turbine with a flanged diffuser shroud (Ohya and Karasudani, 2010)

Also, the experimental study investigated the length effect of the diffuser on the output performance of the turbines called Wind-lens turbines. Four kinds of C-type diffusers from C0 to Cii were prepared as described in **Table 1.2**. The results showed variation in power coefficient, which the researchers termed C_w with the diffuser length L_t/D . As expected, the C_w value becomes smaller as the diffuser length L_t/D becomes smaller. However, when the brim height is larger than 10% i.e., in case of $h > 0.1\ D$, the C_w of a Wind-lens turbine with C0-type diffuser shows almost two-fold increase

compared to a bare wind turbine, and the one with Ciii-type diffuser shows 2.6-times increase, as shown in **Figure 1.10**.

Table1.2 Parameters of C-type wind-lens. For C0-Cii diffuser (μ : The area ratio of exist area/throat area) (Ohya and Karasudani, 2010)

Diffuser	C0	Ci	Cii	Ciii
L_t/D	0.1	0.137	0.221	0.371
μ	1.138	1.193	1.294	1.555

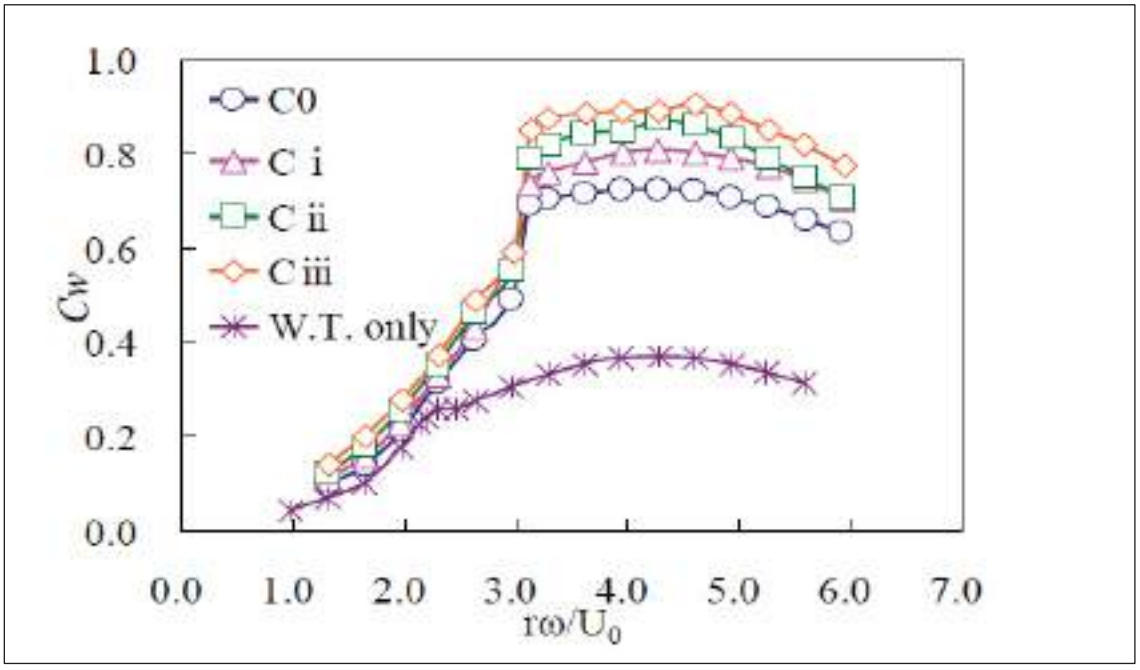

Figure 1.10 Power coefficient C_w of the wind-lens turbine with C-type wind-lens (h= 0.1D) (Ohya and Karasudani, 2010)

The practical Wind-lens turbine, 5 KW, was selected of the Cii-type diffuser ($L_t/D = 0.22$), and the brim height is 10%, i.e., $h > 0.1\ D$. The rotor diameter is 2500 mm. Three 5 KW wind-lens turbines were installed in a seashore park in Fukuoka city, Japan. A remarkable increase in the power of this turbine type was observed. It was 2.5 times increase in output power as compared to bare wind turbine (Ohya and Karasudani, 2010).

1.5 Scope of Work

The focus of this research had been on the aerodynamic investigations for developing of the shrouded augmented wind turbine (SAWT) design. Past studies of the SAWT was represented with a remarkable advancement in output power performance compared to a bare wind turbine. In order to further enhance the augmented velocity and achieve even better distribution of the air velocity inside the shroud, an optimizing design was sought in this study. However, the economic issues were underlying considerations. The computational analysis on six various full scale shroud models and experimental investigations had been undertaken in this study. The physics described in literature reviews showed the axial momentum theory developed for bare wind turbines by Hansen, and followed some conclusions of other works on shrouded wind turbines.

Chapter 2 describes some methodology views behind the shroud design. The effect of various design parameters on the shroud performance may well be accepted as the most important issues, particularly drag force, area ratio, angle of attack, cost effect, Kutta condition satisfaction, and shroud geometric influences. Some definitions and conclusions which indicate the interaction between shroud characteristics are represented in this **Chapter**. The most significant contributions are:

- Interrelationship between lift and drag force of the shrouded design, including, their interaction with regard to the angle of attack.
- Impact of the drag force on shroud wind turbine cost.
- Interrelationship between augmentation velocity factor and shroud area ratio and its length. In addition, the general trend of the shroud efficiency or power efficiency as a function of the area ratio.

- Aerodynamic interference between augmentation velocity factor and shroud body, especially shroud surface resistance, inlet, and outlet sections.

Chapter 3 focused overall –theoretical analysis of the shrouded wind turbine (SAWT). The mathematical analysis of SAWT is represented by applying axial momentum theory developed by Van Bussel (2007). Since there are various forces acting on shroud body once the wind turbine is placed in its throat area, it was significant to show the procedure for calculating these forces. In order to derive the appropriate equations of axial forces, an axial momentum balance was applied for one dimensional on the SAWT developed by Philips (2003) as illustrated well in this chapter.

Chapter 4 employs to describe the three experimental installations. The task of the first experiment was to determine velocity distribution in the testing section, using low airspeed wind tunnel. In the second experiment, the optimized shroud design was selected according to computational and theoretical analysis and then printed with a 3D printer using PLA plastic material. The perfect configurations of the experimental model of micro-shroud were obtained to get results that were accurate. This experiment consisted of creating and testing micro-empty shroud to verify the CFD results of air velocity distribution and argumentation factor. The third experiment included testing a micro-wind turbine with and without the shroud. The extracted power difference between SAWT and bare wind turbine was sought in this last experiment.

Chapter 5 illustrates computational fluid dynamic CFD techniques based on the solution of the Navier-Stokes equations using ANSYS-FLUENT 14&15. These techniques were applied to the configurations of shroud geometries of six models created by using software SolidWorks13 based on airfoil E423 databases. Airfoil E423 is an

Eppler high lift airfoil created by NACA. Each model was generated by revolving the airfoil E423 around an axis of symmetry. Models named M1, M2, M3, and M4 were created under different angle of attacks. While models M1, M5, and M6 were created under different length ratio. Model M1 was considered as optimum and the reference model. A model denoted M7_EX was the result of scaling down model M1 and was used for experimental investigations. Last contributions of this chapter discussed the computational methods of processing the models using ANSYS-FLUENT 14&15, particularly, the geometric domain, meshing, and solver methods.

Chapter 6 contains results of numerical calculations that were performed on the six various models and the experimental model. The goal of these calculations was to study the most important parameters of the shroud design that determine the possible performance benefits of the extracted power that gained from SAWT. The air velocity distribution and pressure distribution in both throat and exit shroud areas are presented in this chapter. In addition, with the basic phenomena known from the analysis of drag force on empty shroud, the way to gain benefits from optimizing shroud design with respect to cost effect, is discussed. Further, the mathematical calculations of extracted power in the six shroud models were shown in PV-curves. Finally, the validation results between computational and experimental work were compared clearly in **Chapter 6**. Overall conclusions and recommendations based on these results are discussed in **Chapter 7**.

CHAPTER 2
METHODOLOGY VIEWS OF THE SHROUD DESIGN

This chapter gives some definitions or methodology views related to the shroud design E423. Some conclusions from other works have been mentioned in order to confirm some thoughts about shroud design. Some researches denoted the shrouded wind turbine as DAWT, which is diffuser augmented wind turbine or ducted augmented wind turbine. Also it was referred to in this paper as SAWT, “shroud augmented wind turbine”. The shroud described in this research was created from airfoil E423, so it has been denoted as shroud E423. **Figure 2.1** shows the shroud E423 configurations. Where, L is the shroud length, R_{throat} is throat radius, D_{out} is the diameter of outlet section, and α is the expansion angle (angle of attack).

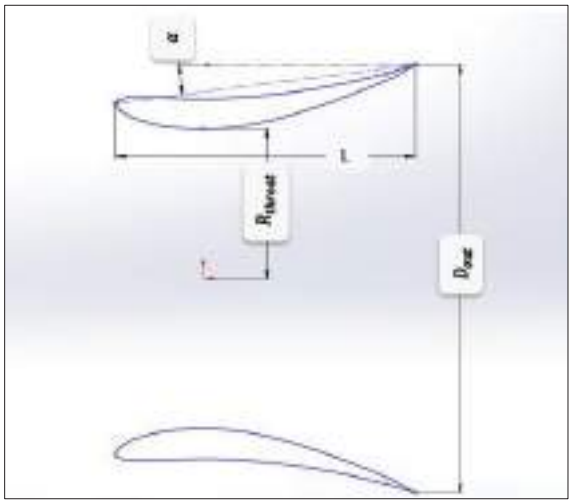

Figure 2.1 Shroud E423 configuration

2.1. Lift and Drag Characteristics of the Shroud Design

As a result of fluid flow over the surface of a body, the two forces exerted on it are denoted as lift and drag force. Lift force is the component of these forces, which is perpendicular to the oncoming flow direction while the drag force is the component of the surface force parallel to the flow direction. The lift and drag coefficient C_l and C_d are defined as:

$$C_l = \frac{F_l}{0.5\ \rho\ V_\infty^2\ c} \tag{2.1}$$

$$C_d = \frac{F_d}{0.5\ \rho\ V_\infty^2\ c} \tag{2.2}$$

Where ρ is the air density and *c* is the length of the airfoil or projected area of the body, V_∞ is the incoming velocity, and F_l and F_d are the lift and drag forces, respectively. The magnitude of the lift and drag forces is variable depending on body shape and also on the Reynolds number (Hibbeler, 2015).

In fluid dynamics, drag force of fluid resistance (air resistance) which is called fluid friction acts opposite to the relative motion of any “body” moving with respect to a surrounding fluid. The drag forces depend on velocity, and also it can exist between two fluid layers or a fluid and solid surface.

Since the shroud geometry was created from an airfoil in the curvature shape by revolving it around an axis of symmetry, this shape will generate these forces when the fluid flows on it. The drag force is the most influential force on the shroud, and it is described in chapter three in the **Equation (3.40)**.

However, Widnall (2009) indicated that the lift force on a shroud (duct) is not really lift, but is rather the suction pressure directed towards the axis of symmetry. In addition, Spera (2014) believed that the shroud lift forces are probably responsible for accelerating the wind speed through the throat area.

2.2. The Interrelationship between Drag, Lift Force and Angle of Attack.

Each airfoil has specific angle of attack, which is designed for an appropriate purpose. The lift coefficient (C_l) increases linearly with increasing angle of attack (α) until a maximum value of C_l is reached, with respect to Reynolds number, as shown in **Figure 2.2** (Hansen 2008).

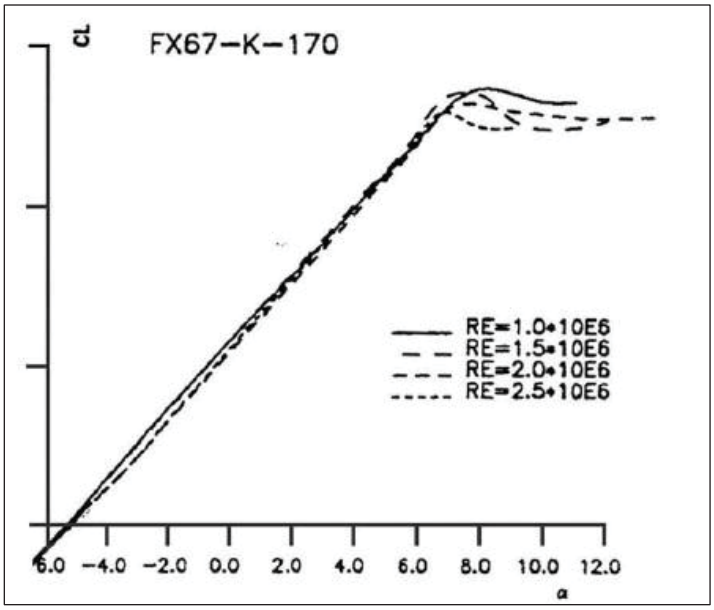

Figure 2.2 Lift coefficient C_l against angle of attack α for airfoil (FX67-K-170) (Hansen, 2008)

In the airfoil E423 which was selected for designing the shroud, the drag coefficient has maximum value at low lift coefficient, and the shape of the curve is

approximately parabolic (Abbott, 1949), **Figure 2.3(a)**. The relation between angle of attack and lift force is shown **Figure 2.3 (b)**.

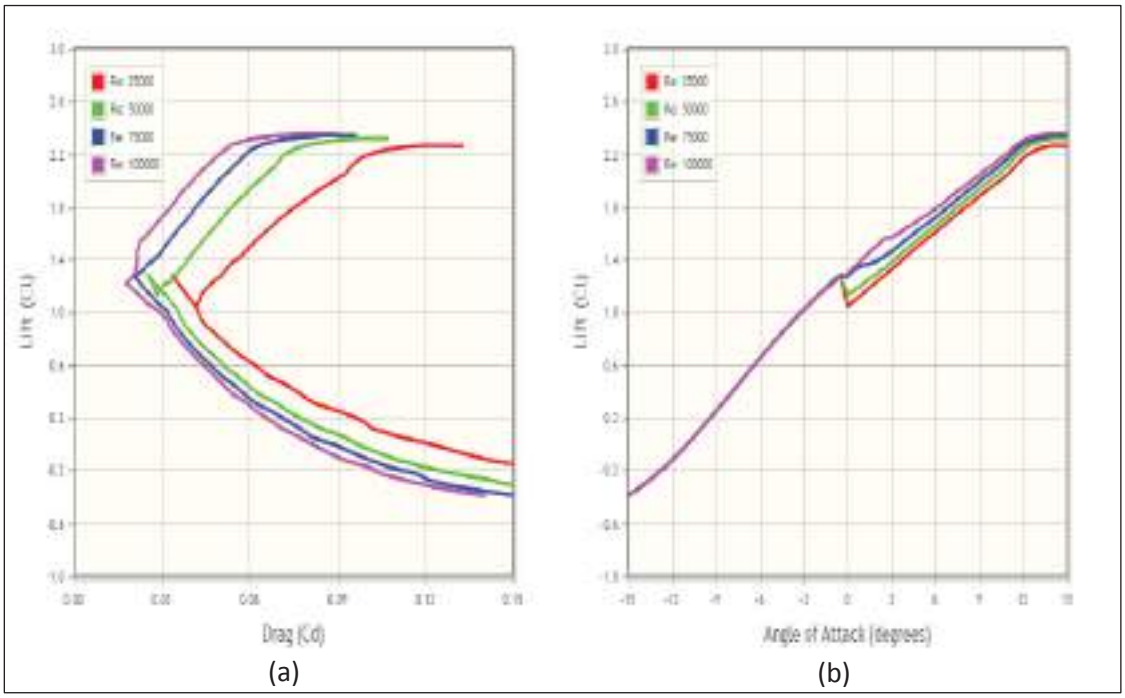

Figure 2.3 Lift and drag coefficients vs angle of attack for airfoil E423 (airfoil investigation database, 2013).

The angle of attack of airfoil E423 for shroud geometry has been changed and tested under different values to maximize the exit area ratio for the shroud, in order to increase the augmentation velocity factor of the shroud. Different angles of attack for this airfoil, and different length of the shroud were analyzed in CFD presented in **Chapter 5**. **Figure 2.4** shows airfoil E423 of the shroud under four different angles of attacks.

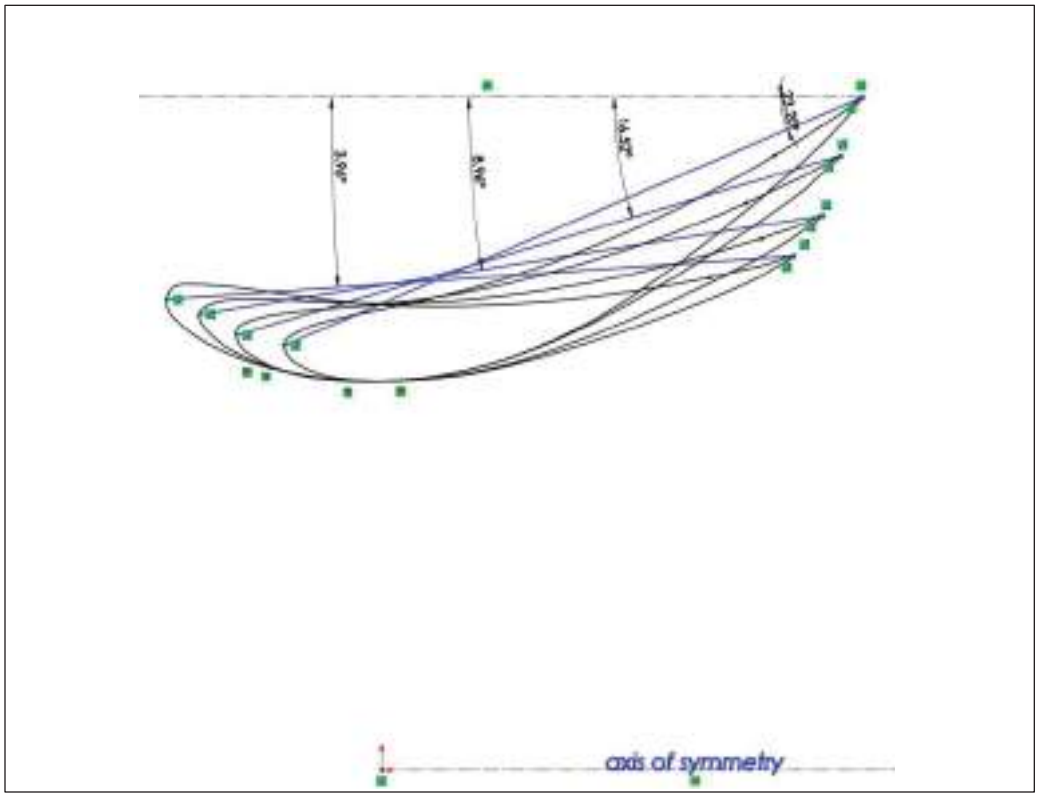

Figure 2.4 Airfoil E423 profile under different angle of attack**.**

As mentioned previously, Widnall (2009) asserted that the lift force is not a real lift force, rather a suction force directed to the center. According to the numerical analysis on empty shroud E423 in this study, it was found that the lift force is zero, which is directed toward the center of the shroud, and it is independent on the angle of attack. Thus, the influence of the angle of attack only focuses on the drag force.

2.3. The Influence of the Drag Force on SAWT Cost

The drag force has a substantial influence on the shroud design. High drag forces reduce the mass flow rate through the turbine, as shown in **Chapter 6** (augmentation velocity factor results). In addition, increasing the drag forces can lead to detrimental economic issues.

Foreman (1983) examined drag loads on three conical diffusers in the context of preliminary structural design and the cost estimates for DAWT designs using these diffusers. Foreman concluded that with using drag force coefficient (C_d= 0.54) as a half value of total drag coefficient (C_d= 1.1) which was found, based on diffuser frontal area in a 64.9 m/s extreme wind ,the cost effectiveness increases with size.

Lubitz and Shomer (2014) described the drag force on the shroud surface as the force acting on diffuser that aligned with the wind

$$F_d = \frac{1}{2} C_{dd} \rho \frac{\pi}{4} \left({D_0}^2 - D_r^2 \right) U^2 \tag{2.3}$$

Where D_0 is diameter of exit area, and D_r is the throat diameter of the shroud. C_{dd} is the diffuser drag coefficient, and U is wind velocity.

Lubitz and Shomer (2014) concluded that diffusers with flanged exits, sharp bends or very large opening angles (thus causing separated flow) would experience significantly greater aerodynamic drag than long, revolved airfoil diffusers. This can significantly impact required structural strength to ensure survival of the shroud in extreme winds.

It is clear that the design shape of shroud plays a large role in determining the extent of the influence of the drag force. Increasing the efficiency of the shroud requires increasing parameters such as the exit area, but still the benefit from increasing the exit area is worthwhile. While, Lubitz and Shomer (2014) mentioned that Phillips analysis (2003) found that the cost efficiency of a DAWT increases as the extent (size) of the diffuser (whole turbine system) is reduced, resulting in the extreme case that a conventional diffuser-less wind turbine would be most cost effective. Phillips (2003) also found, and clearly stated, that it is a design for extreme wind loads that is the limiting

structural case for DAWTs, and that these loads will be many times greater than for a HAWT (Horizontal Axial Wind Turbine) of comparable size.

As it is seen in **Equation 2.3** that drag force increases with increasing the exit diameter. Foreman et al. (1978) analyzed the diffuser (shroud) cost based on the size of the shroud especially on the dimension of the diameter. The study found that SAWT can be anywhere from marginally cheaper to much more expensive depending on whose authoritative judgment is used. Considering the benefits of SAWT, including a potentially greater factor for usable annual wind energy pattern, one can conclude the SAWTs generally become more economical than conventional Wind Energy Conversion System (WECS), regardless of the size turbine costing, the longer they are in operation.

Referring to, **Figure 2.5 (a)**, the cost of the DAWT (SAWT) or wind turbine increases with increasing the diameter which is in maximum value at diameter 100 meters. **Figure 2.5 (b)** shows that maximizing the size does not effect on the cost of the SAWT with respect to WECS. The difference between the two is that, in (b), the amount of the energy extracted by SAWT annually made the cost acceptable.

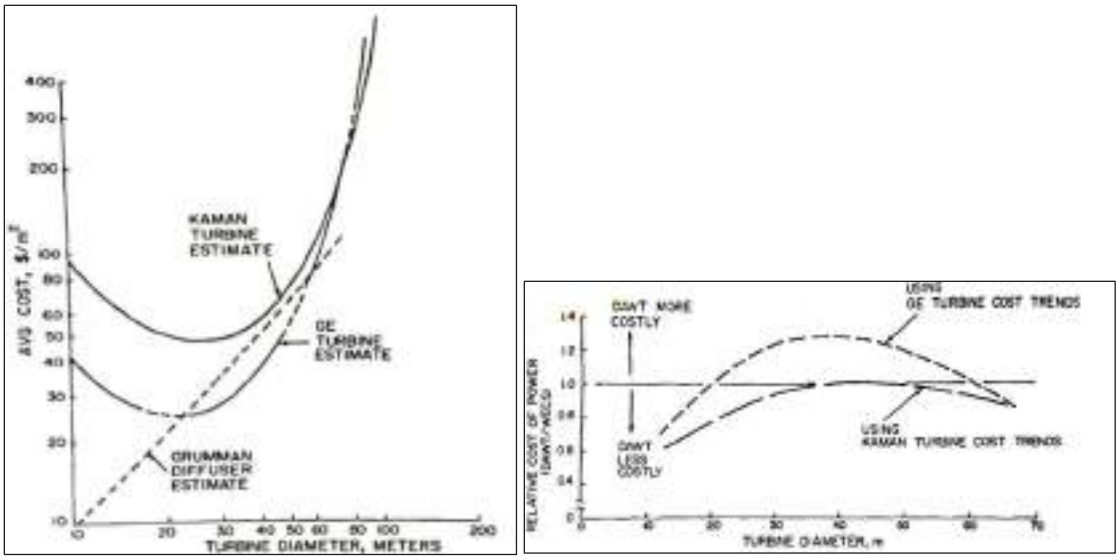

(a) (b)

Figure 2.5 Shrouded wind turbine cost estimates: (a) Average cost estimates of wind turbines and a baseline diffuser design (Foreman et al.(1978)). (b) Power cost comparison of DAWT (SAWT) and WECS for equal turbine size (Foreman et al.(1978)).

2.4. Shroud Materials Alternative

Selecting the appropriate materials of manufacturing the shroud structure has a big role in reducing the cost and making the shroud lighter and more sustainable to extreme wind loads. Forman (1980) had characterized three different materials involved in the manufacture of the shroud structure; aluminum, fiberglass reinforced plastic (FRP), and Ferrocement. Aluminum is widely used construction material in U.S with high initial cost, but with lower life cycle costs comparable with steel. Fiberglass reinforced plastic (FRP) also has high material costs, but it can be produced with low investment in machinery and tooling and low life cycle costs. Ferrocement's has low raw material costs, low investment requirements for tooling and production equipment, and high life

cycle costs. However, it is size limited that it cannot be used to fabricate SAWT in size greater than 6.8 m of the rotor diameter.

Today, companies such as Green Energy Technologies uses simple fiberglass reinforced plastic with different thicknesses depending on the size for manufacturing the shrouds. Fiberglass reinforced plastic possesses a desirable combination of properties. They have high strength and good dielectrically properties, relatively low density, low thermal conductivity, and high resistance to the effects of the atmosphere, water, and chemicals. The mechanical properties of the plastics are for the most part determined by the characteristic of the fiber and the strength of the bond between the fiber and resin. The variation of the processing temperatures also depends on the resin. Fiberglass reinforced plastic containing continuous fibers arranged in a particular fashion have high strength and rigidity (Tiukaev, 1979).

2.5 The Kutta Condition Satisfaction of the Shroud Design

The essence of the Kutta theory states that the fluid flow around an airfoil leaves the trailing edge of airfoil tangentially and smoothly. In addition, the fluid velocity at the trailing edge has to be finite. Since the shroud design was created from an airfoil by revolving about an axis of symmetry to generate diffuser shape, it is convenient to check this condition. However, Widnall (2009) considered that in most cases, the role of the Kutta condition has been ignored in favor of focusing on the internal flow, assuming atmospheric pressure and one-dimensional flow at the downstream edge of the duct (shroud). **Figure 2.6** shows four types of fluid flow over airfoil. In **Figure 2.6 (a)** with no circulation, the airfoil is in a position that causes infinite velocity about a sharp trailing

edge. In **Figure 2.6 (d)** where circulation of the flow leaves trailing edge smoothly, the Kutta condition can be applied.

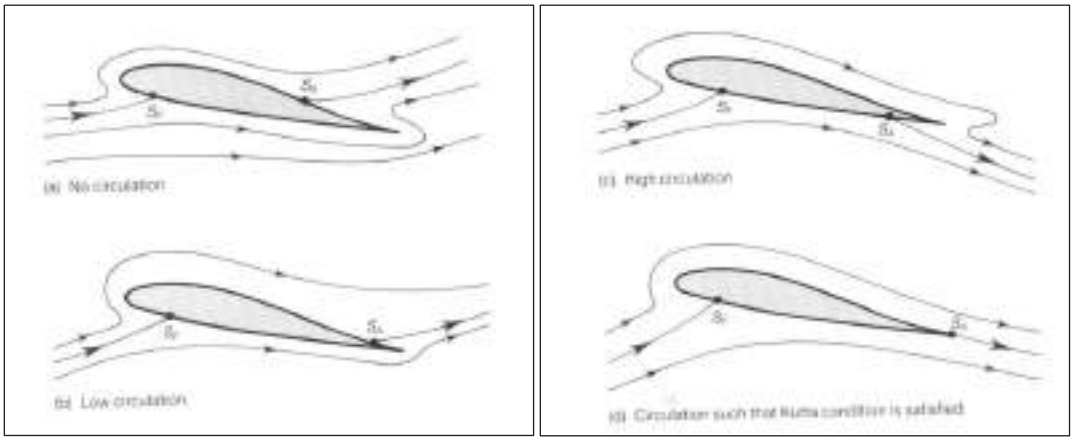

Figure 2.6 Four different types of the flow around an airfoil profile (a) no circulation (b) low circulatory (c) high circulation (d) circulation with satisfying Kutta condition (Kutta Conditions, 2012).

In other words, the Kutta condition determines how much of the flow goes through and how much goes around the duct. For a smooth shape function, the Kutta condition is automatically satisfied (Rienstra, 1992).

E423 airfoil, which was selected in this research, has a sharp trailing edge that helped to make smooth flow in the exit area of the shroud. As shown in **Figure 2.7**, the flow has satisfied the Kutta condition in the airfoil E423 at 8.96° of the angle of attack for full scale of the shroud.

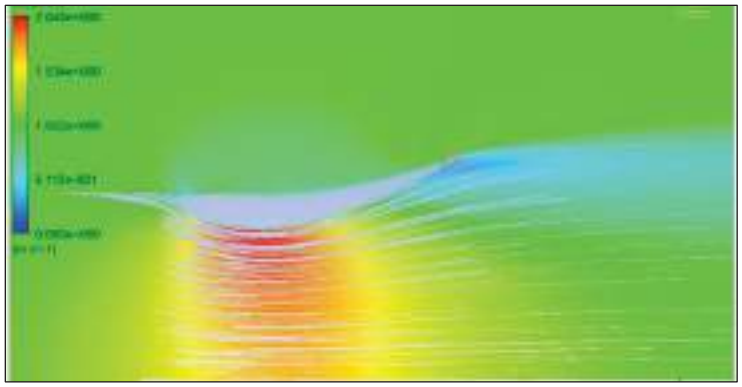

Figure 2.7 E423 airfoil profile at 8.96° of the angle of attack which shows flow streamline over the surface of airfoil (circulation with satisfying Kutta condition).

2.6. Augmentation Velocity Factor vs Shroud Area Ratio and Its Length

Widnall (2009) showed that augmentation velocity factor (average velocity at throat/undisturbed velocity) increases linearly when increasing the area ratio. Widnall used a specific angle of attack of the shroud design and increased the area ratio by increasing the length ratio (shroud length/ shroud throat diameter).

Also, the Widnall's relationship between augmentation velocity factor and area ratio was confirmed in this study, in **Chapter 6**. It was shown clearly between the models M1, M5, and M6. However, increasing area ratio by increasing the angle of attack while keeping length ratio constant causes reduction in augmentation velocity factor due to high separation layers in the exit plane of the shroud, as shown in **Chapter 6** (Model M3 and M4).

Shinomiya et al. (2013) tested and analyzed different shroud geometries with different area ratios and different shroud lengths. That study found that increasing the length and area ratio leads to increase in augmentation velocity factor, as shown in **Figure 2.8**.

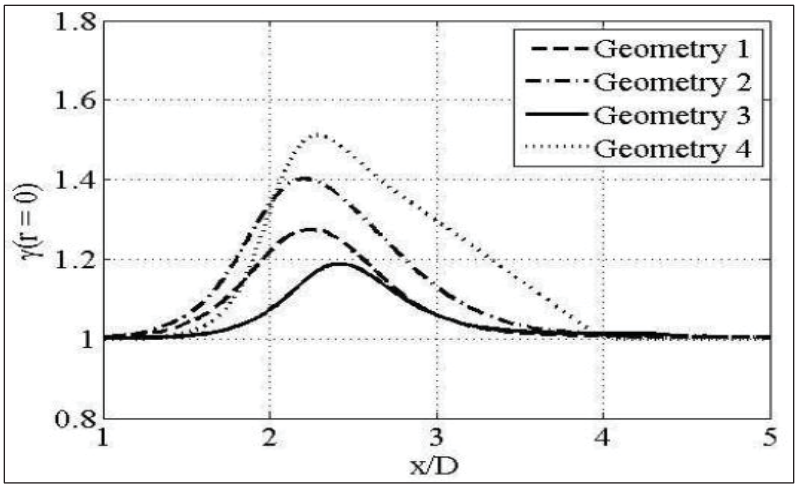

Figure 2.8 Augmentation Factor γ on the axis of symmetry for the simulated geometries (Shinomiya, el, 2013). Note that geometry 1 to geometry 4 indicates an increase in the *L/D* ratio

Where, γ was considered as augmentation velocity factor. The geometry 4 presented the highest speed-up ratio with an aspect ratio L/D =1.5. Where the L is the length of the shroud and D is the throat diameter. Even though geometry 4 has a high augmentation factor, it was evaluated to be the highest cost construction. Geometry 2, which was less costly, was selected by the authors to be an appropriate one with L/D =0.35. Other geometries with low area ratio and length matched with low augmentation factor (Shinomiya et al., 2013).

As it is confirmed computationally on the shroud E423 models in **Chapter 6**, the augmentation velocity factor increased in model M5 and M6 when the area ratio and the shroud length increased. For consideration, increasing the length ratio (L/D) increases the cost of construction for the shroud, but at the same time, it will maximize the augmentation velocity factor coinciding with increasing the exit shroud area.

2.7 Exceeding Betz Limit

In SAWT, the Betz limit was exceeded by a factor of 2-4. Depending upon applying **Equation 3.16**, in **Chapter 3** which is developed by Van Bussel, the power coefficient increased when the turbine is placed inside the shroud. For example, if the area ratio considered is 2 and back pressure ($\gamma = 1$), then the power coefficient for SAWT became 1.18, while the Betz limit is 0.59. This shows an increase in power coefficient of SAWT to be twice of that of a bare wind turbine. Actually, the Betz limit can be exceeded up to 4 times by increasing the area ratio of shroud.

Jamieson et al.(2008) investigated experimentally in their research that the diffuser and other flow concentrating devices have shown that the power performance coefficient C_p, may exceed the Betz limit. However, authors stated that no theory exists to define in a generalized way what ideal limit may apply to C_p in such situations.

2.8 Relationship between the Shroud Power Augmentation Factor, Shroud Efficiency, and Shroud Area Ratio.

Igra (1981) derived the shroud power augmentation factor (r) in presence of an actuator disk. This factor expresses the ratio between the power delivered by the shroud wind turbine and the maximum power available from an ideal wind turbine:

$$r = \frac{\Delta P_T Q}{\frac{0.593}{2}\rho V_0^3 A_t} \tag{2.4}$$

Where, ΔP_T is the drop in total pressure through the shroud wind turbine and Q is the volumetric flow rate passing through the shroud. A_t is throat area and V_0 is undisturbed

airspeed. This relation can be written with the diffuser efficiency η_{diff}, non-dimensional shroud exit pressure C_{pe} , and shroud area ratio $\frac{A_e}{A_t}$:

$$r_{max} = 0.649 \left(\frac{\left(1 - C_{pe}\right)^3}{1 - \eta_{diff}\left[1 - \left(\frac{A_t}{A_e}\right)^2\right]} \right)^{1/2} \tag{2.5}$$

Where:

$$C_{pe} = \frac{P_e - P_0}{\frac{1}{2}\rho V_0^2} \tag{2.6}$$

The P_e is exit pressure, the same P_4 as shown in **Chapter 3** in **Figure 3.3**, and A_e is the shroud exist area. η_{diff} can be obtained from **Equation (3.21)** in **Chapter 3**.

Igra (1977 and 1980) concluded that to achieve maximum power augmentation factor the following requirements have to be met: reference **Equation 2.5**;

- The shroud exist pressure C_{pe} should be as low as possible.
- For a given shroud (diffuser) area ratio $\frac{A_e}{A_t}$, η_{diff} should be as large as possible.
- For a given shroud efficiency η_{diff}, $\frac{A_e}{A_t}$ should be as large as possible.

Also, Igra(1981) showed that the shroud power augmentation factor increased with increasing the shroud area ratio for different designs, as shown **Figure 2.9.**

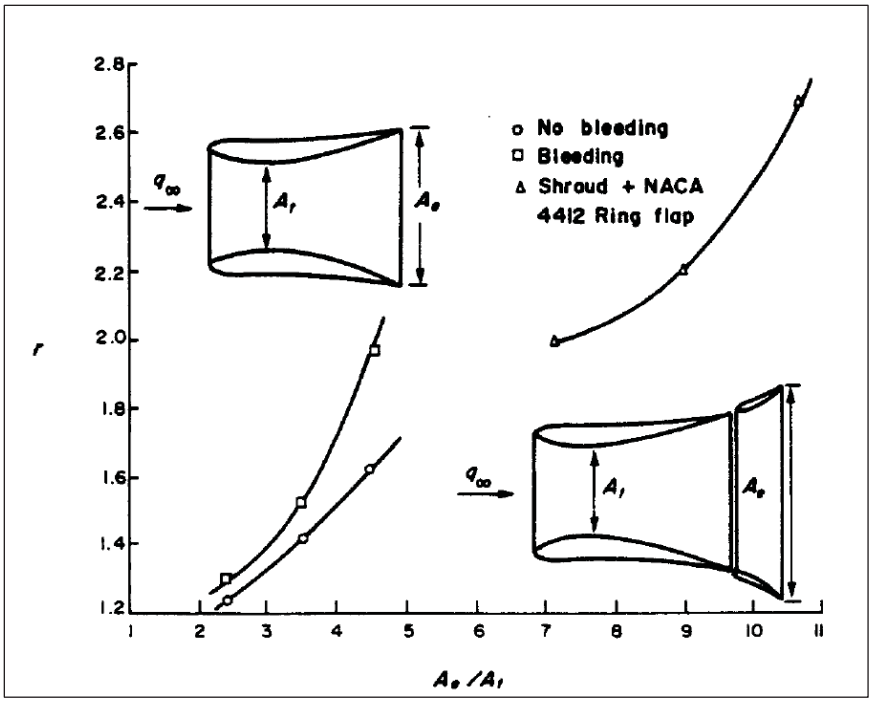

Figure 2.9. Shroud power augmentation factor (r) versus the shroud area ratio $\frac{A_e}{A_t}$ (Igra, 1981)

From these requirements, it can be concluded that the power coefficient **Equation (3.16)** in **Chapter 3** which was developed by Bussel agreed with Igra's augmentation factor that by increasing area ratio, the power would be increased.

2.9 Geometric Influences on SAWT Performance (inlet, outlet, shroud resistance, blade number…etc.)

2.9.1. Inlet section

The inlet section in the shroud E423 has an influence for enhancement of the augmentation velocity factor. The inlet section works as nozzle which helps for increasing the air entrance to the shroud.

Figure 2.10 (a) shows the configuration of inlet section for the shroud E423. The inlet section kept with small length and lower angle comparing to the outlet section as shown in **Figure 2.10 (b),** because the theory of generating power by using shroud is focused on the increasing the exit section more than inlet. Also, increasing entrance section of the shroud is due to economic issues.

(a) (b) (c)

Figure 2.10 Sections of shroud E423, (a) inlet section (b) outlet section (c) side view of shroud E423.

Kossasih et al. (2012) investigated the performance of the diffuser (shrouded) micro wind turbine using nozzle in front of the diffuser and without using it, as shown in Figure **2.11 (a)** and **(b)** respectively.

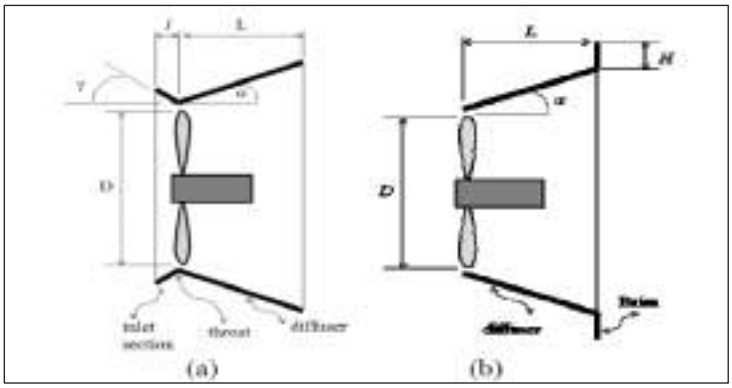

Figure 2.11 Simple shroud designs for wind turbine (a) nozzle-diffuser and (b) diffuser-brim shroud (Kossasih et al., 2012)

Kossasih et al.(2012) concluded that power coefficient C_p of the micro wind turbine increased by approximately 56% with simple diffuser, and 61% with nozzle – diffuser shroud. The nozzle –diffuser augmentation showed an increase in the performance by 5% compared to the diffuser augmented alone.

In reality, the profile of airfoil E423 enhanced to generate the curvature inlet section to the shroud geometry as in a nozzle. In **Chapter 6**, it was found there is an influence of the inlet section on augmentation factor between model M4 and M5 which they have the same area ratio. Model M4 has high angle of attack and short entrance section compared to model M5 which has less angle of attack with longer entrance but it has augmentation factor higher than model M4.

2.9.2 Outlet section

The exit plane or outlet section in the shroud as shown in **Figure 2.9(b)** is the most important geometric part, since it determines the amount of the energy extracted from the air based on the theory used in this research. According to **Equation (3.16)** in **Chapter 3**, increasing the exit diameter of the shroud for a given throat diameter which is represented by shroud area ratio $\boldsymbol{\beta}$ will maximize the power significantly. The large open exit plane causes a decrease in the pressure inside the shroud, and subsequently pulls more velocity to the shroud and maximizes the extracted power. However, increasing the exit diameter of the shroud leads to increase in the drag force which in turn requires a sustainable structure to withstand the high loads caused by the high airspeeds.

2.9.3 Shroud Resistance

The shroud resistance for the flow is caused by some factors which may be caused by the degree of surface smoothness, angles of the exit and inlet section, rounded inlet section, separation layers(boundary layers) ...etc. Lawn (2003) made assumption for letting K to be a resistance of coefficient to the flow velocity V_2 incident on it:

$$K = \frac{p_2 - p_3}{\frac{1}{2}\rho V_2^2} \tag{2.7}$$

Where V_2 is the velocity at throat area of the shroud, p_2 and p_3 are the pressure just before and after rotor plane, respectively. Also, Lawn (2003) formulated from Bernoulli's equation the velocity at the throat area in term of K and efficiencies upstream and downstream:

$$V_2 = V_0 \sqrt{\frac{\eta_{01} - C_{P_b}}{\eta_{01} + K - C_{p_{23}}}} \tag{2.8}$$

Where:

η_{01} is the inlet diffusion efficiency, formulated by:

$$\eta_{01} = \frac{p_2 - p_0}{\frac{1}{2}\rho V_0^2 - \frac{1}{2}\rho V_2^2} \tag{2.9}$$

C_{P_b} is the base pressure coefficient, defined as:

$$C_{P_b} = \frac{p_3 - p_0}{\frac{1}{2}\rho V_0^2} \tag{2.10}$$

$C_{p_{23}}$ is the diffuser pressure coefficient formulated by:

$$C_{p_{23}} = \frac{p_3 - p_2}{\frac{1}{2}\rho V_2^2} \tag{2.11}$$

Lawn concluded that the low resistance coefficient (K) enables the velocity enhancement at the throat V_2. One of approaches to make the velocity enhancement ($V_2 > V_0$) is that the base pressure (C_{P_b}) has to be negative. Then, the pressure p_3 just after rotor plane must be lower than the ambient pressure p_0 (**Reference Equations 2.8 & 2.10**).

2.9.4 The Number of the Turbine Blades

The blade number of SAWT also has an influence on the shroud performance. Wang and Chen (2008), in their CFD analysis, investigated the drawbacks of using high numbers of the turbine blade. **Figure 2.12** shows the power coefficient Cp versus tip speed ratio (λ) using different number of blades.

$$\lambda = \frac{w.r}{V_0} \tag{2.12}$$

Where w is the angular velocity at blade tip, r is the rotation radius of turbine, and V_0 is undistributed airspeed.

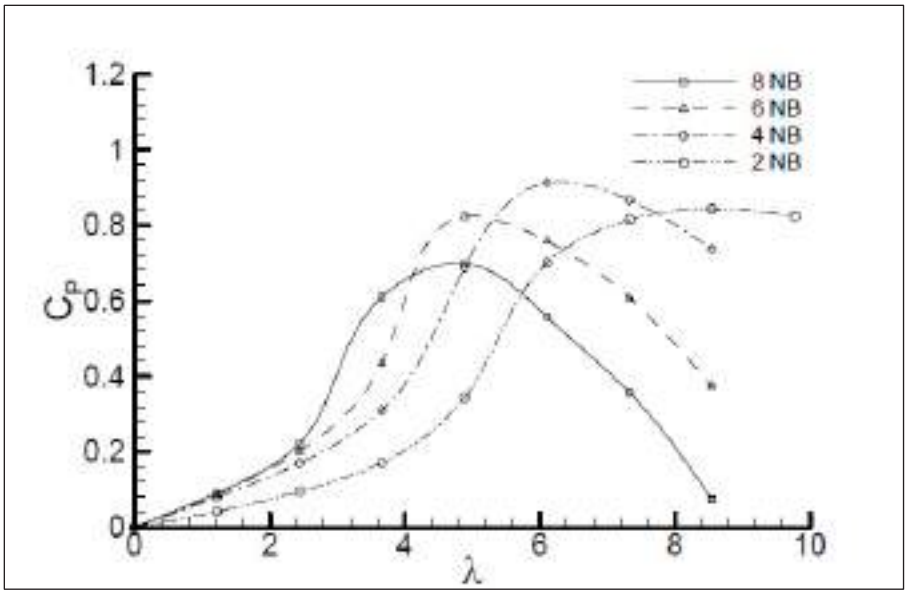

Figure 2.12 The power coefficient vs tip speed ratio with using different number of turbine blades (Wang and Chen, 2008).

Wang and Chen concluded that the number of blades has an effect on the ducted wind turbines studied with the use of CFD technique. Increasing the number of blades creates higher starting torque, reduces cut-in speed, and provides the sufficient blade area to transfer the wind energy. However, high number of blades leads to more blockage and lower blade entrance velocity. Eventually, the power coefficient will reduce. For this reason, an optimum number of blades will provide better power performance. According to Wang and Chen's study, the rotor plane with four blades is an appropriate number of blades.

CHAPTER 3

MATHEMATICAL MODELING OF THE SAWT DESIGN

This chapter presents the mathematical analysis for SAWT (Shrouded Augmented Wind Turbine) using the same conceptions applied on bare wind turbine. In order to derive the relative equations of SAWT, the better way is to show the aerodynamic conceptions with no shroud; this mathematical analysis on the bare wind turbine has already been discussed in the literature review in **Chapter 1** . The performance of SAWT relies on a number of geometric influence, flow characteristics and operation parameters. The mathematical application in this chapter depended upon the data collected from numerical analysis and experimental work for verification.

The simplest aerodynamic model for both of the bare wind turbine and shrouded wind turbine is the actuator disk model in which the rotor becomes a homogenous disk that removes energy from the wind. The change in the pressure and velocity upstream and downstream of actuator disc can be described by Bernoulli equation under the assumption of one-dimensional analysis. The approach used for analysis of the shrouded wind turbine is the same as that for the bare wind turbine except some forces added to the loading disk, augmentation velocity factor, and backpressure ratio, which maximizes the output power equation.

Mathematical Analysis

As mentioned in first chapter in the literature view, Hansen (2008) has derived the extracted power equation for bare wind turbine. Hansen also found the relationship between mass flow rate for bare wind turbine and SAWT; that is the relative increase in the power coefficient for a shrouded turbine is proportional to the ratio between the mass flow through the turbine in the diffuser and the same turbine without a diffuser. However, this chapter focuses on deriving the equations of SAWT with and without (empty diffuser) actuator disk, and applying momentum balance on the SAWT.

The assumption carried on a bare wind turbine in one-dimensional analysis is that the turbine is represented as an actuator disc (Burton et al., 2001). The disk is considered ideal. The rotational velocity component in the wake was neglected, and the disk is also considered frictionless. The entire process is assumed to occur at a small Mach number and air density is thus constant. The flow is also assumed to be steady, incompressible, and frictionless, and external forces were neglected. These conceptions can be applied on SAWT. The difference, however, is that external forces acting on the fluid upstream and downstream of the turbine exist in SAWT (Phillips, 2003). The flow throughout the shroud is assumed to be attached to the shroud surface, and the separation point happens only from the diffuser trailing edge (Yamin et al., 2013), see **Figure 3.1**.

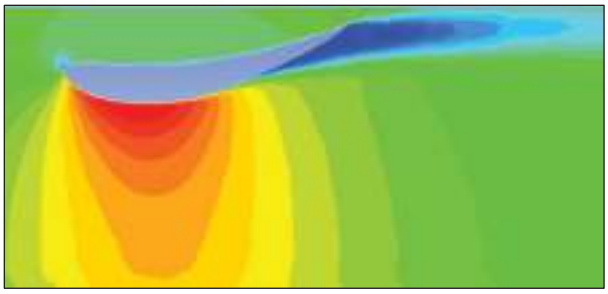

Figure 3.1 Velocity contour of the symmetric shroud E423, 2-Dimension. Separation layers appears only in the trailing edge.

3.1 Pressure and Velocities inside an Empty Diffuser (Shroud)

It has been mentioned in the literature review that applying momentum theory on rotor plane represents by applying Bernoulli equation. As assumed the flow is inviscid, the relationship between the pressures far in front of the empty diffuser (shroud) and its exit can be written down (Van Bussel, 2007).

$$p_{tot} = p_0 + \frac{1}{2}\rho V_0^2 = p_2 + \frac{1}{2}\rho V_2^2 = p_3 + \frac{1}{2}\rho V_3^2 = p_4 + \frac{1}{2}\rho V_4^2 \tag{3.1}$$

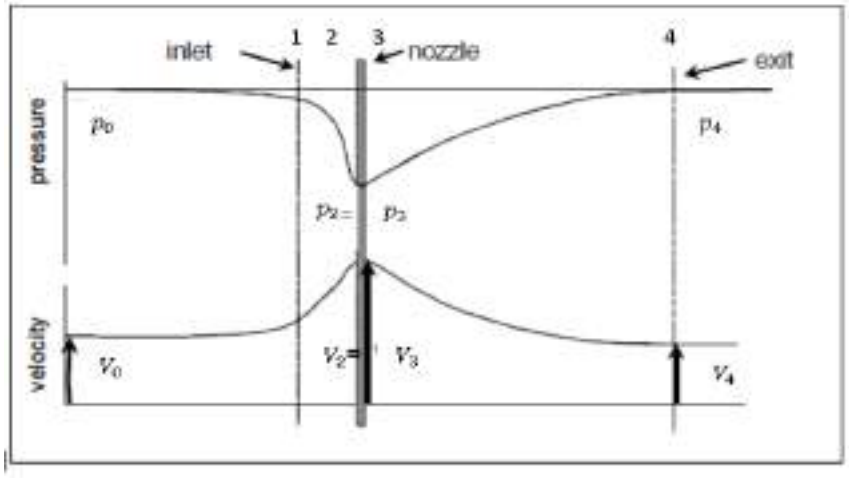

Figure 3.2 Pressure and velocity relationships in an empty shroud (diffuser) (Van Bussel, 2007).

Where the parameters in **Equation (3.1)** are shown in **Figure 3.2**. p_0, V_0 *and* p_4, V_4 are the pressures and velocities at inlet and exit plane respectively . p_2, V_2 *and* p_3, V_3 are pressures and velocities at the throat area, located before and after the loading disk(actuator disk). Since there is no loading disk (empty diffuser), p_2, V_2 are therefore the same as p_3, V_3.

Van Bussel (1999) used the continuity equation to derive a relationship between the velocity at the throat (nozzle) and the velocity at the shroud (diffuser) exit that is denoted as diffuser area ratio β

$$V_2 A_2 = A_4 V_4 \tag{3.2}$$

$$V_2 = \beta V_4 \quad or \quad \beta = A_4/A_2 \tag{3.3}$$

Therefore the total pressure at the throat area (nozzle), using the relation(3.3), can be written:

$$p_{tot} = p_2 + \frac{1}{2}\rho(\beta V_4)^2 \tag{3.4}$$

The theory behind the derivation for power and the loads in sections (3.3 & 3.6), depends on the area ratio factor and also on the back pressure in the exit area of the shroud. By taking the assumption that no back pressure at the shroud exists, the pressure at the exit area section is equal to the pressure at inlet ($p_4 = p_0$); this is also true for velocities ($V_0 = V_4$). Therefore, the equation for pressure at the throat can be expressed as follows:

$$p_2 = p_0 + (1 - \beta^2)\frac{1}{2}\rho(V_0^2) \tag{3.5}$$

Van Bussel (1999) stated that the **Equation 3.5** shows that a negative pressure will exist at the nozzle, whenever the diffuser area ratio is larger than 1. This is evidently the case when the exit area is larger than the nozzle (throat area) and no flow separation occurs.

In case, when back pressure in the shroud exists, Igra stated that the shrouded exit pressure should be as low as possible in order to achieve more pressure recovery. The back pressure occurs when Kutta-condition is applied on the shroud exit area such as sharp edge of airfoil, and the flow is forced to deflect in radial direction, and also when separation of the layers occurs on the trail edge of the shroud as shown in **Figure 3.1**. In this state, the velocity at exit area is different from undisturbed velocity in the front of the shroud V_0

$$V_3 = \gamma V_0 \tag{3.6}$$

Thus, the pressure will be at the throat section:

$$p_2 = p_0 + (1 - \beta^2\gamma^2)\frac{1}{2}\rho V_0^2 \tag{3.7}$$

Where, γ is the back pressure ratio, and p_2 is pressure at throat area. Therefore, back pressure ratio will be one or more $(\gamma \geq 1)$ if the shroud area ratio is more than one, then the pressure at exit area is zero or negative.

3.2 Pressure and Velocities inside the Shroud with Presence Axial Turbine (Actuator Disk)

Likewise in a conventional wind turbine, the momentum theory can be applied on the close upstream of incoming velocity and downstream of exiting velocity across the rotor plane which is represented by actuator disk. In the SAWT, the same approach can be applicable. However, the location of the rotor plane (actuator disk) is placed wherever the small cross section area is. The narrow section or nozzle section of the SAWT caused an increase in the local velocity, and it is also drops the total pressure in exit area.

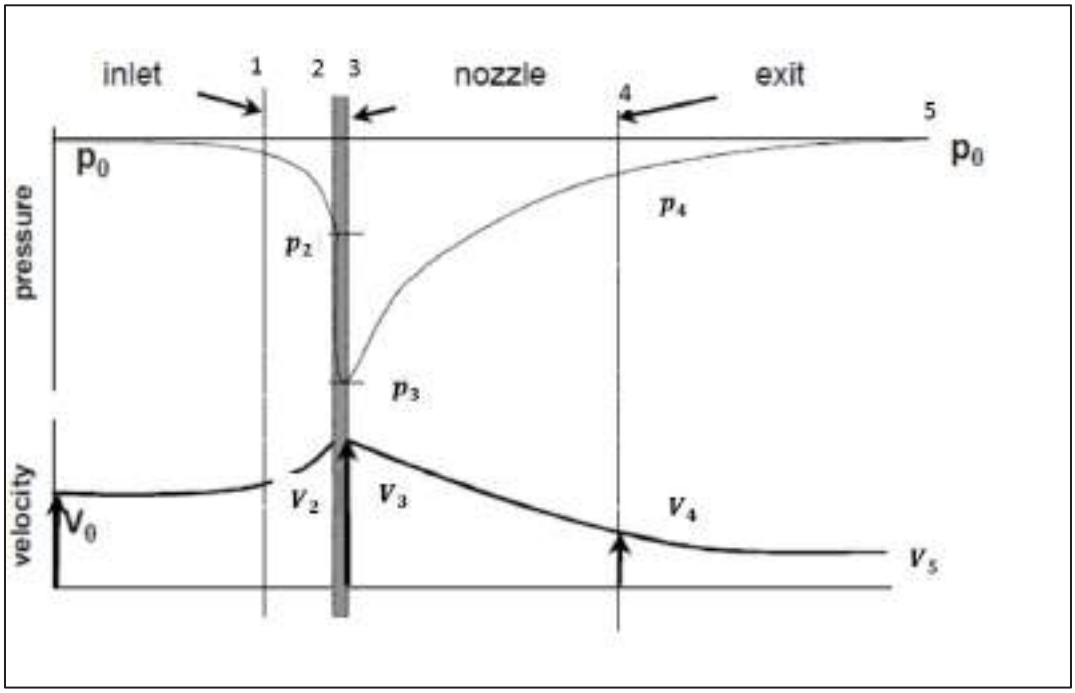

Figure 3.3 Optimal pressure and velocity distribution for SAWT (Van Besssel, 1999)

Van Bussel (1999) developed the momentum theory for diffuser wind turbine in one dimension. The equivalency of this theory matches closely to conventional wind turbine. The assumption for this theory is that at the exit of the shroud (diffuser), the

conditions are applied as the same after a bare wind turbine, and also no back pressure is considered. Then the following expression referring to **Figure 3.3** is introduced:

$$V_4 = (1 - a) \tag{3.8}$$

Where a is the axial induction factor at the exit area of the shroud. The induction factor in far wake of the shroud is half of that at exit area, as mentioned in **Chapter one** for bare wind turbine, thus the far field exit velocity is as follows:

$$V_5 = (1 - 2a)V_0 \tag{3.9}$$

Using the continuity equation, and shroud (diffuser) area ratio β, then the velocity at the throat area or nozzle $V_2 = \beta V_4$, gives

$$V_2 = \beta(1 - a)\, V_0 \tag{3.10}$$

When an extra back pressure at the exit of shroud is present, then the velocity at exit leads to:

$$V_4 = \gamma(1 - a)V_0 \tag{3.11}$$

Analogous to **Equation (3.6)** for empty diffuser, the velocity at the throat then equals:

$$V_2 = \beta\gamma(1 - a)\, V_0 \tag{3.12}$$

It can be observed from **Equation (3.12)** that the amount of air passing through the turbine plane in the shroud has increased with factor $\beta\gamma$ compared to a bare wind turbine.

"The pressure relations can easily be obtained by application of Bernoulli's law in the flow in front of the rotor, and similarly in the flow behind the rotor'' (Van Bessel, 2007). As assumption is considered that the rotor plane is placed in throat area, then the pressure in the front of the rotor is:

$$p_2 = p_0 + [1 - \beta^2\gamma^2(1-a)^2]\frac{1}{2}\rho V_0^2 \tag{3.13}$$

And for the pressure behind the rotor:

$$p_3 = p_0 + [(1-2a)^2 - \beta^2\gamma^2(1-a)^2]\frac{1}{2}\rho V_0^2 \tag{3.14}$$

Therefore; the difference pressure between the upstream and downstream pressure is:

$$p_3 - p_2 = 4a(1-a)\frac{1}{2}\rho V_0^2 \tag{3.15}$$

3.3 Power and Thrust Equations for SAWT.

The power equation or the power coefficient can be easily found using the power coefficient C_p as mentioned in **Equation (1.6)** from **Chapter One**, and by applying the difference pressure equation for SAWT **Equation (3.15)**, the power coefficient for SAWT becomes:

$$C_{p,rotor} = \frac{(p_3 - p_2)V_2}{\frac{1}{2}\rho V_0^3} = \beta\gamma 4a(1-a)^2 \tag{3.16}$$

And consequently the power coefficient based upon the diffuser exist area:

$$C_{p,exist} = \gamma 4a(1-a)^2 \tag{3.17}$$

From **Equations (3.16 & 3.17),** a good relationship is obtained between power coefficients at the throat and exit area:

$$\beta = \frac{C_{p,rotor}}{C_{p,exist}} \tag{3.18}$$

An important conclusion can be seen in **Equation (3. 16)**; the power coefficient for bare wind turbine can be found by setting $\beta\gamma = 1$.

Thus the generated power:

$$P = \frac{1}{2}\rho A_r V_0^3 C_{p,rotor} \tag{3.19}$$

Where ρ is air density, A_r is the rotor swept area, V_0 is the undisturbed air velocity, and $C_{p,rotor}$ is the power coefficient for the rotor in the shroud.

The thrust force on the rotor inside the shroud is exactly the same as the thrust force on a bare rotor from **Equation** $(\mathbf{1.7})$, **Chapter 1**, and by applying the principle of conservation of momentum for the flow through SAWT leads:

$$C_T, total = \beta\gamma 4a(1-a) \tag{3.20}$$

3.4 Shroud Efficiency

The efficiency of the shroud or diffuser as described by Phillips (2003) can be obtained from applying energy balance on the shroud. Since the shrouded efficiency depends on the pressure drop at the exit shroud area and pressure just after rotor plane, diffuser efficiency can be expressed as:

$$\eta_{diff} = \frac{p_4 - p_3}{\frac{1}{2}\rho(V_3^2 - V_4^2)} \tag{3.21}$$

Where p_3 and V_3 are the pressure and velocity just after rotor plane, and p_4 and V_4 are pressure and velocity at exit shroud area.

Equation (3.21) can be applied in the presence of the actuator disk to determine the efficiency of the shroud, and an important equation for determining the efficiency of the shroud without the actuator disk has been developed by Widnall as follows in the next section (3.5).

3.5 Shroud Efficiency without Actuator Disk Based on CFD Analysis.

Widnall was able to determine the efficiency of the shroud without the presence of the rotor plane (actuator disk) by developing an equation based on Computational Fluid Dynamic (CFD) analyses and shroud exit area. A report was created by Spera (2014) based on the Widnall theory for developing this efficiency equation, Widnall described shroud area ratio AR:

$$AR = \frac{shroud\ exit\ area}{shroud\ throat\ area} \tag{3.22}$$

Actually, this shroud area ratio AR is denoted (β) in the **Equation (3.3)** by Van Bessel, and it has the same meaning. Widnall data have been curve-fit as follows in **Equation (3.23)** and as illustrated in **Figure (3.4)**

$$AF0,W = -0.070\ AR^2 + 1.614\ AR - 0.535 \tag{3.23}$$

Where AF0,W is Widnall ideal augmentation factor without rotor thrust

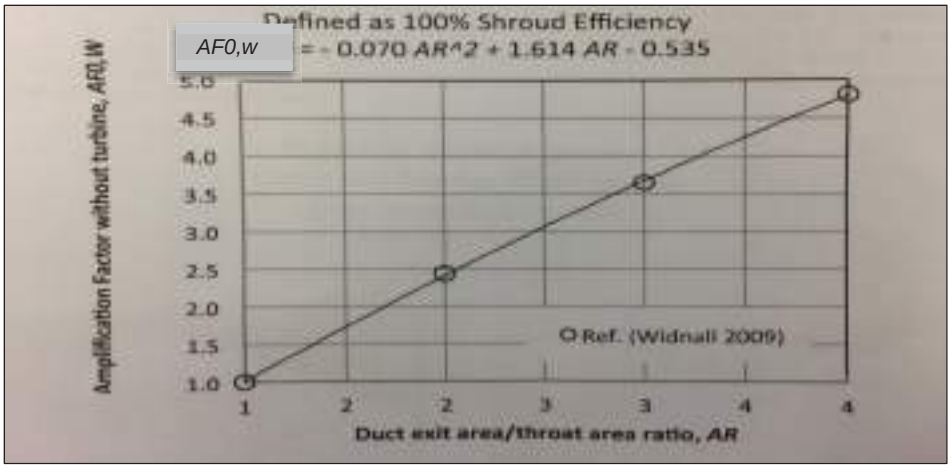

Figure 3.4 Ideal shroud airspeed amplification without turbine (Spera, 2014).

From **Figure (3.4)**, it is clear that the augmentation factor $(AF0, W)$ increases linearly with increasing the shroud area ratio.

Thus, the efficiency equating for empty shroud:

$$\eta_{empty\ diff.} = \frac{(AF0 - 1)}{(AF0, W - 1)} \tag{3.24}$$

Where, $\eta_{empty\ diff.}$ is the empty shroud efficiency in %, the AF0 is augmentation factor for a given shroud cross-sectional design without rotor thrust, and it is calculated from the average throat airspeed to the undisturbed airspeed in CFD analysis $AF0 = V_{throat}/V_0$, and AF0,W is obtained from **Equation (3.23)**.

By using **Equation (3.24)**, the shroud efficiency can be determined before continuing with further calculations of the wind turbine. In this study, **Equation (3.24)** was applied on E423 shroud (AR=2). The efficiency obtained from E423 shroud was 63.7%.

3.6 Axial Momentum Balance and the Forces Acting On the Shroud and Rotor Plane.

When the wind turbine is placed in the shroud, there will be thrust force; upstream, and downstream induced forces, which act on actuator disk. In addition to the thrust force, there is drag force acting on the duct. Thus, it is important to apply axial momentum balance for one dimension on the whole system in order to calculate these forces.

Lilly and Rainbird (1956) applied momentum balance on the shroud of a windmill by taking care of all the forces acting on the system in control volume. For bare wind turbine, and according to Lilley and Rainbird, Phillips (2003) described the momentum balance in his work by applying it to a control volume that is upstream and downstream of the rotor as shown in **Figure 3.5.**

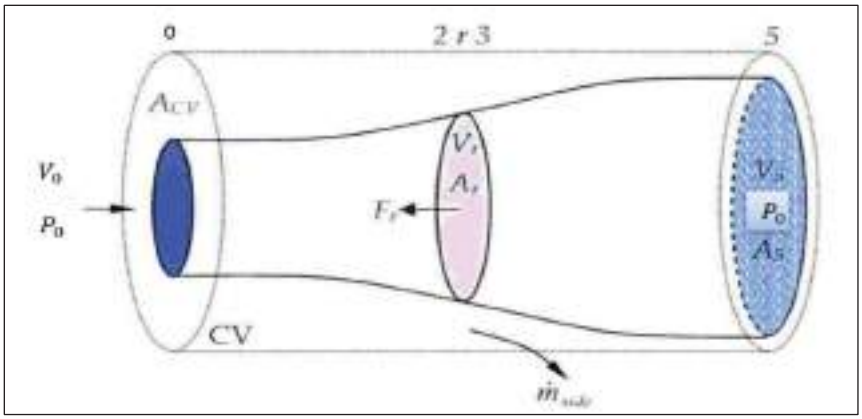

Figure 3.5 Illustration of the streamtube passing through a bare wind turbine rotor. Atmospheric pressure exists at station 0 and 5 (Philips, 2003).

The Upstream momentum balance is given by:

$$F_{us} - (p_2 - p_0)A_2 = \rho Q(V_2 - V_0) \tag{3.25}$$

Where F_{us} is the force acting on upstream flow, and Q is the volume flow rate. By applying the Bernoulli equation at upstream cross-section leads:

$$(p_2 - p_0) = \frac{1}{2}\rho(V_0^2 - V_2^2) \tag{3.26}$$

Thus

$$F_{us} = \rho Q(V_2 - V_0) + \frac{1}{2}\rho(V_0^2 - V_2^2)A_2 \tag{3.27}$$

And using the induction factor a

$$V_2 = V_0(1 - a) \tag{3.28}$$

$$F_{us} = \frac{1}{2}\rho A_2 V_0^2 a^2 \tag{3.29}$$

Similarly, the force, which is acting on downstream flow, F_{ds} can be obtained from the momentum balance downstream of the turbine:

$$F_{ds} + (p_3 - p_0)A_3 = \rho Q(V_5 - V_3) \tag{3.30}$$

$$(p_3 - p_0) = \frac{1}{2}\rho(V_5^2 - V_3^2) \tag{3.31}$$

$$F_{ds} = \rho Q(V_5 - V_3) - \frac{1}{2}\rho(V_5^2 - V_3^2)A_3 \tag{3.32}$$

And using induction factor; $V_5 = V_0(1 - 2a)$; and $V_3 = V_2$

$$F_{us} = -\frac{1}{2}\rho A_3 V_0^2 a^2 \tag{3.33}$$

Where A_3 is equal to A_2. “The axial pressure forces on the streamtube upstream of the turbine and these on the downstream part are considered separately. They can be shown to be non-zero; equal in the magnitude and opposite in sign” (Philips, 2003).

The axial momentum balance applied on a bare wind turbine can be formed for SAWT in the same manner. Philips, (2003) considered that there is a small perturbation in pressure from the free-stream pressure acting on the control volume responsible of creating axial pressure forces, as shown in **Figure 3.6**.

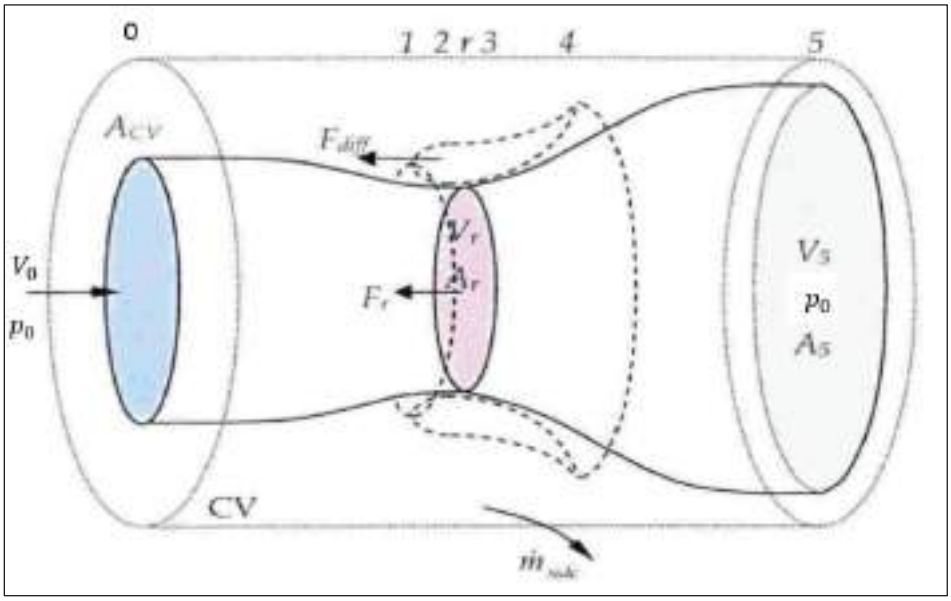

Figure 3.6 Streamtube passing through the shroud in presence of the actuator disk, and the forces in the system (Phillips, 2003).

For the upstream free-streamtube

$$F_{us} + p_0A_0 - p_2A_2 - (A_0 - A_2)p_0 = \rho Q(V_2 - V_0) \tag{3.34}$$

Where: Q=V_2A_2

$$F_{us} - (p_2 - p_0)A_2 = \rho Q(V_2 - V_0) = \rho V_0^2 A_2 \varepsilon(1 - \varepsilon) \tag{3.35}$$

Where: $\varepsilon = {}^{V_2}/_{V_0}$ is augmentation factor.

And by using Bernoulli equation between station 2 and undisturbed velocity station:

$$(p_2 - p_0) = \frac{1}{2}\rho(V_0^2 - V_2^2) = \frac{1}{2}\rho V_0^2(1 - \varepsilon^2) \tag{3.36}$$

$$F_{us} = \frac{1}{2}\rho V_0^2 A_2(1 - \varepsilon)^2 \tag{3.37}$$

The force across the rotor is represented by thrust force:

$$F_r = -(p_2 - p_3)A_r \tag{3.38}$$

Where: $A_r = A_2$

And the force which is acting on shroud on the streamtube passing through it is obtained from the integral of the axial component of pressure forces over the inner surface (Snel, 2001).

$$F_d = \iint_R p \, dr \, d\theta$$

$$= \left(p_0 + \frac{1}{2}\rho V_0^2\right)(A_4 - A_3) - \frac{1}{2}\rho Q^2 \left(\frac{A_4 - A_3}{A_4 A_3}\right) \tag{3.39}$$

In reality, this force is the drag force on the shroud, which is also described, by Lubitz and Shomer (2014) in easier form as:

$$F_d = \frac{1}{2} C_d \rho \frac{\pi}{4} (D_4^2 - D_2^2) V_0^2 \tag{3.40}$$

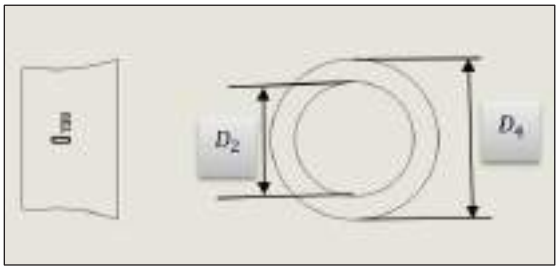

Figure 3.7 Frontal cross sectional area of E423 shroud.

Where F_d is the drag force, C_d is drag coefficient obtained experimentally, V_0 is undisturbed air velocity, D_4 and D_2 are the diameters of the exit plane and throat plane of the shroud, respectively.

For downstream (post-expansion) free-streamline

$$F_{ds} + p_4 A_4 - p_0 A_5 + (A_5 - A_4) p_0 = \rho Q (V_5 - V_4) \tag{3.41}$$

$$F_{ds} - (p_4 - p_0) A_4 = \rho Q (V_5 - V_4) \tag{3.42}$$

Using exit pressure coefficient represented by:

$$Cp_4 = \frac{p_4 - p_0}{\frac{1}{2} \rho V_0^2} \tag{3.43}$$

$$F_{ds} = -Cp_4 \frac{1}{2} \rho V_0^2 V_4 + \rho V_0^2 V_2 \left(\frac{V_5}{V_0} - \frac{V_4}{V_0} \right) \tag{3.44}$$

Bernoulli equation in the downstream:

$$p_4 - p_0 = \frac{1}{2}\rho(V_5^2 - V_4^2) \tag{3.45}$$

And using $\varepsilon = {}^{V_2}/_{V_0}$,$\beta = {}^{A_4}/_{A_2}$ and continuity equation between station (4 &2).

Where $\lambda = {}^{A_2}/_{A_4}$ is described by Phillips (2003), then $\lambda = {}^{1}/_{\beta}$

$$Cp_4 = \frac{\frac{1}{2}\rho(V_5^2 - V_4^2)}{\frac{1}{2}\rho V_0^2} = \left(\frac{V_5}{V_0}\right)^2 - \left(\frac{V_4}{V_0}\right)^2 = \left(\frac{V_5}{V_0}\right)^2 - \left(\frac{V_4}{V_2}\frac{V_2}{V_0}\right)^2$$

$$= \quad Cp_4 = \left(\frac{V_5}{V_0}\right)^2 - \varepsilon^2\beta^2 \tag{3.46}$$

Where: $\frac{V_5}{V_0} = [Cp_4 + \varepsilon^2\beta^2]^{1/2}$, Thus:

$$F_{ds} = \frac{1}{2}\rho V_0^2 A_2 \left[2\varepsilon\left\{[Cp_4 + \varepsilon^2\beta^2]^{1/2} - \varepsilon\beta\right\} - \frac{1}{\beta}Cp_4\right] \tag{3.47}$$

Where the continuity equation is $A_2V_2 = A_4V_4$, and thus ($\frac{V_2}{V_4} = \frac{A_4}{A_2} = \beta$)

The final momentum balance is obtained by summation of all terms:

$$F_{ds} + F_r + F_d + F_{ds} = \rho\, Q(V_5 - V_0)$$

$$F_{ds} + F_r + F_d + F_{ds} = \rho\, \varepsilon\, V_0 A_2(V_5 - V_0) \tag{3.48}$$

Note that, the momentum balance can be applied on empty shroud (without rotor) using **Equation (3.48)** with some simplifying changes such as $F_r = 0$ and $p_2 = p_3$

CHAPTER 4

EXPERIMENTAL MODELING

Experimental investigations on the micro-shroud included measurement the air velocity distribution inside the shroud at the throat and also measurement of a small turbine with and without the shroud. A low speed wind tunnel was used for the experiments. Before testing the shroud, the velocity distribution inside the entire wind tunnel was mapped to establish the test section area with fully developed flow.

4.1 Wind Tunnel

The advances in computational fluid dynamics (CFD) modelling on high speed digital computers have reduced the demand for wind tunnel testing. However, CFD results are still not completely reliable and wind tunnels are used to verify the CFD computer codes. The wind tunnels are usually designed for a specific purpose and speed range. The most common tunnels are for icing research, as well as for subsonic, supersonic, and hypersonic flow. A wind tunnel may be open and draw air from outside the tunnel into the test section and then exhaust back to the outside, or the tunnel may be closed with the air recirculating inside the tunnel (Shah et al, 2013).

4.1.1 Wind Tunnel Configurations

The wind tunnel which was available at Youngstown State University is an open, and low air speed tunnel with small size of dimensions (16’ x 4’ x 4’). The aluminum structure of the side walls are covered by thick glass sheets to become a good monitor during the test as shown in **Figure 4.1**. The wind tunnel consists of an axial fan (Cincinnati Fan –Size 48) which is powered by a 10 horsepower motor in a 4 feet diameter housing as shown in **Figure 4.2**. The wind tunnel is capable of generating wind speeds up to 34 mph.

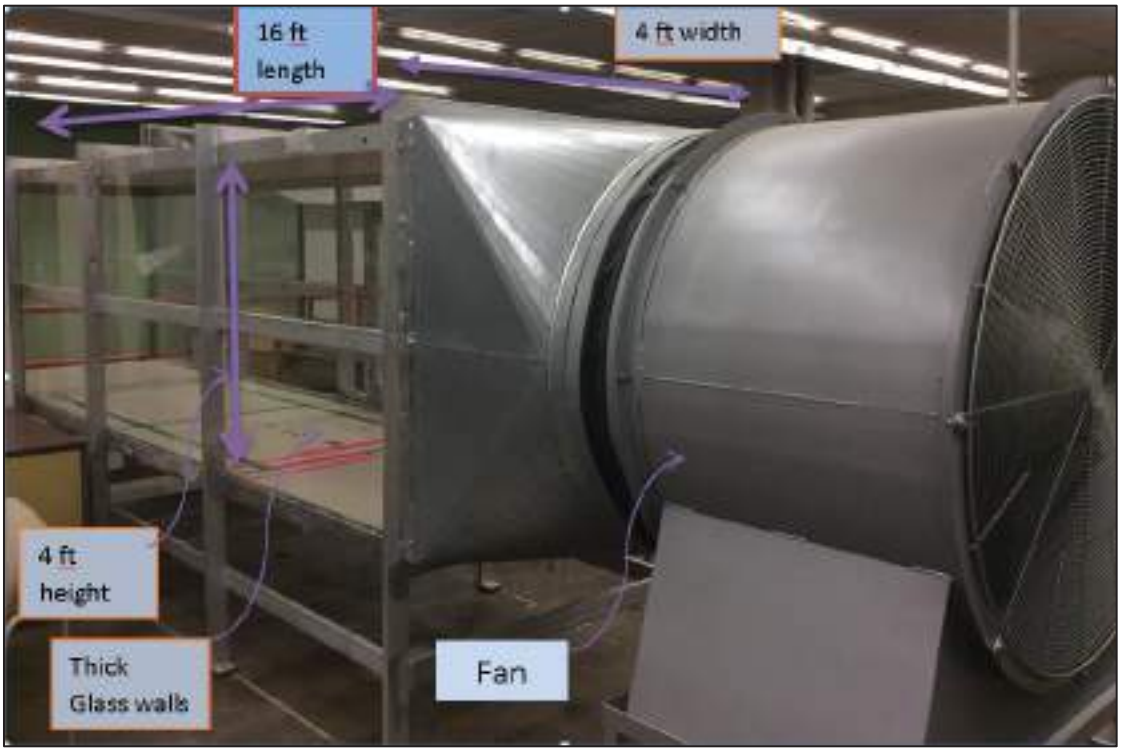

Figure 4.1 Low speed wind Tunnel at YSU

Figure 4.2 Axial Fan (Cincinnati Fan –Size 48, 10 hp)

The Motor Fan was controlled by a small computer. The LabVIEW v8.6 software was used to control the wind tunnel, including switching on the fan and controlling the speed, as shown in **Figure 4.3**, while reversing the fan direction was done manually from the fan system VFD.

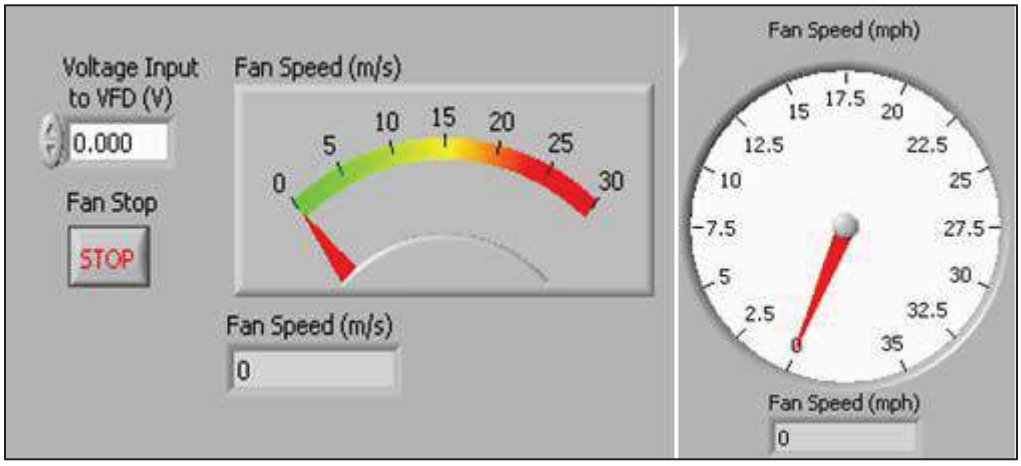

Figure 4.3 LabVIEW software screen (Fan control screen)

4.1.2 Experimental Apparatus (Preparations and Tools)

4.1.2.A Data Acquisition Device

The preparation for the first experiment required a setup of the wind tunnel with computer software. The apparatus that was used to receive and transform the information to the LabVIEW (computer) was DAQ (Data Acquisition device)(NI cDAQ-9172, module NI 9264) as shown in **Figure 4.4**. The DAQ hardware acts as the interface between a computer and signals from the outside world. It primarily functions as a device that digitizes incoming analog signals so that a computer can interpret them. The three key components of a DAQ device used for measuring a signal are the signal conditioning circuitry, analog-to-digital converter (ADC), and computer bus. There are many DAQ devices used for various functions such as, automating measurement systems and processes (National Instruments, 2014).

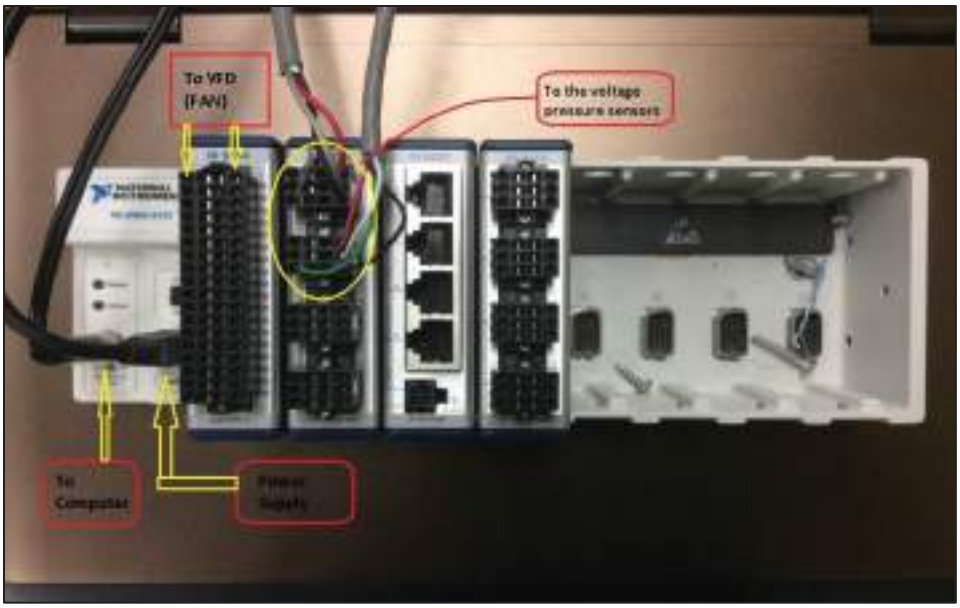

Figure 4.4 Data Acquisition device (DAQ)

The Fan was run by a variable frequency drive (VFD)(Allen Bradley Model PowerFlex-4M) connected to the DAQ in order to control the fan speed by LabVIEW (computer software). DAQ permitted an input voltage to the fan which varied from 0 to 8 V DC. Also, the frequency input for the VFD has an input range, from 0 to 80 Hz, which is capable of providing wind speeds up to 34 mph from the fan.

4.1.2.B Pitot- Static Tube and Pressure Sensors

Pitot static tube (166-12,1/8" diameter, 12" insertion Depth, 3" tip length) was used to measure the static and total pressure in order to calculate the air speed inside the wind tunnel at specific points. A Pitot- static tube is a device which enables the measurement of the dynamic pressure of a fluid in motion, such as the air flow around a moving vehicle or stationary object exposed to air flow. A Pitot- static tube has two ports; static pressure (P_{static}) and total pressure (P_{total}) as shown in **Figure 4.5(a)**. The difference between these two pressures is the dynamic pressure which is used to determine wind speed. Connecting a differential pressure transducer across the two ports will therefore measure $P_{dynamic}$ directly (PI Research, 2014).

(a) (b)

Figure 4.5 Experimental apparatus: (a) Pitot- static tube (FlowKinetics, 2015). (b) MLV series Low voltage pressure sensors (Mouser Electronics, 2011)

The Pitot - static tube was connected to a pressure sensor through thin plastic tubing (1/8" dia.). The MLV (Magnetic Low Voltage) series, low voltage pressure sensors, as shown in **Figure 4.5(b)**, wired to the DAQ, which transfers the signal to the computer software (LabVIEW). Two Pitot-static tubes and pressure sensors were used in the experiment.

4.1.2.C Unit Conversions and Velocity Calculations

The unit conversions were done in LabVIEW to change the dynamic pressure readings and then to equivalent air flow measurements. The unit conversions sequence is as shown in **Figure 4.6**, and **Figure 4.7,** which illustrates the operating LabVIEW front panel.

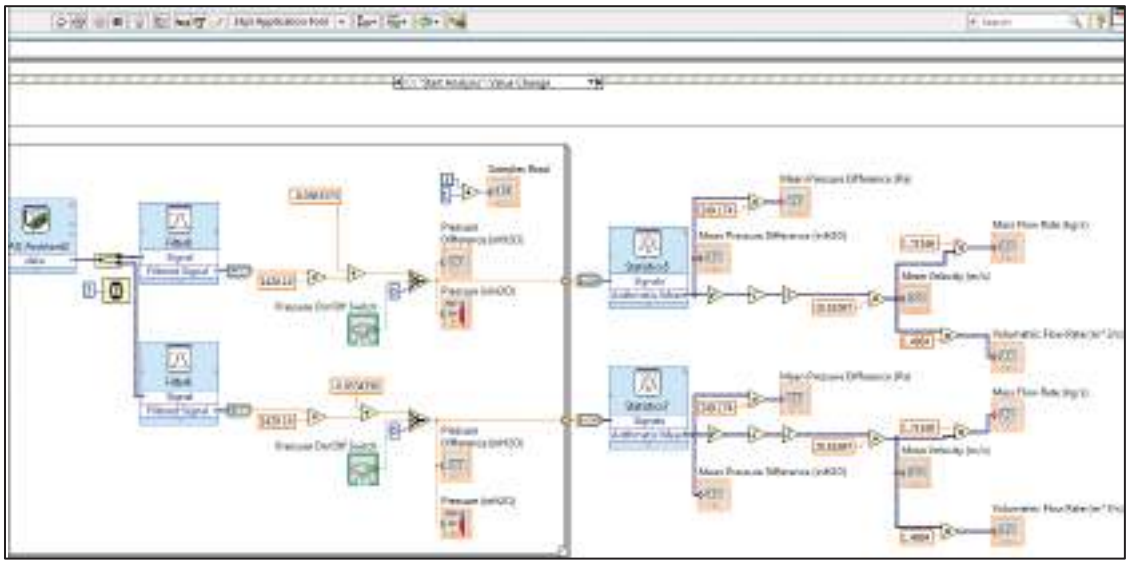

Figure 4.6 LabVIEW diagram of low airspeed wind tunnel. This program was designed to run the wind tunnel and measure the pressure differences.

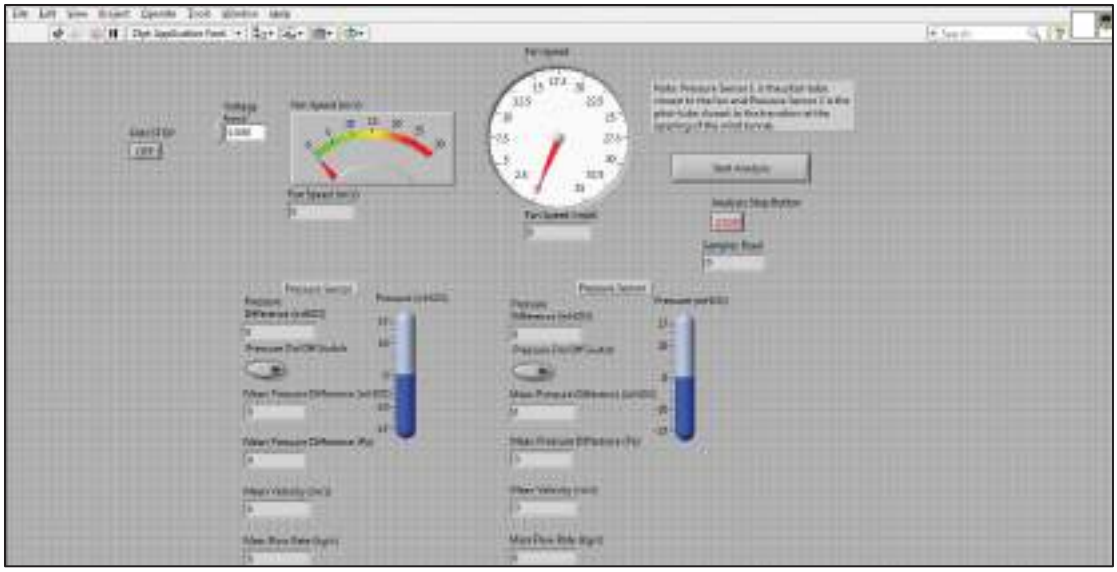

Figure 4.7 LabVIEW operating panel of low airspeed wind tunnel. This panel shows the direct measurements of the pressure differences, velocity, and mass flow rate.

The conversion of dynamic pressure measurements to air speed values can be calculated from Bernoulli's equation:

$$P_{dynamic} = \frac{1}{2}\rho V^2 \tag{4.1}$$

Where ρ is the air density. Solving for velocity and inserting correct unit conversion, the air velocity is calculated as such:

$$V = 1096.7\sqrt{\frac{P_{dynamic}}{d}} \tag{4.2}$$

Where:

$$d = 1.325\ \frac{P_B}{T}$$

V: velocity in feet per minute, $ft/\min$

$P_{dynamic}$: dynamic pressure in inch of water, inH2O

d: Density of air in pound per cubic foot

P_B: Barometric (or absolute) static pressure in inch of mercury. It is approximately 29.9 inches of mercury with dry air at 73 °F

T: absolute temperature (indicated temperature in °F plus 460°). The temperature at wind tunnel was 73.7°F .

Therefore;

$$V = 4025.252\sqrt{P_{dynamic}} \qquad ft/\min \tag{4.3}$$

$$V = 20.448\sqrt{P_{dynamic}} \qquad meter/sec \tag{4.4}$$

4.1.2.D Turnbuckle and Pitot tube clamps

In order to measure the dynamic pressure and consequently the air speed at points in the cross-section inside the wind tunnel, a movable weld-mount turnbuckle (5200 Ib, ¾'' dia., 29'' closed length) was used as shown in **Figure 4.8 (a).** The two ends of the turnbuckle were provided with swivel leveling mounts (standard, stud with threaded Hole). These levels had pads under the base to reduce noise and absorb vibrations as shown in **Figure 4.8(b)**. Also the base has a ball and socket nut that allows the stud to swivel 15 degree to compensate correctly on the walls.

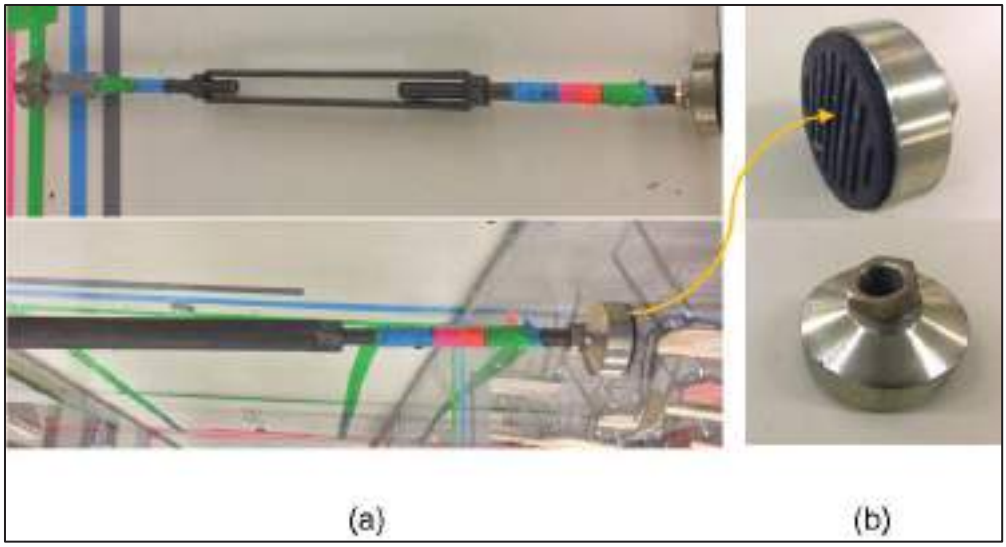

Figure 4.8 Experimental tools (a) weld-mount turnbuckle (5200 Ib, ¾'' dia., 29'' closed length) (b) Swivel leveling mounts, with vibration reducing pads.

The turnbuckle was setup horizontally which could be moved up and down as shown in **Figure 4.8 (a)**. There was a multi-mount clamp which allowed the Pitot tube to rotate 360 degrees as shown in **Figure 4.9**, and also allowed the Pitot tube to move up and down. The multi –mount clamp was movable along the turnbuckle and thus easy to set at any desired position.

Figure 4.9 Multi-mount clamp

4.1.3 Wind Tunnel Schematic

The experimental tools and devices were set and installed properly to achieve accurate results of the dynamic pressure measurements**. Figure 4.10** shows the setup of instrumentation block diagram, based on measuring the airspeed distribution in the selected section inside the wind tunnel. The block diagram includes the apparatuses that were used in the experiment. The block diagram for the LabVIEW software is as shown in **Figure 4.6**, and the front panel design is as shown in **Figure 4.7**.

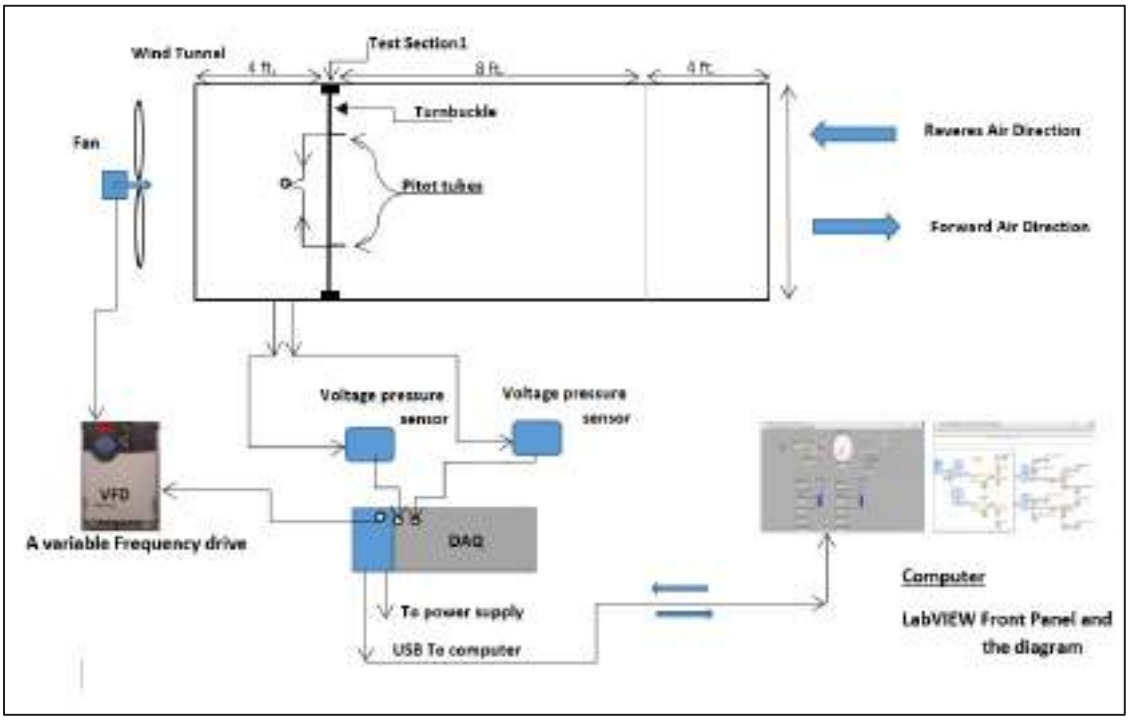

Figure 4.10 Schematic of the experimental wind tunnel setup

4.2 Measurement of Velocity Distribution inside Wind Tunnel

The first experiment was performed to determine the most consistent testing section area in wind tunnel. Two sections were tested with the air flow in both the positive and negative axial directions. The first section was four feet from the fan, and the second

section was twelve feet from the fan, close to the open end, as shown in **Figure 4.12.** According to Dwyer for installation and operating instructions each section was divided to 81 points since in practical situations, the velocity of the air stream is not uniform across the cross section of a duct. Friction slows the air moving close to the walls, so the velocity is greater in the center of the duct. To obtain the average total velocity in ducts of 4" diameter or larger, a series of velocity pressure readings must be taken at points of equal area. A formal pattern of sensing points across the duct cross section is recommended as shown **Figure 4.11.**

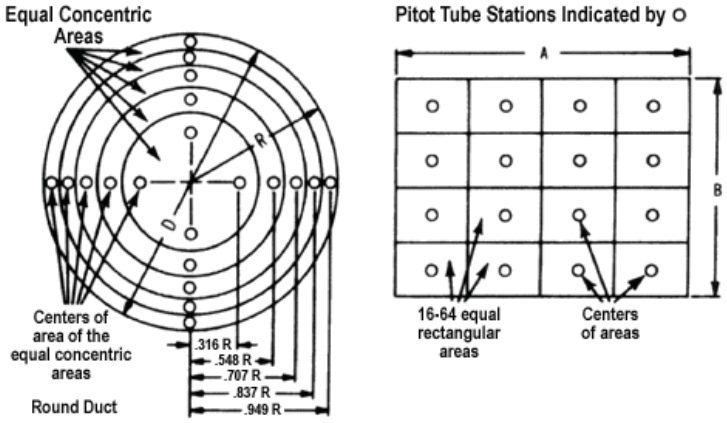

Figure 4.11 Traverse on round and square duct areas (Dwyer)

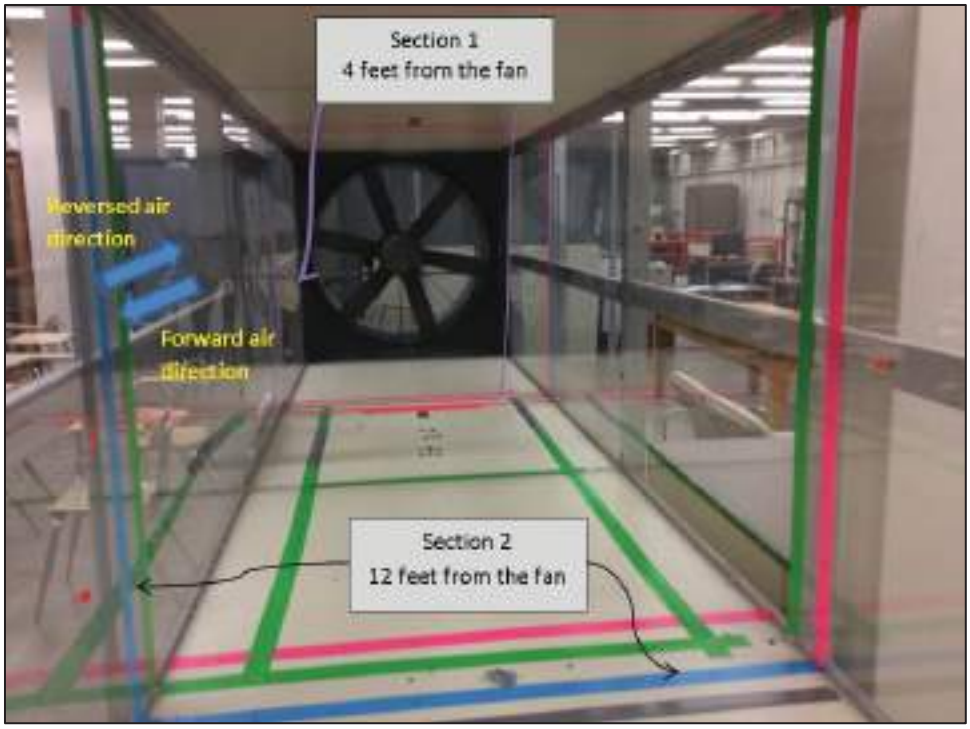

Figure 4.12 Test Sections inside Wind Tunnel

Two Pitot static tubes were used as shown in **Figure 4.13 (a)**. They were aligned at each point of the cross-section by using thin strings to make sure that tip length was parallel to the flow direction under allowable angle so that the total pressure port was facing the flow, as shown in **Figure 4.13 (b).** The wind tunnel, controlled by an input voltage of 5.5 volts, was run at fan airspeed of 4.4 miles per hour.

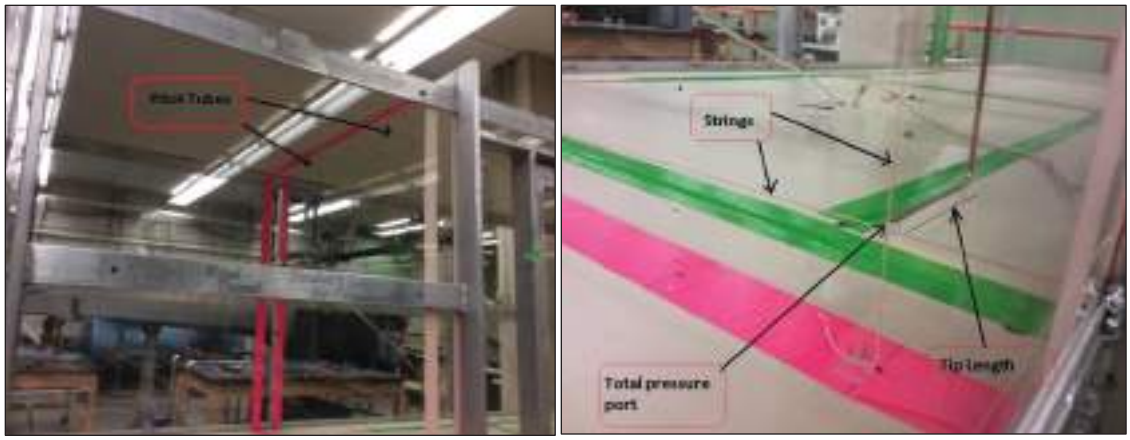

(a) (b)

Figure 4.13 The Pitot tubes installation: (a) Two Pitot static tubes installed in testing section1.(b) Pitot tube alignment by using strings.

The first section with reverse air direction was the best section for testing the shroud. The velocity profile was fully developed in this section, so it was decided to place the shroud at its center. The graphic plot of the first section is shown in **figure 4.14,** and the other section test plots are attached in **Appendix A**. The maximum velocity in center of section1 reached 9.1 m/s, and minimum velocity was 4.3 m/s close to the walls for a control voltage of 5.5 volts.

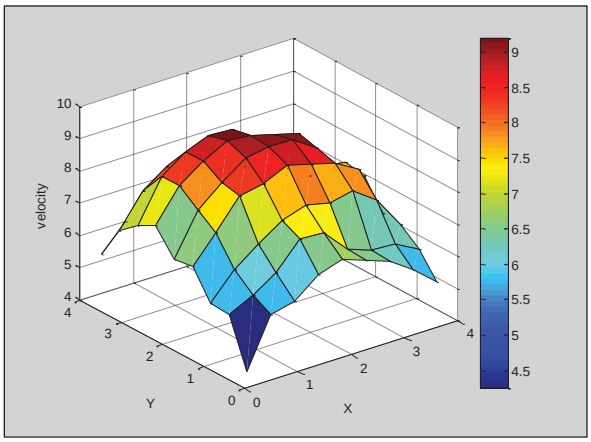

Figure 4.14 Air velocity distribution at section1 (reverse direction)

4.3 Empty Micro-Shroud Experiment

4.3.1 Manufacturing of the Experimental Shroud Model

The shroud model was designed in SolidWorks based on the coordinates of the airfoil E423. To create the full solid body, the sketch was positioned with respect to an axisymmetric center-line. The experimental shroud size was a result of scaling down a full optimum size with scale factor of 0.0265 because the wind tunnel was not large enough to test full size. The throat radius (R_{throat}) of experimental shroud model was 4.46 inches, and the length (L) was 7.18 inches resulting in L/R_{throat} of 1.6. The shroud expansion angle, α was 8.96° giving outlet and inlet area ratio (β) of 2, as shown in **Figure 4.15**. After the model was designed in SolidWorks, it was printed in a 3D printer machine (MAKERBOT REPLICATOR 2X) to get more precise configurations for the model. Because of the 3D printer size, the shroud was printed in 8 pieces and then glued and taped together to get a rigid, sustainable experimental part. **Figure 4.16. (1-6)** depicts some stages of creating the experimental shroud model.

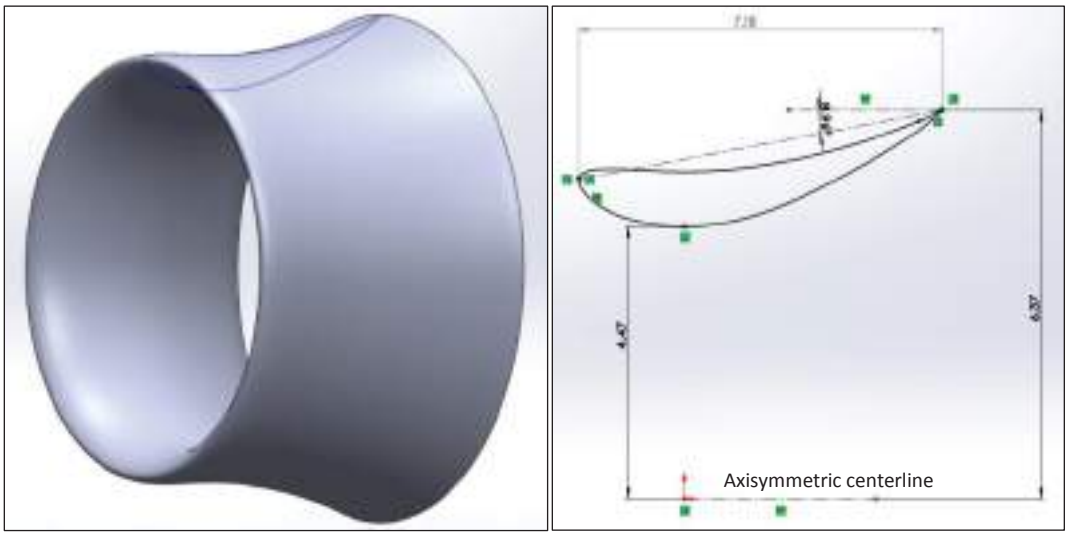

Figure 4.15. Configurations of the Experimental Shroud Model

Figure 4.16 Experimental shroud (Shroud manufacturing steps): (1-2) glued parts together (3) sand the surfaces to be smooth (4) taped the whole model (5-6) complete model

4.3.2 Experimental Setup and Method

The shroud was setup in the testing section, 4 feet from the fan, as a result of the first experiment showing this section had fully developed velocity when the air direction was reversed (backward). Thus, it was the recommended section for testing the shroud. **Figure 4.17** shows the shroud in the wind tunnel of this section. In order to measure the velocity distribution inside shroud throat area, two Pitot tubes were used. One of them was placed inside the shroud and the other was placed 5 inches just in the front of it. The velocity readings were taken along the radial axis at throat region since the shroud has axis-symmetric, as shown in **Figure 4.18**.

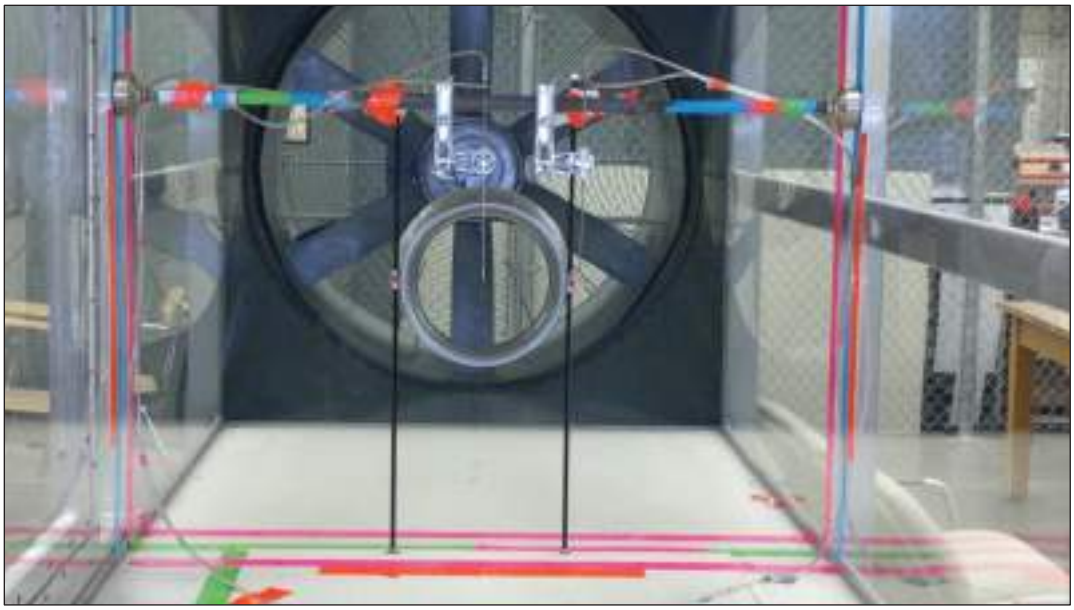

Figure 4.17 Shroud placed in test section1

Figure 4.18 Pitot static tubes placed inside and outside the shroud

4.3.3 Operating conditions

The wind tunnel was run under input voltage 5.5 volts, which provides airspeed of producing maximum air velocity 16.4 m/s inside the shroud. The Reynolds number for wind tunnel was $5.87\ x\ 10^5$ where the mean air velocity at 5.5 volts was 7.33 m/s inside

wind tunnel. Based on this mean air velocity (7.33 m/s), Mach number was 0.0213. The Mach number was so small since the wind tunnel was running at low airspeed.

4.4 Micro-Shroud Testing with Existing Small Turbine

In the third experiment, a micro-wind turbine was built in order to measure the extracted power without a shroud and then with this turbine inside the shroud throat area. The micro turbine consisted of a small generator (3000 rev/min, 12V-24V, 31mm diameter, 3.175mm shaft diameter, and 52 mm length), as shown in **Figure 4.19(a)**. The model turbine has three blades, modeled from NACA 4415 airfoil profile with angle of attacks variant between 2.8° and 27°. The blades and nacelle were sketched in SolidWorks, and then printed in 3D printer (MAKERBOT REPLICATOR 2X), as shown in **Figure 4.19(b)**

Figure 4.19 Micro-wind turbines: (a) Micro Generator (b) Three blades of airfoil NACA4415 and Nacelle

The length of each blade was 109 mm in order to fit on the shroud throat area. The clearance was approximately 2mm between the shroud inner perimeter and tip blade.

Three different voltage multi-meters were used to measure the voltage and the current, as shown in **Figure 4.20**

Where :

Power (P) = Voltage (v) x Current (I) (4.5)

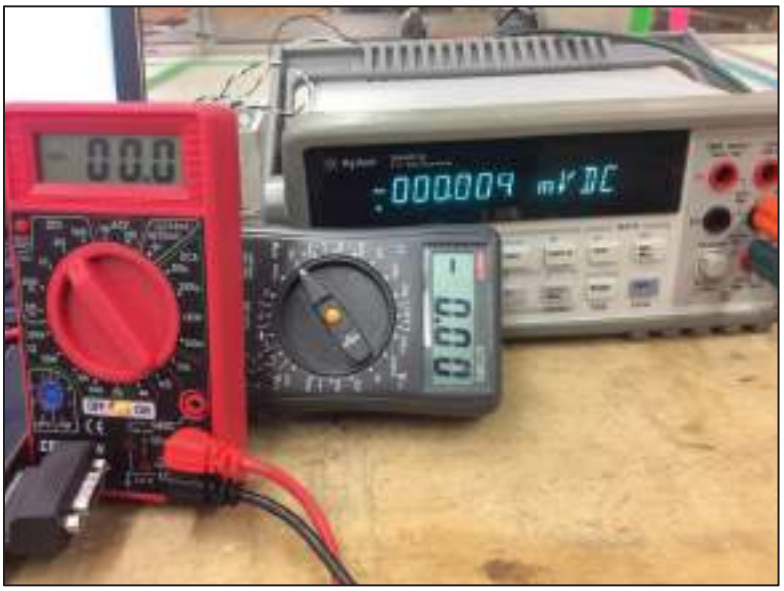

Figure 4.20. Three different voltage-current Multi-meters

Both the bare wind turbine and shrouded wind turbine were placed in the test section in the wind tunnel. A Pitot tube was put just 5 inches before the turbine to measure the inlet velocity as shown in **Figure 4.21**.

(a) (b)

Figure 4.21 Both turbines placed in testing section of the wind tunnel: (a) Micro-shrouded wind turbine (b) Micro-bare wind turbine

CHAPTER 5

COMPUTATIONAL ANALYSIS OF THE SHROUD E423 DESIGN

Computational Fluid Dynamic (CFD)

5.1. Introduction

Computational fluid dynamics (CFD) is process by which numerical solution to fluid flow problems are obtained by the use of computers. The advanced computers with large memory and high speed have enabled CFD programs to achieve solution to many flow problems such as those that are compressible or incompressible, laminar or turbulent (Ganis, 2003). CFD analysis employs a number of algorithm equations, which replace the differential equations. The differential equations for fluid flow problems are the continuity (conservation of mass), Navier-Stokes (conservation of momentum), and the conservation of energy equations. The numerical method used corresponds to the finite volume and finite difference method when using the commercially available code ANSYS FLUENT. In turbulence modeling, the standard $\mathbf{K-\varepsilon}$ and $\mathbf{K-\omega}$ turbulence models were used in this study. In 2-Dimensional analysis, the standard $\mathbf{K-\varepsilon}$ turbulence model is a widely accepted model for turbulent flow simulation in CFD because it is used for fully turbulent flow (high Reynolds number) where the Reynolds number in this analysis was high as discussed in **Chapter 4**, reference, **section 4.3.3**.

5.2. Governing Equations in CFD

5.2.1 Mass and Momentum Conservation Equations

The fluid motion can be described by the dynamic equations for fluid. The conservation of mass or continuity equation states that the local rate of change of mass within the control volume, plus the net rate of mass entering and leaving the open control surface must equal zero. It can be expressed mathematically:

$$\frac{\partial}{\partial t}\int_{cv} \rho \, dv + \int_{cs} \rho \, . \, dA = 0 \tag{5.1}$$

It can be writing as:

$$\frac{\partial \rho}{\partial t} + \nabla . (\rho \bar{V}) \tag{5.2}$$

Where: dv : Mass of element volume

dA : Mass of element surface area

$\frac{\partial \rho}{\partial t}$: Rate of density change inside the control volume

∇ : Vector operation in Cartesian coordinates $\left(\nabla = \frac{\partial}{\partial x}\vec{\imath} + \frac{\partial}{\partial y}\vec{\jmath} + \frac{\partial}{\partial z}\vec{k}\right)$

$\nabla . (\rho \bar{V})$: Net flow across boundaries of control volume

$\bar{V}$: Velocity vector

The velocity vector $\bar{V}$ in the **Equation 5.2** is described in local velocity components of 2-dimension, *u*, and *v* which are represented in Cartesian coordinate system (*x*, *y*) and time (*t*). Since the analysis in this paper was 2D axisymmetric, the continuity equation must be expressed in polar coordinate:

$$\frac{\partial \rho}{\partial t} + \frac{\partial (\rho \mathrm{v}_x)}{\partial x} + \frac{\partial (\rho \mathrm{v}_r)}{\partial r} + \frac{\rho \mathrm{v}_r}{r} = S_m \tag{5.3}$$

Where, *r* is the radial coordinate, *x* is the axial coordinate, v_x is the axial velocity, v_r is the radial velocity, and S_m is the source term.

The conservation of momentum equation can be obtained by applying the fundamental principles of Newton's second law of motion to the fluid domain. Newton's second law states that the net force on an element, or a particle, is equal to the time rate of change of its linear momentum. This law can be applied to a fluid particle moving through 3-dimensional space where the total momentum of any system, the instant directly prior to an event will equal the total moment of the system in the instant immediately after event. The net force on the particle, or object, in the *x*-direction is equal to the time rate of change of its linear momentum in the *x*- direction. The conservation of momentum equation can be written in general form (Cartesian coordinates):

$$\frac{\partial \rho V}{\partial t} + \nabla . \rho \vec{V} V = -\nabla p + \rho g + \nabla \tau \tag{5.4}$$

Where, V is general velocity component, p is the pressure, g is the gravity, and τ is the shear stress.

5.2.2 Navier-Stokes' Equation for Axisymmetric Analysis

The 2-D and 3-D incompressible Navier-stoke Cartesian equations cause the weak solution based on the regularity assumed for velocity. According to Ukhovskii (1968), if the initial data and the domain are symmetric and θ-component of initial velocity is zero, then the solution becomes regular. In this study, the shroud E423 was cylindrically symmetric and the domain kept symmetric so that there was no θ-component of velocity. According to this assumption, a weak solution becomes indeed a strong solution. The axisymmetric conservation of momentum equation can be expressed:

$$\frac{\partial(\partial v_x)}{\partial t}+\frac{1}{r}\frac{\partial(r\rho v_x v_x)}{\partial x}+\frac{1}{r}\frac{\partial(r\rho v_r v_x)}{\partial r}$$

$$=-\frac{\partial(p)}{\partial x}+\frac{1}{r}\frac{\partial\left[r\mu\left\{2\frac{\partial(v_x)}{\partial x}-\frac{2}{3}(\nabla.v)\right\}\right]}{\partial x}+\frac{1}{r}\frac{\left[r\mu\left\{\frac{\partial(v_x)}{\partial r}+\frac{\partial(v_r)}{\partial x}\right\}\right]}{\partial x}$$

$$+F_x \tag{5.5}$$

For axisymmetric flow, there is no flow in the θ -direction and all θ derivatives are identically zero. So it is considered only two variables, *r* the radial direction and *x* the axial direction.

5.2.3 Turbulence Modelling – Eddy viscosity

5.2.3. A. $K-\varepsilon$ (K- epsilon) Turbulence Model

The $\boldsymbol{K-\varepsilon}$ turbulence model is based upon the exact transport equations for the turbulence kinetic energy *K* and its dissipation rate $\boldsymbol{\varepsilon}$ (Sveningsson, 2003). P. Bulat and V. Bulat (2013) stated that, in the standard *K* - epsilon turbulence model, viscosity is determined by a single characteristic linear turbulence scale; in reality all scales of motion contribute to turbulent diffusion.

The modelled *K* and ε equations expressed:

$$\frac{\partial k}{\partial t}+u_j\frac{\partial k}{\partial x_j}=\frac{\partial}{\partial x_j}\left(\left(v+\frac{v_t}{\sigma_k}\right)\frac{\partial k}{\partial x_j}\right)+P_k-\varepsilon \tag{5.6}$$

$$\frac{\partial \varepsilon}{\partial t}+u_j\frac{\partial \varepsilon}{\partial x_j}=\frac{\partial}{\partial x_j}\left(\left(v+\frac{v_t}{\sigma_\varepsilon}\right)\frac{\partial \varepsilon}{\partial x_j}\right)+\frac{C_{\varepsilon1}P_k-C_{\varepsilon2}\varepsilon}{\mathcal{T}} \tag{5.7}$$

Where: $\mathcal{T}$: turbulent time scale ($\mathcal{T}\geq 6\sqrt{{}^{\nu}/_{\varepsilon}}$)

P_k : Production turbulent kinetic energy $P_k = 2v_t S^2$, $S^2 = S_{ij} S_{ij}$

S_{ij} : Symmetric part of the mean strain rate tensor, $S_{ij} = \frac{1}{2}\left(\frac{\partial U_i}{\partial x_j} + \frac{\partial U_j}{\partial x_i}\right)$

v : Kinematic viscosity

v_t : Kinematic turbulent viscosity

U_i, U_j: Mean velocity in x, y-direction respectively

The standard $K-\varepsilon$ model coefficients were kept as a default in shroud analysis:

$$C_\mu = 0.09, \quad C_{\varepsilon 1} = 1.44, \quad C_{\varepsilon 2} = 1.92, \qquad \sigma_k = 1.0, \ \sigma_\varepsilon = 1.3$$

5.2.3. B. $K-\omega$ (k-Omega) Turbulence Model

K -Omega model is the same the $K-\varepsilon$ model, but it employs equation for the turbulent energy dissipation rate (omega) instead of dissipation equation $\boldsymbol{\varepsilon}$.

The modelled K and ω equations expressed:

$$\frac{\partial k}{\partial t} + u_j \frac{\partial k}{\partial x_j} = \frac{\partial}{\partial x_j}\left((\nu + \sigma^* \nu_t)\frac{\partial k}{\partial x_j}\right) + P_k - \beta^* \omega k \tag{5.8}$$

$$\frac{\partial \omega}{\partial t} + u_j \frac{\partial \omega}{\partial x_j} = \frac{\partial}{\partial x_j}\left((\nu + \sigma \nu_t)\frac{\partial \omega}{\partial x_j}\right) + \gamma \frac{\omega}{k} P_k - \beta \omega^2 \tag{5.9}$$

Where: $\nu_t = \gamma^* \frac{k}{\omega}$

According to P. Bulat and V. Bulat, (2013), K - [omega] SST (Shear Stress Transport) turbulent is essentially a union of the two models (k-[epsilon] away from the walls and the k-[omega] in the wall region). Researchers, who use standard SST model, typically find that it shows good results in mixing layers at medium pressure gradients.

The standard $K-\boldsymbol{\omega}$ model coefficients are:

$$\beta = {}^{3}/_{40},\ \beta^{*} = {}^{9}/_{100},\ \gamma = {}^{5}/_{9},\quad \gamma^{*} = 1,\quad \sigma = 0.5,\qquad \sigma^{*} = 0.5$$

CFD Methodologies

5.3 Fluent Solver Algorithms

The FLUENT solver has provided two basic solver algorithms: The first is a density-based coupled solver (DBCS) that uses the solution of the coupled system of fluid dynamics equations (continuity, momentum and energy); the second is a pressure-based algorithm solver (PBCS) that solves the equations in a segregated or uncoupled manner. The segregated pressure-based algorithm has proven to be both robust and versatile, and it has been utilized in concert with a wide range of physical models, including multiphase flows, conjugate heat transfer and combustion (Kelecy, 2008*).* The pressure-based solver in ANSYS-FLUENT is used for most incompressible flows, while the density-based solver is used for compressible flows. **Figure 5.1** Shows the overall flowchart of fluent solver algorithms.

Since there was no heat included in this analysis of study, and the flow over the shroud was incompressible, then the pressure- based solver was used and the energy equation was turned off.

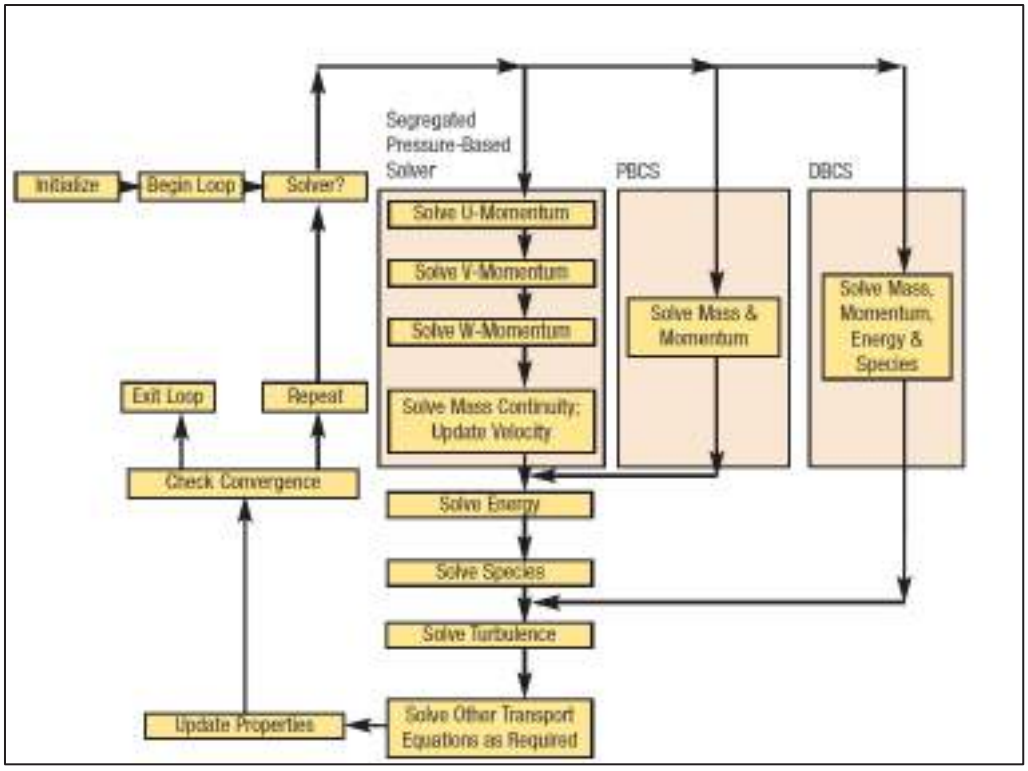

Figure 5.1 Overall flowchart of fluent solver algorithms (Kelecy, 2008)

5.4 Pressure –Based Solver

The pressure-based solver uses an algorithm, which classified as general classic method called the projection method. Based on this method, the continuity (or mass) equation represented by the velocity field is obtained by solving the pressure correction equation. In order to satisfy the continuity equation, the velocity field should be corrected by the pressure field. Also, in the momentum equation, the process of solving velocity field is the same as in continuity equation. Because the governing equations are non-linear and coupled to one another, they are solved frequently with the required number of iterations until the solution reaches the convergence (Fluent Inc., 2013-2014).

The Ansys-Fluent includes two pressure based solver algorithms; a segregated algorithm and a coupled algorithm, as shown in **Figure 5.2**. In the Pressure-Based Segregated Algorithm,

> The pressure-based solver uses a solution algorithm where the governing equations are solved sequentially (that is, segregated from one another). Unlike the segregated algorithm described above, the pressure-based coupled algorithm solves a coupled system of equations comprising the momentum equations and the pressure-based continuity equation. Thus, in the coupled algorithm, Steps 2 and 3 in the segregated solution algorithm are replaced by a single step in which the coupled system of equations are solved. The remaining equations are solved in a decoupled fashion as in the segregated algorithm. (Fluent Inc., 2013-2014)

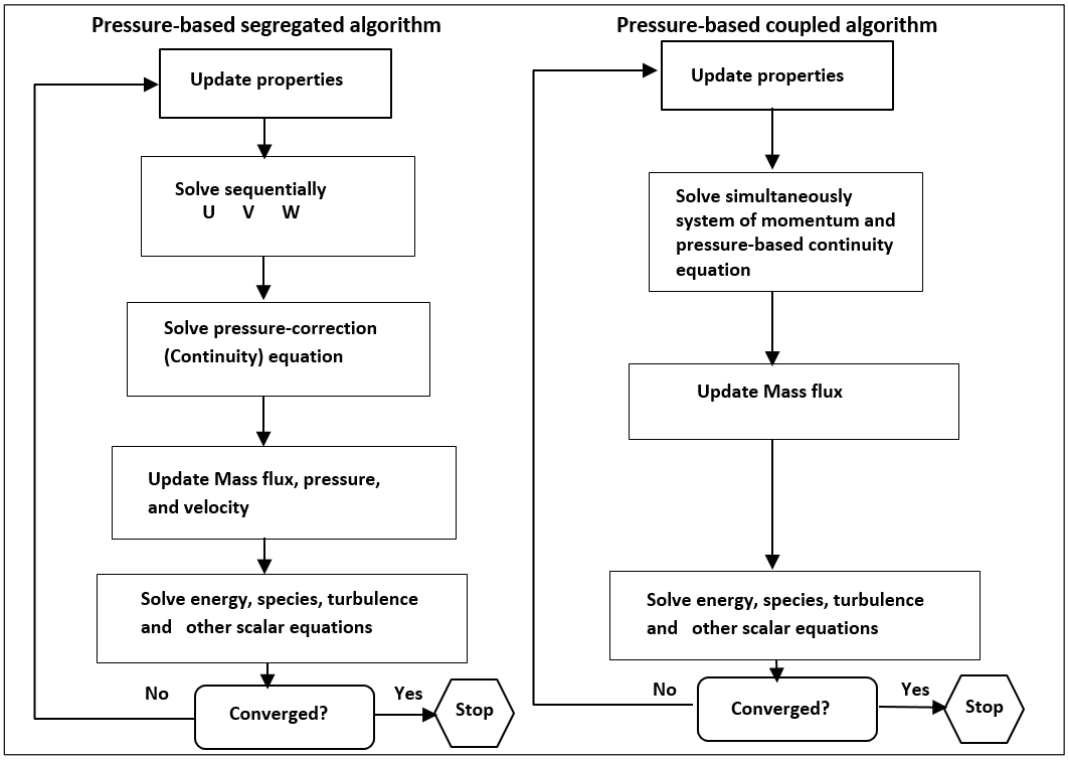

Figure 5.2 Flowchart of two pressure-based solver algorithms [Fluent Inc., (2013-2014)]

Numerical Simulation

5.5. Physical Modeling

Different geometries of the shroud design for CFD modeling were analyzed using ANSYS-FLUENT 14 and ANSYS-FLUENT 15. The models were created in SOLIDWORKS 13 based on the airfoils E423 (Eppler E423 high lift airfoil) database with changing the angle of attack. Six models in full scale were analyzed in 2D simulation of the axisymmetric shroud body expressed in polar coordinates. The experimental model analyzed in 2D was a scale down of full optimum model size keeping an area ratio of 2. In addition, CFD analysis included simulation in 3D for drag force investigations.

Six full scale models with proposed throat radius of 168 inches were modeled in solidworks. These models, shown in **Figures (5.3 and 5.4),** were simulated in ANSYS-FLUENT to investigate the effects of changing the length and angle of attack on the aerodynamic performances of the shroud E423. In addition, these models were designed to determine the available amount of the extracted power of each model. **Table 5.1** shows clearly the configurations of the shroud models. Model M1 was selected as optimum reference model based on augmentation velocity factor, power performance, and cost efficiency. It was tested in the experimental work at a scaled down model named (M7_EX). As compared to model M1, the models M5 and M6 were changed in the length but with throat radius and angle of attack kept constant to give area ratios of 3, and 4, respectively. Models M2, M3, and M4 had different angles of attack, keeping the throat radius and length constant resulting in area ratios of 1.75, 2.5, and 3 respectively. **Appendix B** shows databases and geometries for all models.

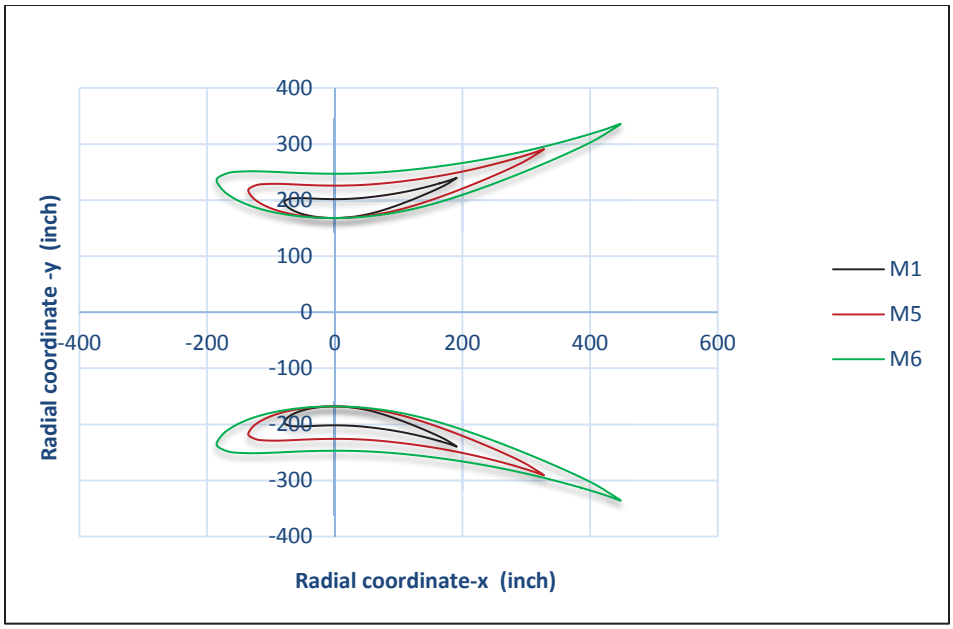

Figure 5.3 Shroud models M1, M5, and M6 showing change in the shroud length with the angle of attack and throat radius constant)

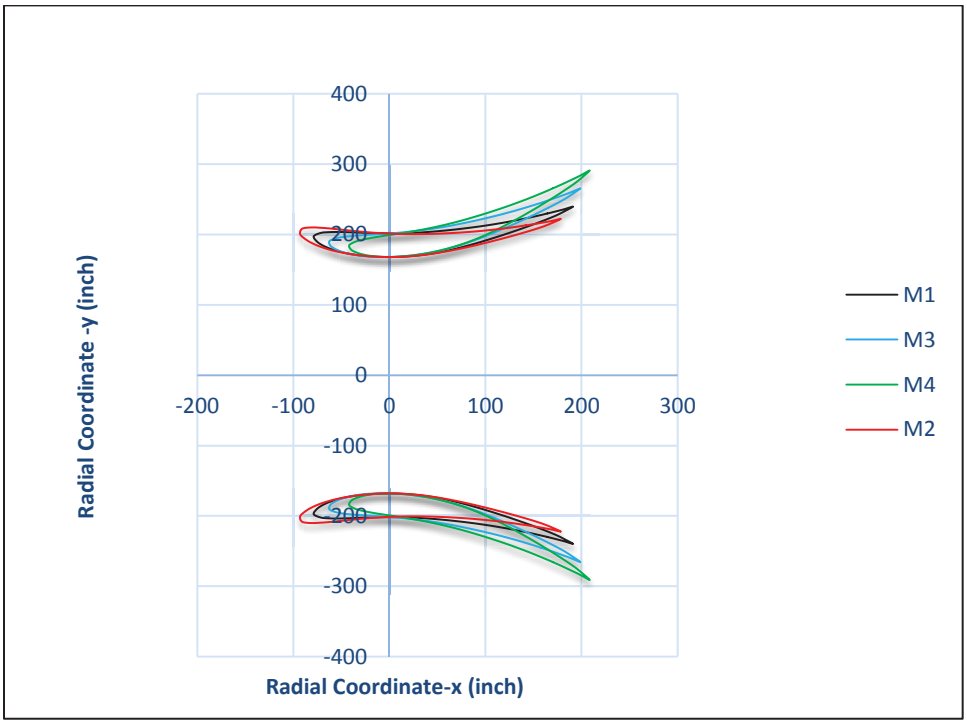

Figure 5.4 Shroud models M1, M2, M3, and M4 showing change in the angle of attack with the length and throat radius constant

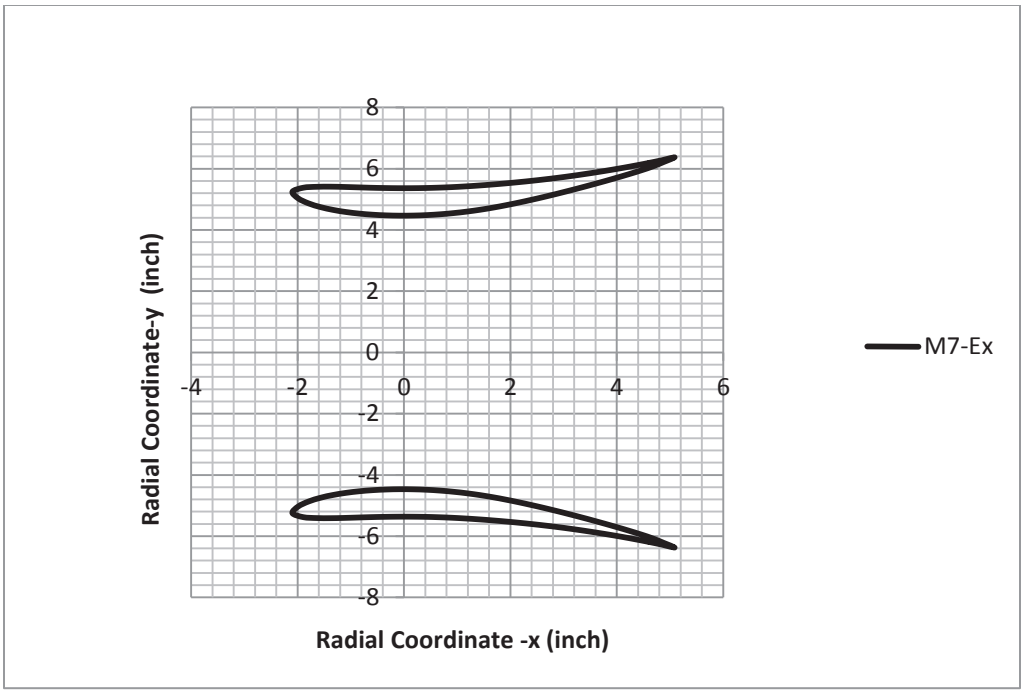

Figure 5.5 Experimental shroud model M7-Ex scaled down of M1

Table 5.1 Configurations of the six models and experiment model

Model Type	Description	Angle of attack α	Area Ratio β	Length Ratio L/R_{th}
M1	Optimum Model	8.96	2	1.6
M2	α : Reduced R_{th}&L :constant	3.96	1.75	1.6
M3	α : increased R_{th}&L :constant	16.52	2.5	1.6
M4	α : increased R_{th}&L :constant	23.2	3	1.6
M5	L : increased R_{th}&α :constant	8.96	3	2.75
M6	L : increased R_{th}&α :constant	8.96	4	3.77
M7_EX	Experimental model: scale down of M1	8.96	2	1.6

5.6. Geometry of Computational Domain

5.6.A. 2-D Geometry of Computational Domain

Since the shroud E423 geometry was axisymmetric, the 2D simulation was performed on only half of the empty shroud for each of seven models. To avoid any blockage effect, save the analysis time, and achieve converged solution, the rectangular computational domain was sized to $(\mathbf{75}\ \boldsymbol{xR_{throat}})$ long and $(\mathbf{29}\ \boldsymbol{xR_{throat}})$ high for the full-scale size models, as shown in **Figure 5.6.** For the micro-experimental model, the computational domain was $(\mathbf{90}\ \boldsymbol{xR_{throat}})$ long and $(\mathbf{33}\ \boldsymbol{xR_{throat}})$ high.

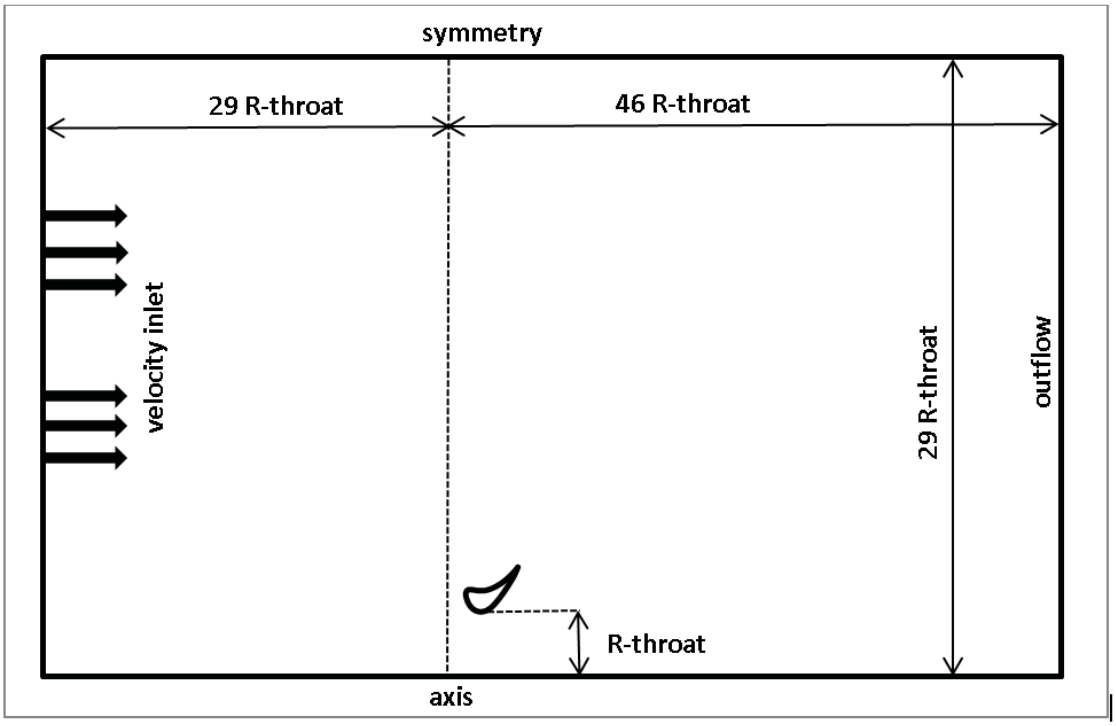

Figure 5.6 Computational domain and boundary conditions

5.6.B. 3-D Geometry of Computational Domain

The goal of 3D analysis in ANSYS-FLUENT 15 was to analyze the drag force effect on the empty shroud for each model. The domain was taken as cylindrical symmetry, only a portion of 60°, with radius $(\mathbf{23}\ \boldsymbol{xR_{throat}})$ and length$(\mathbf{60}\ \boldsymbol{xR_{throat}})$, as shown in **Figure 5.7.**

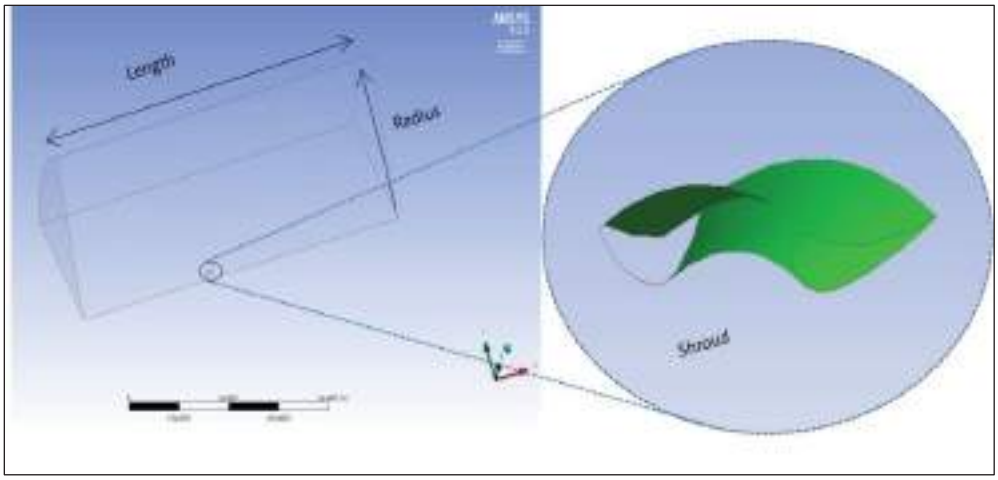

Figure 5.7 3D Fluid domain in ANSYS-FLUENT15 for a portion (60°) of empty shroud model

5.7 Mesh and Boundary Conditions

Ansys-Workbench was used to create the model's domain and mesh in this analysis. For the 2D simulation, each model was discretized into approximately 140,000 triangle elements using unstructured mesh. It was difficult to generate structured mesh in workbench around the shroud geometry analyzed with an axisymmetric domain since the airfoils have sharp edge, and a curvature shape. However, 5 layers of structured quadrilateral mesh were created around the shroud surface to avoid the flow separation. Adjacent to a very fine triangular mesh was created and extended in both x and y-

directions the boundary layer mesh, out from the shroud. Beyond these two regions, larger triangular meshes were utilized. All three regions are illustrated in **Figure 5.8**

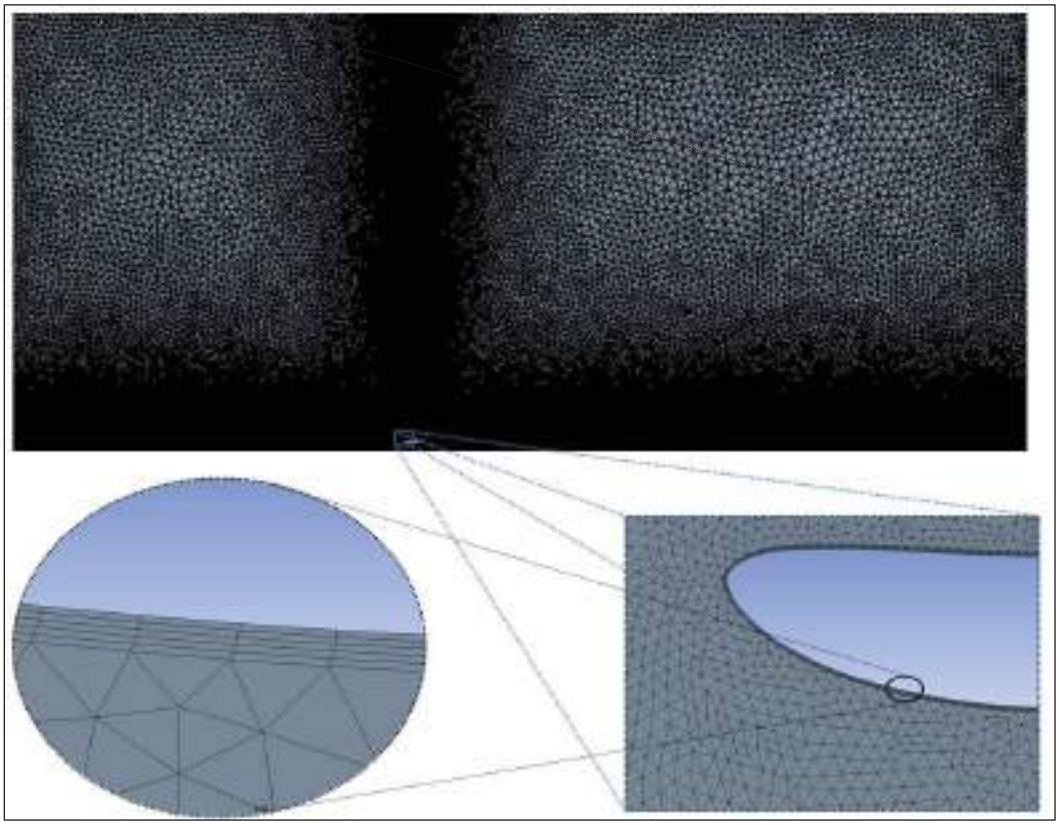

Figure 5.8 Unstructured triangle mesh with showing layers around the shroud

The relevant center of mesh shape was selected fine with high smoothing. The minimum mesh size was varied from 0.5 inches to 1 inch depending on the model configuration, while the maximum mesh size reached to 200 inches. These sizes were for full size model. For the micro-experimental model, 0.03 inches was the minimum and 11.79 inches the maximum mesh sizes.

The mesh in the 3D modeling was also created in Workbench of ANSYS-FlUENT15, for a portion of 60° of the shroud model**.** Unstructured meshes of 2,558,323

triangle elements were used. Again 5 layers were added to the surface of the shroud to avoid the separation layers, as shown in **Figure 5.9**.

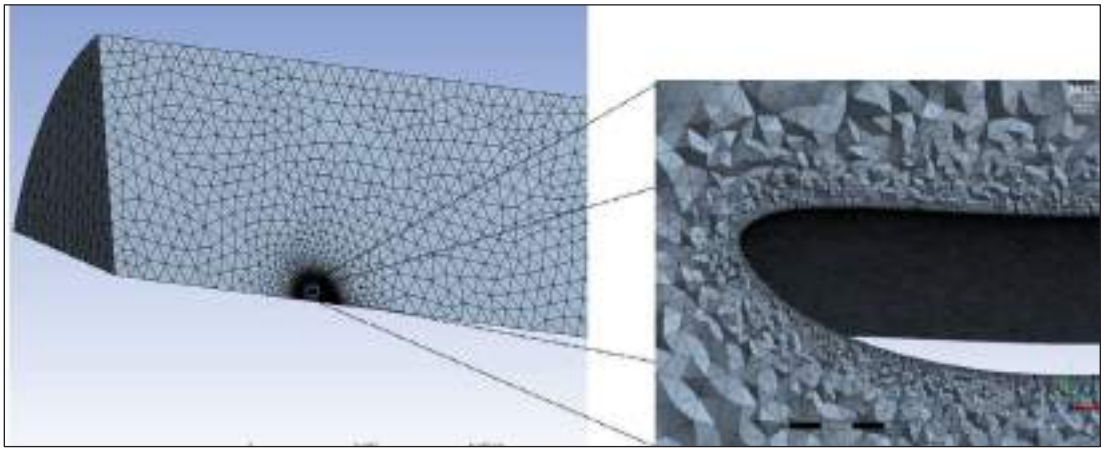

Figure 5.9 Three-dimensional meshes for a portion (60°) of the empty shroud

5.8 Solver Control and Turbulence Model

Numerical simulation of 2D models was carried out using Fluent 14 &15. The fluid flow was considered as steady state flow in order to simplify the CFD simulations for the wind tunnel experiments. As mentioned previously, pressure-based solver was chosen since the flow over the shroud was assumed incompressible under very small Mach number. Since the shroud is symmetric, the axisymmetric analysis was taken to lower the number of iterations, and therefore time, to reach a converged solution.

The standard $\mathbf{K-\varepsilon}$ turbulence model was utilized in 2-dimensional analysis since it is widely used in 2D simulation. The turbulent coefficient model was left as a default, as shown in **Figure 5.10 (a).** The inlet boundary condition was a constant free stream velocity of 5 m/s for full size models and the outlet boundary of the domain was set to zero atmospheric pressure (operating pressure 101,325 Pa) as shown in **Figure 5.11**. The

inlet velocity for experimental model was 8.98 m/s which was the same velocity used in wind tunnel. The turbulent intensity was set to 5% since it was assumed as a free-stream, low velocity operation. The turbulent viscosity ratio kept as a default 10%, as shown in **Figure 5.11**.

Simple scheme of pressure –velocity coupling was selected even though it takes little more time than couple scheme to reach convergence; it is more accurate for steady state flow. Other setups of solution methods were showed in **Figure 5.10 (b).**The residual convergence criteria were chosen 10^{-6} which gave convergent solution with around 1200 iterations as shown in **Figure 5.10 (c).**

(a) (b) (c)

Figure 5.10 Solution method settings (a) Turbulance model setup (b) Solution methods setup (c) Residual Monitors setup

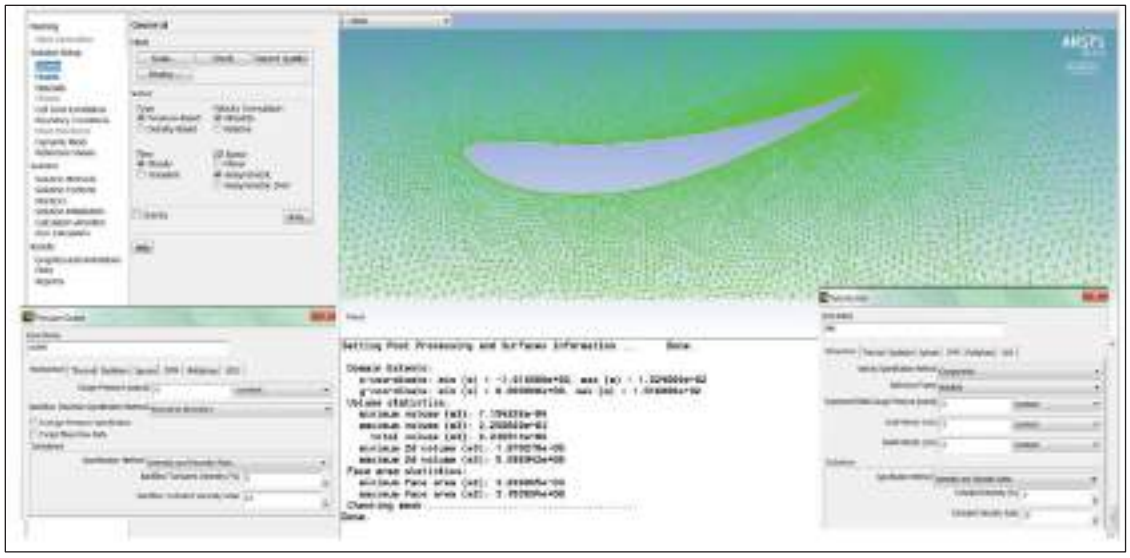

Figure 5.11 Illustrate general physics setup, and the boundary conditions monitors

The SST **K − ω** (Shear Stress Transport) turbulence model was used in the 3-dimensional analysis. Since the necessary number of mesh elements was enormous, the SST **K − ω** turbulence model is appropriate for this analysis to save the time and reach the convergent solution. Other physics setups of 3D simulation were kept the same as in the 2D simulation.

5.9 Scaling (similitude)

The wind tunnel used in the experiment of this study was small with dimensions of (16x4x4) feet. As mentioned previously in **Chapter 4**, the wind tunnel was not large enough to test the full size model of exit diameter 39.95 feet. In order to match the augmentation velocity factor and other results between the experimental model and full size model M2, it was required to scale the velocity and the geometry. The experimental model M7 used in this investigation was 1.06 feet in exit diameter and 0.598 feet in the length.

In order to make a similitude between the experiment model and the prototype, it was necessary for the the Reynolds number to be the same for both of them (Hibbeler, 2015).

$$\left(\frac{\rho V D}{\mu}\right)_m = \left(\frac{\rho V D}{\mu}\right)_p \tag{5.10}$$

Where: ρ: air density, μ : air viscosity , V: velocity , D: diameter , m: model, p: prototype .The same fluid was used for both the model and the prototype. Therefore, its properties ρ and μ will be the same, then:

$$V_m D_m = V_p D_p \tag{5.11}$$

Chapter 6
THE RESULTS AND DISCUSSION

The goal of this study was to optimize the shroud design which has an outlet area larger than its throat area, as discussed in **Chapter 5**. The main focus of this research was more on the augmentation factor and radial air velocity distribution in the shroud throat area, in addition to other factors. Since the amount of wind energy of air passing the rotor area is proportional to its mass flow rate**,** it was practical to place the wind turbine in the throat area of the shroud because this is the highest velocity augmentation location, by a factor of more than two.

CFD Analysis Results

The CFD (Computational Fluid Dynamics) was carried out using the ANSYS-FLUENT 14 &15 software and the computational settings were as discussed in **Chapter5**. Those settings led to a convergent solution with a number of iterations variant between 1000-2100, for each of six models and the scaled down experimental model, as shown in **Figure 6.1**

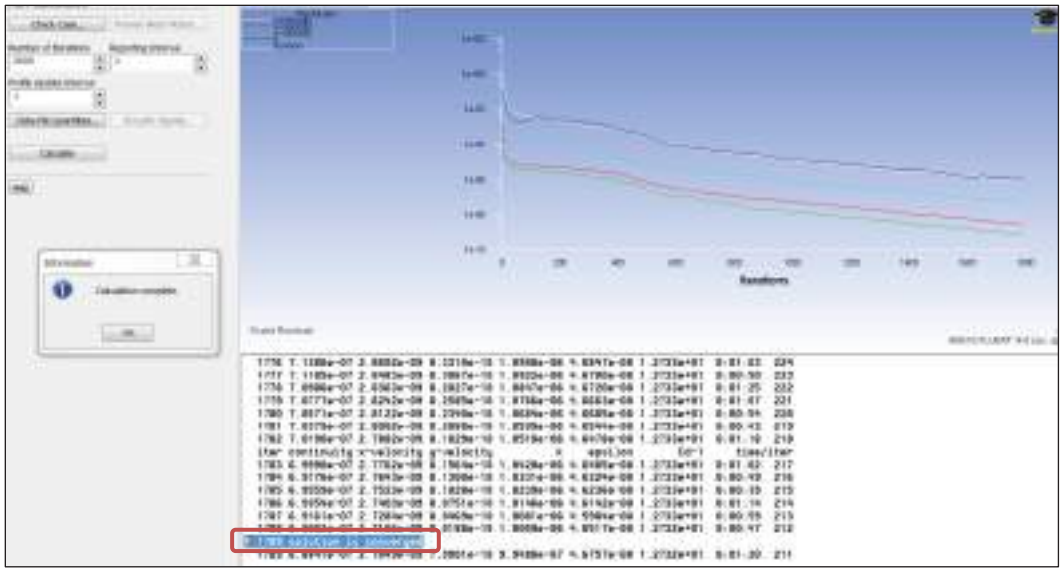

Figure 6.1 Solution calculations show the convergence at 1789 iterations of residual criteria 10^{-6}

6.1 Augmentation Factor AF0 and Radial Velocity Distribution inside the Shroud Throat Area

The improvement of the shroud's augmentation capabilities was sought in this study. As result of CFD analysis on the six different models of empty shroud E423, it was found that the wind speed is doubled inside the shroud particularly in throat area, as shown in **Figure 6.2,** and **Figure A.7** of Appendix C.

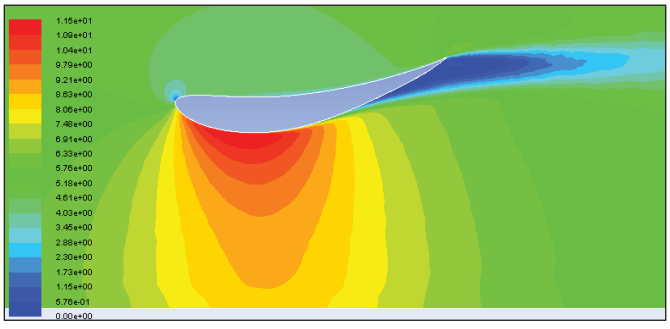

Figure 6.2 Velocity contour of the axisymmetric empty shroud E423 of M1 (AR=2) (Inlet velocity 5 m/s).

The augmentation velocity factor (AF0) is the first factor affecting the increase in power output and the method of comparison used by SAWT (Shrouded Augmented Wind Turbine) to determine whether the system is worth developing. In other words, the augmentation factor describes the SAWT efficiency. Igra (1981), and Widnall (2009), referred to the augmentation velocity factor (AF0), as the ratio of the average wind velocity in the throat area of the shroud to the undisturbed wind velocity ($V_{ave.\ at\ throat}/V_{0.}$).

Table 6.1 shows the augmentation velocity factors (AF0) for each model. A higher AF0 indicates a higher mass flow rate through the shroud throat area, thus increasing the extracted power.

Table 6.1 Augmentation velocity factors for empty shroud E423 models

Model	**AF0**	**Model**	**AF0**
M1	1.9	M4	1.742
M2	1.82	M5	2.11
M3	1.785	M6	2.16

There is significant increase in AF0 in models M5 and M6 since these models were increased in length and area ratio, as shown in **Table 5.1** in Chapter 5. However, model M4, which has area ratio of 3, was much lower than M1 (optimum model) even though it has higher area ratio. This was caused by the higher separation layers, leading to lower mass flow rates in the throat area of models M3 and M4. Also, the entrance section of both models M3 and M4 were reduced (because of high angle of attack) compared to M1. The large curvature section enhanced the inlet section (entrance) of the shroud model M1, and served as a nozzle, as discussed in **Chapter 2**, **Section 2.9**. In the

model M3 and M4, it can be seen that increasing the area ratio without increasing the shroud length appropriately, caused high separation layers and then led to reduce AF0.

Figure 6.3 shows radial velocity distribution in the shroud throat area. The maximum velocity (V_{max} =12.0633 m/s) for an inlet velocity of 5 m/s. For the non-dimensional velocity, V_{max} occurred in model M5 at a radius ratio of 0.97, while maximum radius (R_{max}) is 4.2164 m for all models. Model M5 and M6 have higher air velocity since they have highest area ratio and longest length. The model M1 (AR=2), in the bold line, also has good air velocity distribution compared with other models. In the all models, a remarkable increase in wind speed can be obtained, achieving a high average velocity in the throat plane that is 1.82 – 2.16 times greater than that of the approaching wind velocity V_0.

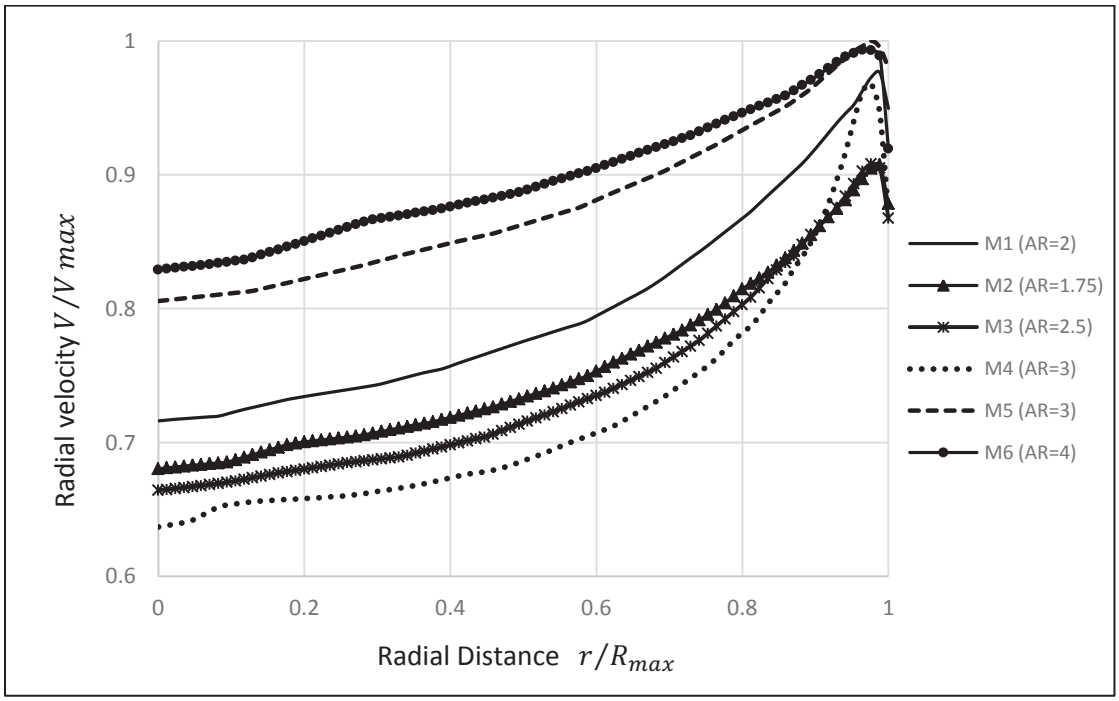

Figure 6.3 Non-dimensional, radial velocity distribution in the throat section of the shrouds (Empty Shrouds)

6.2. Back-Pressure Ratio γ and Radial Velocity Distribution at the Exit Plane of the Shroud

The CFD analysis on the six models revealed an improvement in the pressure recovery. It was discussed previously in **Chapter 2** and three that the pressure drops when entering the shroud and continues to drop causing increase in the velocity, while trying to return to the static pressure once passing the exit plane. The pressure recovery or back pressure was described as ratio of velocities in Van Bussel equation for extracted power (reference **Equation 3.16, Chapter 3**). It is the ratio of the average velocity in the exit plane of the shroud to the undisturbed wind velocity ($\gamma = V_{exit}/V_0$). According to the **Equation 3.16,** in **Chapter 2,** the power increases with increasing γ.

Table 6.2 shows the back pressure ratios for the six models. A significant increase of the back pressure ratio γ was observed in the model M1 (optimum model) and M2 compared to the other models. The effect of extending the shroud length (in model M5 & M6), and increasing the angle of attack (in model M3 & M4), resulted in a lower back pressure ratio γ.

Table 6.2 Back pressure ratios for the six models of the empty shroud E423

Model	Back-Pressure γ
M1	**1.1353**
M2	**1.1996**
M3	**1.0011**
M4	**0.9077**
M5	**1.0001**
M6	**0.8682**

Figure 6.4 shows the non-dimensional air velocity distribution in the exit section of the shroud models. A significant lower sub-atmospheric pressure has surrounded the outlet of the shroud. There is low pressure region at trail edge of the shroud caused by flow separation from the shroud surface as referred in **Figure 6.4**. The higher area ratio of the models provides a greater base pressure effect, and then produces higher separation flow at the exit area. The maximum velocity (V_{max} = 6.706 m/s) occurred in model M1 at $r = .99$ m while R_{max} is 8.5344 m.

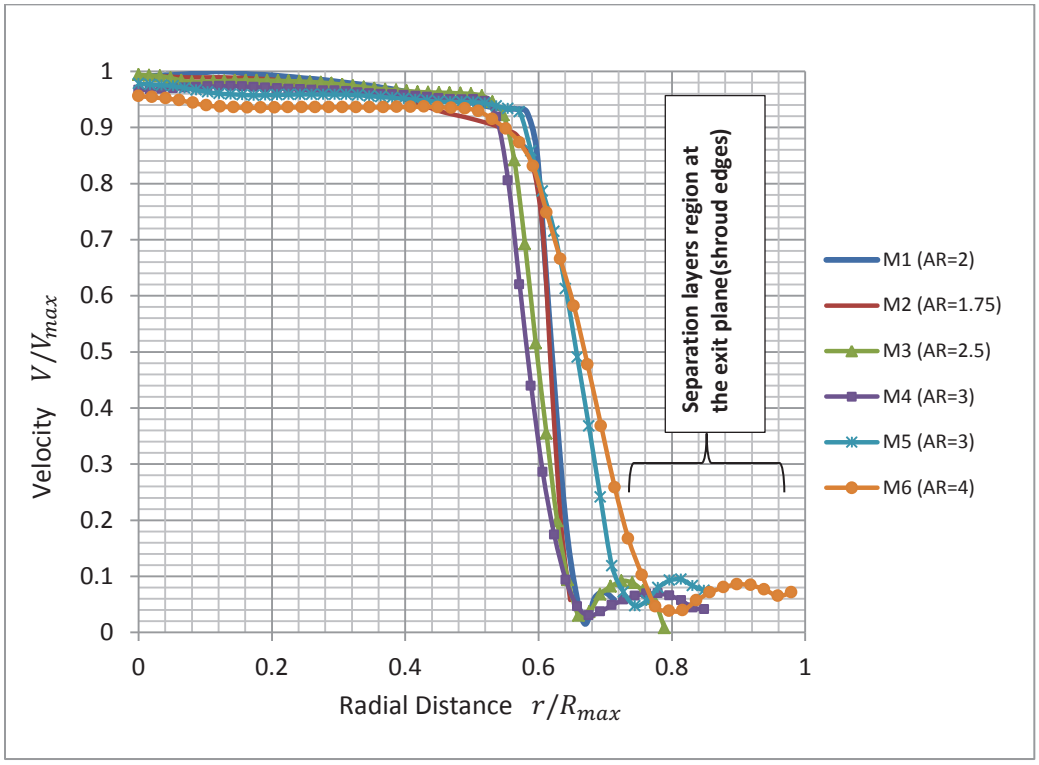

Figure 6.4 Non-dimensional, radial velocity distribution in the exit plane of the shrouds (Empty Shrouds)

6.3 Pressure Distribution Along and Inside the Empty Shroud

Figure 6.5 shows the pressure distribution inside the empty shroud models, along *x*- coordinate in two different radial positions. In position 1, which is radially at the R_{max} of the throat area, the pressure drops pointedly at the throat area and then it tries to recover at exit area (at the trailing edge of the shroud) where the separation layers start. In position 2, which is at the centerline (r = 0), the pressure is a little higher; this means the velocity at the center is less than that at the edge of shroud as showed previously in **Figures 6.2** and **6.3.** The minimum static pressure is ($p_{\min}$ =– 76.2 Pa), which occurred in model M5 at axial distance -0.12 as shown in **Figure 6.5,** where x_{max} is the shroud cord length in positive direction. The radial plane of the throat section was aligned with origin.

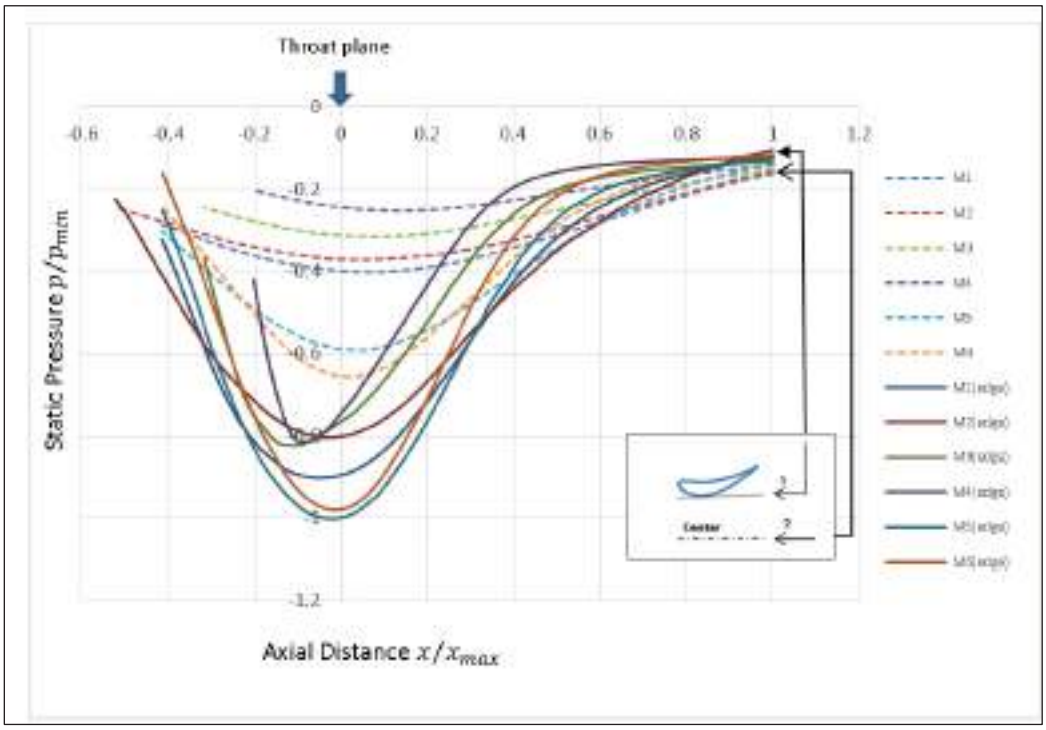

Figure 6.5 Non-dimensional axial pressure distributions along and inside the empty shroud E423 models in two different positions.

Figure 6.6 illustrates the static pressure distribution over the entire empty shroud surface for each model. The pressure drop in the throat area of the shroud (as shown at the readings -0.8 and -1) indicates the velocity is at maximum. It can be seen clearly that at approximately 80% of airfoil cord length the flow starts to separate which is indicated by an increase in the static pressure. In outer surface of the shroud, the static pressure is higher at stagnation point of the leading edge (as shown at 0.2). In general, the pressure over the outer surface is greater which causes the lift force that is directed toward the center of the shroud. The static pressure distribution can be explained well with help of **Figure 6.7** and **Figure A.8** of Appendix C.

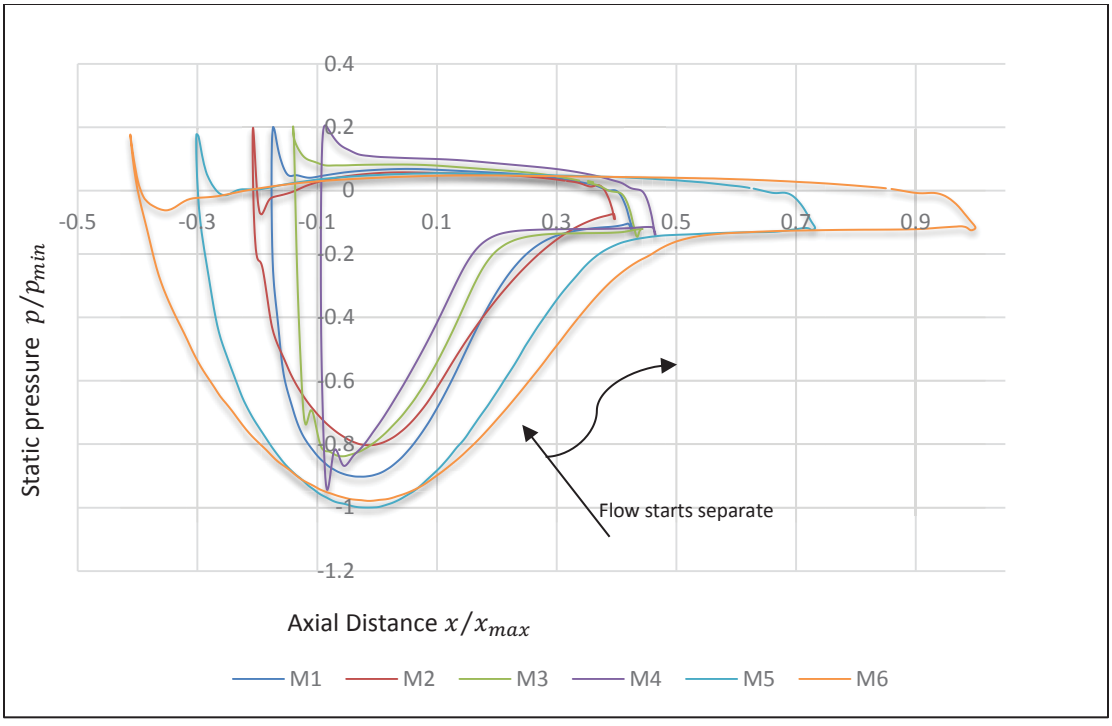

Figure 6.6 Non-dimensional static pressure distribution over entire empty shroud E423 models' surface.

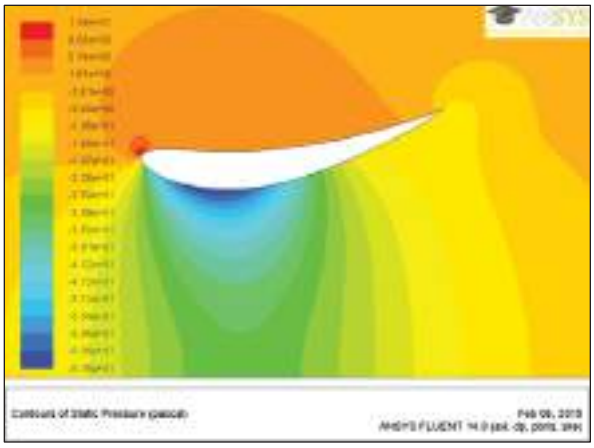

Figure 6.7 Static pressure contour of the empty shroud model M1

6.4 Drag Force Analysis

The drag force effect on the empty shroud models was analyzed computationally in 2D simulation and confirmed with 3D simulation. **Table 6.3** shows the drag force coefficient (C_d) and configurations for each model. The drag force coefficient was calculated using **Equation 3.40,** from **Chapter 3,** with the drag force obtained from CFD analysis. As discussed previously in **Chapter 2**, the drag force acts normally on the projected frontal annular area.

Table 6.3 Geometry configurations of empty shroud for the six models and drag coefficients

Model	Area ratio	Angle of attack α	L/R_{th}	C_d
M1	2	8.96	1.6	0.3417
M2	1.75	3.96	1.6	0.2319
M3	2.5	16.52	1.6	0.5588
M4	3	23.2	1.6	0.6
M5	3	8.96	2.75	0.5394
M6	4	8.96	3.769	0.5908

Figure 6.8 shows the drag coefficient that increases with increasing the angle of attack. Since the drag force is a combination of both the pressure drag and friction drag, the pressure drag acting on the frontal area will maximize once this area became bigger. As a result of increasing the angle of attack, the frontal area exposed to airflow will become larger. Model M4, that has angle of attack $\alpha = 23.2°$ showed drag coefficient of 0.6, while model M2, that has α=3.96°, showed drag coefficient of 0.2319. Indeed, the drag coefficient of model M1 (optimum model) was close to that of model M2, which was the minimum.

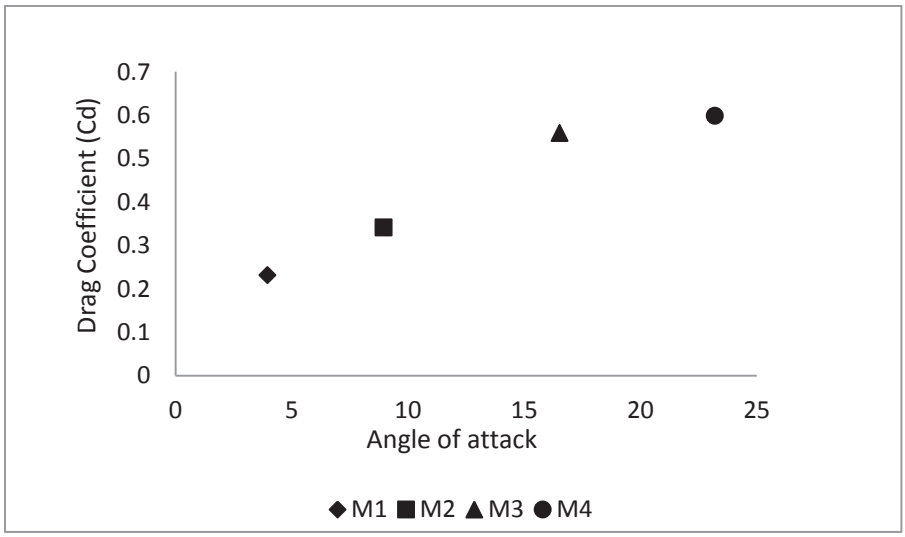

Figure 6.8 Comparison of the empty shroud drag coefficient against angle of attack

Figure 6.9 shows the drag coefficient corresponding to shroud model area ratio. As mentioned previously, increasing the frontal area causes enormous drag force on the shroud and since the difference between the throat area and exit area (represented by frontal area) increased, the drag coefficient maximized. In **Figure 6.9**, it is noticed that there is a difference in drag coefficient between model M4 and M5 even though they

have the same area ratio. The reason is that model M4 has a higher-pressure drag because it has a higher angle of attack. In contrast, the pressure drag is lower on the surface of model M5 which has lower angle of attack. Comparing between these models' sizes, the pressure drag is much more influential than friction drag.

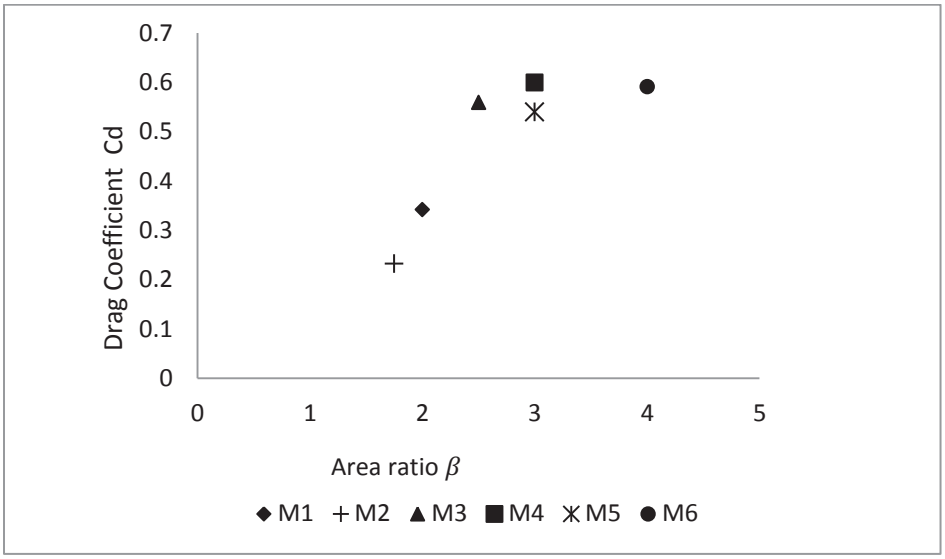

Figure 6.9 Drag coefficient of empty shroud against area ratio**,** for the six Models

The interrelationship between the drag coefficient and length ratio is described in **Figure 6.10**. The drag coefficient also increased with extending the shroud length and also area ratio because the friction drag on the surface has been increased. Model M6 that has the greatest length ratio (L/R_{th}=3.769), has larger drag coefficient of 0.59, compared to model M1.

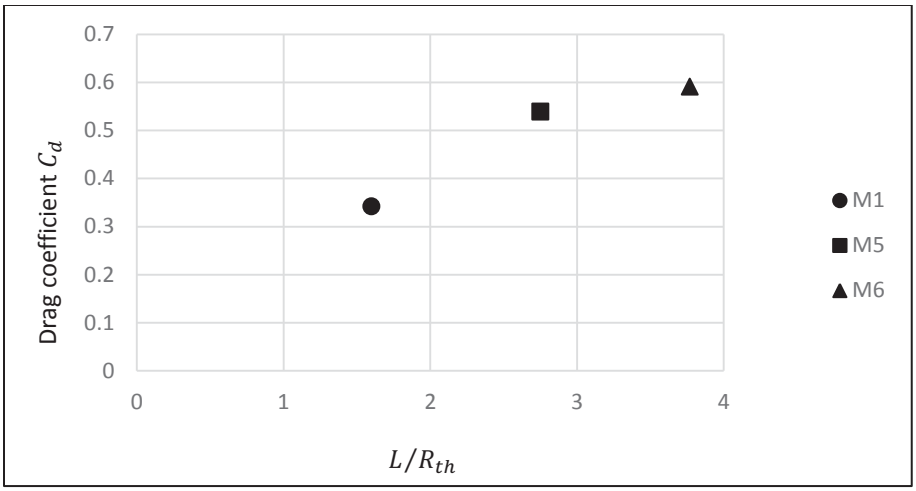

Figure 6.10 The shroud length ratio versus drag coefficient of the M1, M5, and M6

6.5 Grid Convergence

The numerical results for all of augmentation velocity factor AF0, back pressure ratio γ, and drag force were validated with changing the mesh size. The grid convergence simulations were conducted in order to determine an appropriate grid size that balanced accuracy with practicality. The mesh would become finer as the volumes of the elements (cells) become smaller, and thus the error in the discrete results would be reduced. However this increases the computer processing time, sometimes prohibitively. Actually, three different grid types were taken for each of six models; this information is available in Appendix D.

The comparison was done based on analysis time and solution convergence, and also the percentage of errors of Grid1 and Grid2 with respect to Grid3. The Grid2 showed a decrease in the computer processing time and at the same time, the solution reached the convergence with acceptable number of iterations. However, the Grid1 and Grid 3 generally showed an increase in analysis time and required a greater number of iterations

to reach the convergent solution, which led to an increase in the processing time, reference, **Table A.4,** and **Appendix D.** Thus, the characteristics of Grid2 were used for all of the final models, as shown in **Table 6.5**.

Table 6.4 The final numerical analysis of Grid2 for the six models, and percentage different with Grid3

		M1	M2	M3	M4	M5	M6
Results	AF0	1.9 (1.058%)	1.82 (1.105%)	1.78 (0.56%)	1.742 (0.114%)	2.11 (0.95%)	2.16 (0.46%)
	γ	1.16 (1.318%)	1.199 (0.803%)	1.03 (0.966%)	0.9077 (1.34%)	1 (1.005%)	0.868 (0.23%)
	C_d	0.35 (2.05%)	0.23 (%7.115)	0.5588 (0.392%)	0.6 (0.4988%)	0.539 (2.06%)	0.5908 (0.152%)

Table 6.5 Geometry and Grid information for convergence of Grid2

Grid2				
Models	# of Nodes	# of Elements	Run Time (min)	# of Iterations
M1	58432	113698	14.28	1472
M2	52757	101704	9.1	1423
M3	51624	100100	17	1083
M4	67675	130868	19	2153
M5	71265	139385	20	2008
M6	73863	144603	22	2100

6.6 Mathematical Power Calculations

The PV-curves of the six models and bare wind turbine were obtained from the mathematical modeling using **Equations (3.16 & 3.19),** from **Chapter 3**. The back pressure ratios (γ) in **Equation 3.16** were calculated as result of average air velocity at the exit plane of the shroud to the undisturbed air velocity from CFD analysis as shown in

Table 6.2. The variation of the output power versus the inlet air velocity showed a nonlinear increase between inlet velocities of 5 m/s to 30 m/s, as shown in **Figure 6.11.**

In **Table 6.6,** the maximum output power was achieved in model M6 since it has the highest area ratio of 4. The power of model M6 was approximately 3.5 times compared to bare wind turbine. While the power in model M1 (area ratio of 2) was 2.3 times that of a bare wind turbine. According to PV-curves, it seems clear that the output power increases with increasing shroud area ratio, even though there was a slight effect of back pressure. For instance, the difference in back pressure ratio γ between model M2, that has less separated layers, and the one of model M1 was 0.065. Furthermore, the difference is 0.3 between model M1 and M6, and in this case the difference in back pressure ratio γ did not have a big effect on the output power compared to the area ratio effect. However, the output power performance is dependent upon the shroud efficiency (velocity augmentation factor AF0). The more air mass that was pulled inside the shroud, the much better power output was obtained, as discussed previously in **Chapter Two**.

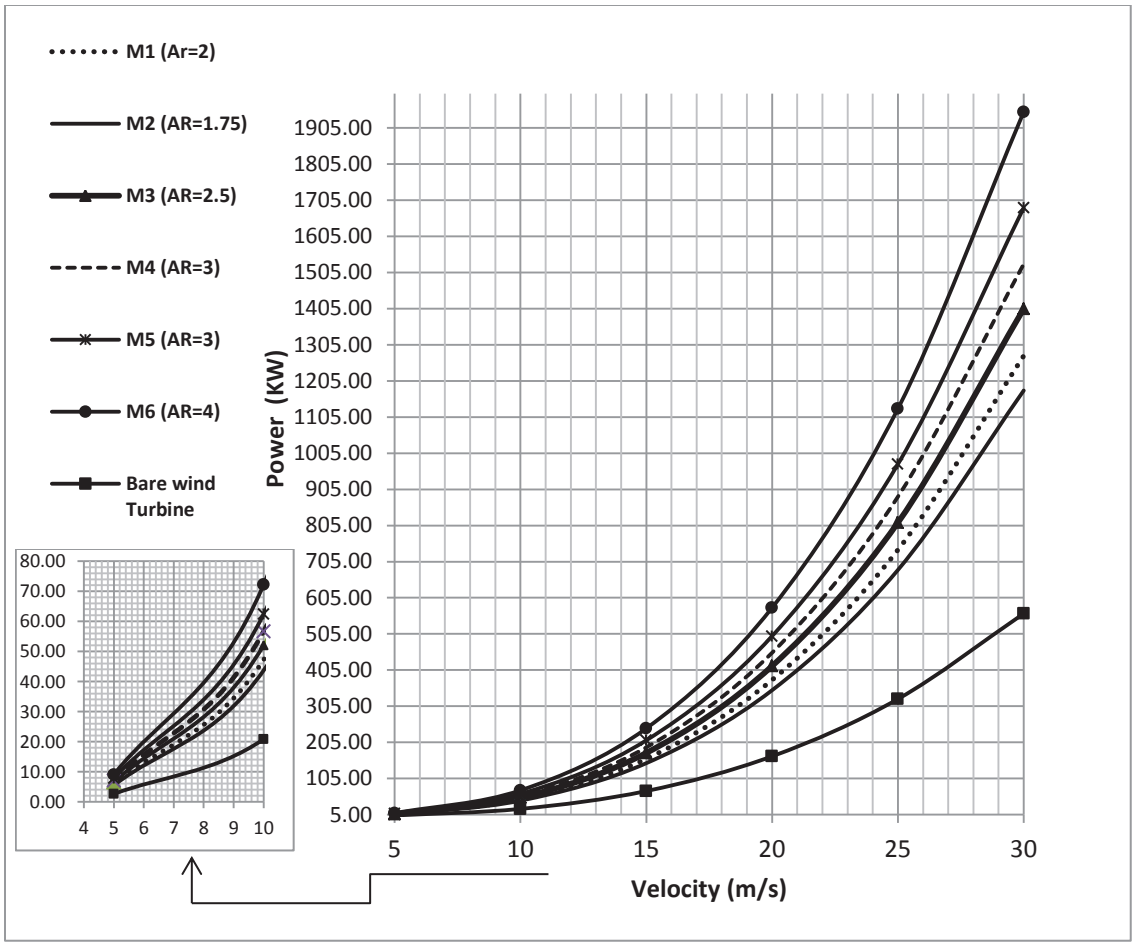

Figure 6.11 Output power versus different inlet air velocities for the six models and bare wind turbine.

Table 6.6 Mathematical calculations of output power of the six models and a bare wind turbine at different inlet air velocities and the ratios for each model with respect to bare wind turbine

Inlet Velocity	Power_M1 (KW) (ratio=2.27)	Power_M2 (KW) (ratio=2.1)	Power_M3 (KW) (ratio=2.5)	Power_M4 (KW) (ratio=3)	Power_M5 (KW) (ratio=3)	Power_M6 (KW) (ratio=3.47)	Bare Wind Turbine
5	5.90	5.46	6.50	7.08	7.80	9.03	2.60
10	47.21	43.65	52.04	56.62	62.38	72.20	20.79
15	159.33	147.31	175.62	191.08	210.53	243.69	70.17
20	377.67	349.18	416.29	452.94	499.05	577.64	166.33
25	737.64	681.99	813.06	884.65	974.70	1128.20	324.87
30	1274.64	1178.49	1404.97	1528.67	1684.28	1949.53	561.37

The induction factor (a) in **Equation 3.16** was considered as optimum factor of 1/3 for the power calculations in **Table 6.4** to give an optimum power coefficient with Betz limit of 16/27. Also, **Figure 6.12** shows power coefficients C_p with various induction factors. It is clear that all models are higher than Betz limit of a bare wind turbine. Model M6 has the maximum power coefficient since it has the highest area ratio.

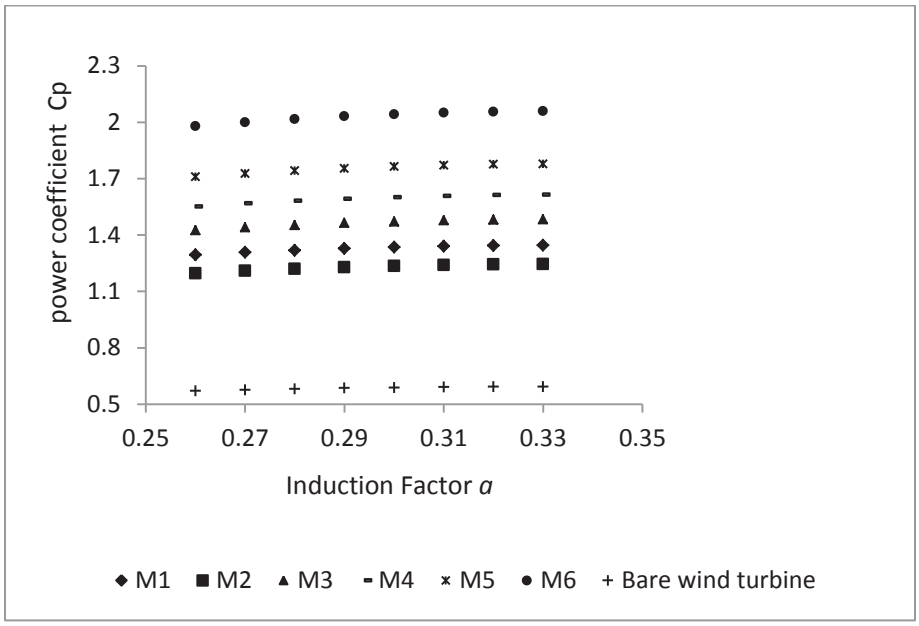

Figure 6.12 Power coefficients of six models versus different induction factors a

6.7 Results Validation (Experimental Work)

In order to validate the CFD simulation results, two experiments were conducted with shroud E423 as discussed in **Chapter 4.** The experimental work was performed for both empty micro-shroud of area ratio equal to 2, and with placing a small generator in its throat area. The properties in both wind tunnel and CFD analysis were assumed the same.

6.7.1 Experimental Velocity Distribution in Throat Area of the Empty Shroud E423 (Augmented Velocity Validation)

Figure 6.13 shows experimental results of the velocity distribution at the throat area of the micro empty shroud placed inside the test section of the wind tunnel. The bold line represents the velocity distribution at 5 inches just before the shroud inlet section. The marked line represents the augmented velocity at throat section of the shroud model M7_EX. The outside readings were taken in radial distance of 8 inches to cover large area, while the radial distance inside the throat area of shroud was 4.33 inches. The maximum velocity (V_{max} =16.48 m/s) occurred at the radius 4.33 inches inside the shroud throat section. The maximum radius R_{max} was considered in **Figure 6.13** the maximum radial distance of 8 inches, which was taken outside the shroud, and at the section plane just 5 inches away from the inlet section of the shroud.

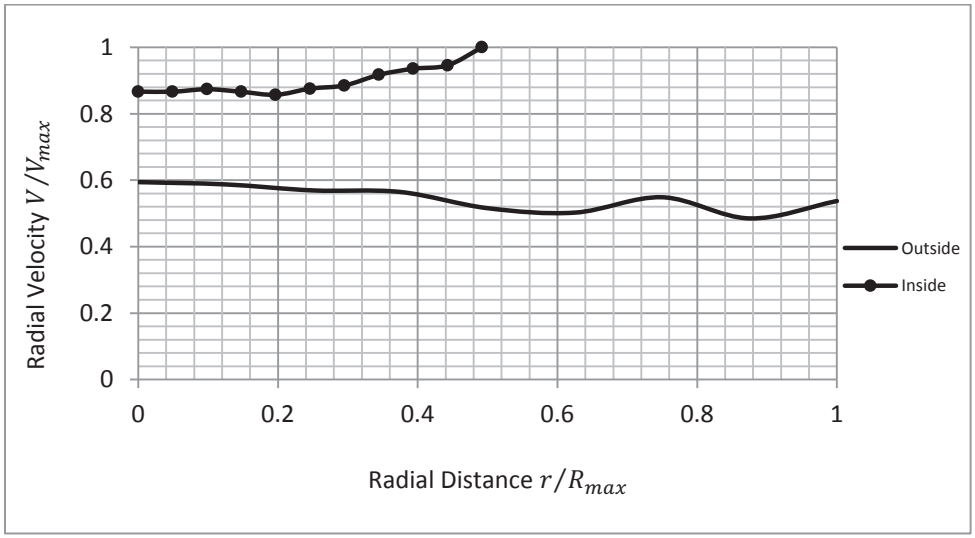

Figure 6.13 Experimental results of non-dimensional air velocity distribution in radial distance inside and outside the experimental model M7_EX (at throat area and outside the shroud)

In this investigation**,** good agreement was found between numerical and experimental results with an error of about 1.06%, which validated the numerical model. **Figure 6.14** shows the numerical against experimental results represented in non-dimensional**.** The maximum velocity (V_{max} =17.612 m/s) occurred in CFD modeling at radius 0.108 m where maximum radius is 0.111 m (4.33 inches), and the inlet velocity was 8.98 m/s. In addition, **Table 6.7** shows the comparison of the augmentation factor between the numerical and experimental work.

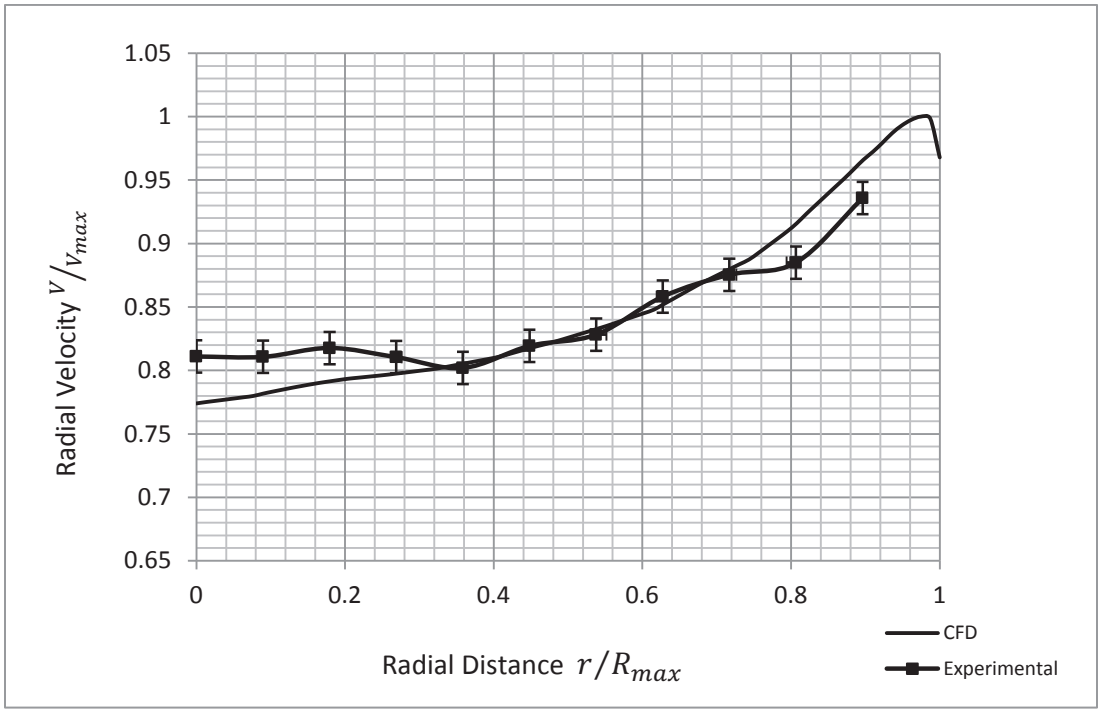

Figure 6.14 validation of the simulation, (Numerical Vs Experimental non-dimensional results results) (Error bars indicate two velocity readings)

Table 6.7 CFD Vs experimental work results of the augmentation factor

	CFD	Experimental Test
V_{inlet}	8.98 m/s	8.98 m/s
$V_{average\ at\ throat}$	14.97 m/s	14.81 m/s
Augmentation Factor AF0	1.667	1.65

As mentioned previously, the inlet velocity for the CFD comparison was the same as the one used in the wind tunnel velocity (8.98 m/s). Then, the full size of the model M1 was scaled down to be the same experimental model. The scaled shroud model M7_EX, with $V_0 = 8.98$ m/s produced augmentation factors of 1.66 in CFD analysis and 1.65 in experimental work.

In case of full-scale shroud size, throat radius was assumed 168 inches, and the augmentation factor of Model M1 was 1.9. In order to get the same value of the augmentation factor for model M7_EX, the inlet velocity has to be scaled up as discussed previously in **section 5.9** , **Chapter 5**. This analysis was approved with using **Equation 5.13**. The velocity for full scale was assumed 5 m/s, then by applying **Equation 5.13** the velocity became 187 m/s, which approximately gave augmentation factor 1.89 for experimental model M7_EX in CFD simulation, as shown **Figure 6.15**.

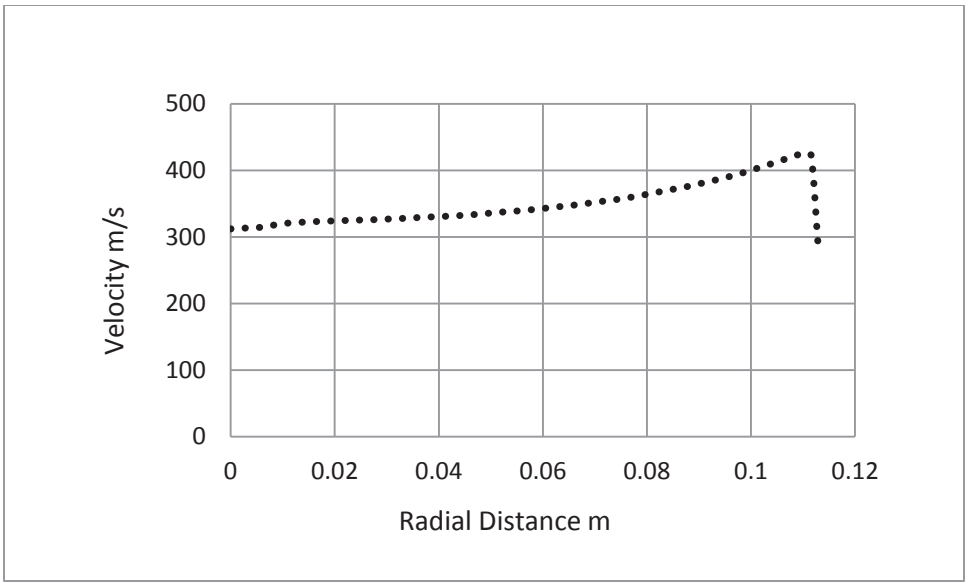

Figure 6.15 Plot of the velocity at the throat area of the shroud against the radial position for experimental model M7_EX at inlet velocity 187 m/s

6.7.2 Experimental Measurements of the Extracted Power Using Micro-Shroud Wind Turbine (Power Validation)

Since the appropriate tools for 3D simulation of entire shrouded wind turbine's system were not available, power was validated by experimental work only. **Table 6.8** shows the experimental results of the power measurements for both the shrouded wind turbine and the bare wind turbine. Different multi-meters were used in this experiment which allowed measurements of the voltages and the currents by taking the mean values between the maximum and minimum readings. A remarkable increase in the output power in SAWT was observed, approximately 1.6 -2.2 times that of a bare wind turbine.

Table 6.8 Experimental measurements of the extracted power for both bare wind turbine and shrouded wind turbine.

Bare wind Turbine (Non- shrouded)				Shrouded Wind Turbine(SAWT)			
mean velocity	Voltage volts	Current mAmper	Power (w)	Voltage (volts)	Current mAmper	Power (w)	Ratio
9.32	18.2	12.6	0.231	21.35	24.8	0.531	2.3
9.81	19.45	16.25	0.318	22.95	29.7	0.683	2.14
10.19	20.75	21.05	0.4988	23.9	36.3	0.868	1.98
10.58	21.95	29.45	0.73644	25.2	44	1.109	1.71
11	24.1	30.1	0.8109	27.3	50.15	1.373	1.88

Also, **Figure 6.16** shows clearly the difference between two cases. The mean velocity was the average velocities that were taken just 5 inches in front of the test section.

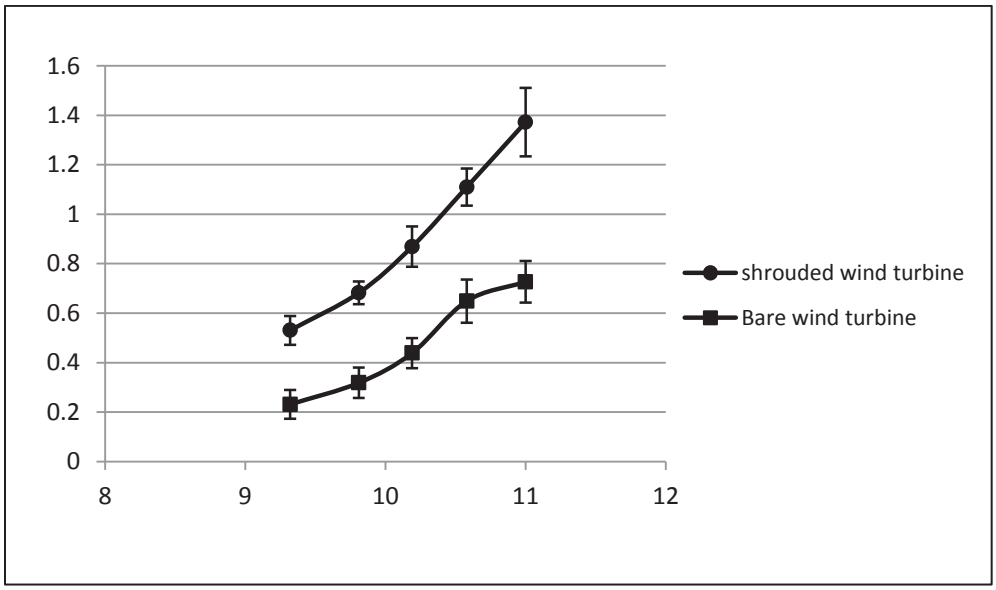

Figure 6.16. Experimental comparison between shrouded wind turbine and bare wind turbine for extracted power (Error bars indicate two power readings)

Since the optimum power coefficient C_p for the bare wind turbine is 0.59 (at a =1/3) for a very large scale, it is not practical to consider this value for micro wind turbine (it has to be so small). It was difficult to compare the mathematical results for the power with the experimental result of the micro-wind turbine for both cases because the test conditions were not the same as the mathematical calculations. There were many factors that influence the turbines' performance including blade profile, which was chosen randomly (not part of research topic), size of the blade diameter, swept area, and the number of the blades used in experiment. Thus, the goal of this experiment was to focus only on the power generated by the bare wind turbine and SAWT in a real world experimental environment.

CHAPTER 7
CONCLUTIONS AND FUTURE WORK

Conclusions

The computational analysis and wind tunnel experiments on special design of shrouded wind turbine had been carried out to achieve a better understanding of the effect of the air distribution at the throat area of empty shroud and consequently the augmented power. Augmentation velocity factor of six different models was sought in this study and the results of CFD analysis showed good performance when the area ratio is increased at appropriate angles of attack. In this study, the shroud E423 of model M1(area ratio of 2) proved to be the acceptable design generating good power with less cost caused by drag force, when compared to other shrouded models studied.

The optimum model (model M1, area ratio of 2) has less augmentation velocity factor (AF0=1.9) and less output power, compared to Model M5 and M6, but Model M1 has significantly less drag force coefficient ($C_d = 0.34$) which reduces the cost effect on the shroud price. In addition, the numerical analysis results on empty models showed a decrease in back pressure ratio in the model M5 ($\gamma = 1$) and M6 ($\gamma = 0.86$). However, the back pressure ratio in model M1 was ($\gamma = 1.135$) which is higher than that in the model M5 and M6. In fact, the reduction in back pressure γ is caused by the flow separation that occurred in the outlet area of the shroud. This flow separation at all of the

model M3, M4, M5, and M6 makes the Kutta condition not completely satisfied compared to model M1 which has been shown that Kutta condition was completely satisfied , reference **Figure 2.6**.

The velocity distribution inside empty shroud E423 obtained from CFD with the proposed model M1 presented excellent agreement with experimental work. In fact the velocity profile matched with the experimental data at the throat area of empty shroud model M1 with error less than 1.06% of the augmentation factor.

The experimental results on micro –wind turbine showed an increase in the output power by approximately 2.2 times with the turbine placed inside the shroud of model M1 (Area ratio of 2), compared to the performance, found in the bare wind turbine. According to the mathematical calculations, the power can be maximized about 3.5- 4 times using model M6 of higher area ratio of 4.

According to the drag force analysis of empty shroud models, the shrouded wind turbine must be designed to survive an extreme wind gusts that are many times greater than normal wind speeds. SAWT (Shrouded Augmented Wind Turbine) requires an enhanced structure and strength foundation, compared to the bare wind turbine that is shroud-less. The model M1, selected to be optimum, has a reasonable drag force coefficient and good output power. Model M6, while having better output power, has much greater drag load on its body. In reality, the high loads caused by drag force will add more cost.

Recommendations and Future Work

There is a recommendation provided for future work that could play good role to enhance the augmented velocity inside the shroud E423 design.

As discussed previously in **Chapter 2**, and in results from **Chapter 6**, the entrance section (inlet) has an influence on the enhancement of the augmentation velocity factor. This section could be more efficient when guide vanes (fixed vanes) are placed just before the rotor plane of the wind turbine. This would help to achieve even better distribution of air flow across the rotor plane of the turbine blades, and thus prevent bending the turbine blade tips in the extreme wind speed.

Many researchers found that the guide vanes improve the mass flow rate for the system. Igra (1981), in his experimental and theoretical research of developing shrouded wind turbines, used stator or guide vanes in his model to provide fairly stable output and high efficiency over a relatively wide range of velocities. Klujszo et al. (1999) designed several guide vanes for air cleaner, and he found that the guide vanes generate swirling motion while increasing turning angle. This swirling motion could be employed or exploited to enhance rotating turbine blades more efficiently.

For future work, it would be useful to design shrouds with the guide vanes at the entrance section (inlet) with various angles. Then, it would be interesting to analyze them computationally and experimentally to look for the best results.

References

Abbott, Ira H. *Theory of Wing Sections/ Including a Summary of Airfoil Data*. New York: Research Engineer, NASA, 1949. Print.

Airfoil Investigation Database. 26 May 2013. Web. 30 Oct. 2014. <http://www.airfoildb.com/foils/list>.

Burton, Tony, David Sharpe, Nick Jenkins, and Ervin Bossanyi. *Wind Energy Handbook*.England. John Wiley &Sons, Ltd, 2001. Print.

Dwyer. "Air Velocity Measurement:How to Take Traverse Readings." *Dwyer Instruments Inc*. Web. 20 Jan. 2015. <http://www.dwyer-inst.com/products/airvelocityintroduction.cfm>.

Engineering design and Technology Series. "*Student's Guide to learnings SolidWorks Software*". SolidWorks corporation. Massachuests.printed.

Forman, K. M. "Preliminary Design and Economic Investigations of Diffuser Augmented Wind Turbines (DAWT)." *Research Department/ Grumman Aerospace Corporation* (May 15 1980). Print.

Foreman, K. M., B. Gilber, and R. A. Oman. "Diffuser Augmentation of Wind Turbines." *Solar Energy*, 20 (1978): 305-11. Print.

Forman, K. M. "Size Effects in DAWT Innovative Wind Energy System Design." *J. Solar Energy Engineering* 105.4 (01 Nov1983): 401-07.Print.

Fluent Inc. "*Release 14.5"*. http://www.arc.vt.edu/ansys_help/flu_th/flu_th_uns_scheme.html. (visited on 1/19/2015)

Fluent Inc. "Pressure-Based Solver." *SAS IP, Inc* (2014).Web.19 Jan. 2015.

Fuel Economy. The official U.S. Government Source for Fuel Economy

Information.15 Oct, 2012.Web. 3 June 2014.

FlowKinetics LLC. *Generic Pitot-Static Pitot Configuration*. Digital image. 2001-2015. Web. 4 Jan. 2015. <http://www.flowkinetics.com/pitot-static-probe-measurement.htm>.

Grassmann, H., F.Bet, M. Ceschia, and M.L. Ganis. “On the Physics of Partially Static Turbines”. *Renewable Energy,* Vol. 29 (2003): 491-499. Print.

Green Energy Technologies. Issue brief. GreenEnergy Technologies, LLC. Web. 10 Oct. 2014. <http://www.getsmartenergy.com/>.

Ganis, Maximilian Ludwig. *National Institute for Nuclear Physics/Department of Physics of Udine*. Hamburg. 2003. Print.

Hansen, Martin O.L. *Aerodynamics of Wind Turbines.* 2nd ed. London: Earthscan, 2008. 27-42. Print.

Hansen, M. O. L, N. N. Sqrensen, and R. G J. Flay. "Effect of Placing a Diffuser around a Wind Turbine." *Wind Energy* 3 (2000): 207-13. Print.

Health Canada. The Government of Canada, 3 April 2014. Web. 25 June 2014.

Hibbeler,R.C. *Fluid Mechanics*. *Pearson Prentice Hall*. NJ. 2015. Print

Igra, Ozer. “Research and Development for Shrouded wind turbines.” *Energy Cmt & Mgmt* ,Vol. 21,pp. 1981: 13-48. Print.

Igra, Ozer. “The Shrouded Aerogenerator.” *Energy Cmt & Mgmt* ,Vol. 2,pp. 1977: 429-439. Print.

Jamieson, P., Garrad Hassan, and Partners. "Beating Betz-Energy Extraction Limits in a Uniform Flow Field." *Conference Paper* (2008). Web. <http://www.gl-garradhassan.com/assets/downloads/Beating_Betz_-

Energy_Extraction_Limits_in_a_Uniform_Flow_Field.pdf>.

Jafari, S.A.H, and B. Kosash. “Flow Analysis of Shrouded Small Wind Turbine with a Simple Frustum Diffuser with Computational Fluid Dynamics Simulations”. *J.Wind Eng. Ind. Aerodyn., Vol.125* (2014):102-110. Print.

Klujszo, L. A. C. , P.K.Songfack, M. Rafaelof, and R. K. Rajamani, “Design of a Stationary Guide Vane Swirl Air Cleaner,” *Minerals Engineering*, vol. 12, no. 11, pp.1375–1392, 1999.

Kutta Conditions. Digital image. *Astropt.org*. 2012. Web. 21 Oct. 2014. <http://www.astropt.org/2012/11/18/a-mecanica-dos-fluidos-no-automobilismo/>.

Kossasih, P.B., N. Bryce, A. Tondelli, and A. Breazley. “Experimental Study of the Performance of Bare and Nozzle-Diffuser Shrouded Micro Wind turbine Under Axial and Non-Axial Inflow Condition.” *Australasian Fluid Mechanics Conference.* Launceston. 7 December 2012.

Kelecy, Franklyn *J.* “Coupling Momentum and Continuity Increases CFD Robustness”. *Applications Specialist, ANSYS, Inc.* Volume II, Issue 2, 2008.

Lilly, G.M., and W.J Rainbird. *A preliminary Report on the Design and Performance of Ducted Windmills.* Rep. no. 102. College Of Aeronautics Cranfield, 1956. Print.

Lubitz, William David, and Shomer, Adam. “ Wind Loads and Efficiency of a Diffuser Augmented Wind Turbine(DAWT).” *CSME international Congress* (4 June 2014). Print.

Lawn, C. J. "Optimization of the Power Output from Ducted Turbines." *J. Power*

and Energy 217 (2003): 107-17. Print.

Mouser Electronics. *MLV Series Low Voltage Pressure Sensors*. Digital image.*DesignNews*.14 Feb. 2011. Web. 5 Jan. 2015. <http://www.designnews.com/document.asp?doc_id=230126&dfpPParams=ind_184,aid_230126&dfpLayout=article>.

National Instruments. “Data Acquisition (DAQ)”.2014. Web. 6 January 2015

NRDC. Renewable Energy for America, 2011. Web. 9 June 2014.

Ohya, Yuji, and Takashi Karasudani. “A Shrouded Wind Turbine Generating High Output Power with Wind-lens Technology”. *Energies*, Vol. 3 (2010): 634-649. Print.

P. Bulat, Mikhail, and Pavel Victorovich Bulat. "Comparison of Turbulence Models in the Calculation of Supersonic Separated Flows." *World Applied Sciences Journal* 27.10 (2013): 1263-266. Print.

Philips, Derek Crant. *An Investigation on Diffuser Augmented Wind Turbine Design*. Diss. The University of Auckland, 2003. New Zealand: ResearchSpace@Auckland, 2003. Print.

PI Research. “Pitot Static Tube.”: 1-4. *Cosworth*. 2014. Web. 4 Jan. 2015. <http://www.cosworth.com/media/198947/29b-071181.pdf>.

Righter, Robert W. *Wind Energy in America*. Norman. The University Of Oklahoma Press.pp. 42-58. 1996. Print.

Rittner, Don. “Windmills of East-America’s first Green Technology” *Timesunion.com*. Hearst Corporation, 18 May 2010. Web. 22 July 2014.

Rienstra, S.W. “ A Note On The Kutta Condition In Glauert’s Solution Of The Thin

Airfoil Problem.” *Journal of Engineering Mathematics*. 26:61-69. 1992.Print.

Rice University. *World Energy Use*. Digital image. *Openstax CNX*. 2006. Web. 12 Sept. 2014. <http://cnx.org/contents/a4b7e0ec-bded-45de-8016-416aaaa8286b@5/World_Energy_Use>.

Spera, Daivd A. *Wind Turbine Technology/ Fundamental Concepts of Wind Turbine Engineering*. 2nd ed. New York: ASME, 2009. Print.

Spera, David A. *Advisory on Shrouded Wind Turbine Project*. Rep. Florida: DASCON Engineering,LLC. 19 June 2014. Print

Spera, David A. *Update WindSphere Shroud CFD Analysis*. Rep. Florida: Dascon Engineering ,LLC., 15 October 2014. Print.

Snel, H. "Reviews of Aerodynamic Investigation and Design Work Underlying the Vortec 1 MW Turbine and Suggestions for Further Optimization." (2001): 1-27. Print.

Shinomiya, Leo Daiki, Déborah Aline, Amanda Maria, Taygoara Felamingo, José Gustavo, André Luiz Amarante, and Jerson Rogério Pinheiro. “ Numerical Study of Flow around Diffusers with Different Geometry Using CFD Applied to Hydrokinetics Turbines Design.” *OBEM International congress of Mechanical Engineering.* 7 November 2013.

Shah, Ishan.M, S. A. Thakkar, K. H Thakkar, and Bhavesh A. Patel. "Performance Analysis on Airfoil Model in Wind Tunnel Testing Machine (WTTM)." *Engineering Research and Applications (IJERA)* 3.4 (2013):

2094-103. Print.

Sveningsson, Andreas. "Analysis of the Performance of Different Turbulence Models in a Stator Vane Passage_Flow." *Department of Thermo and Fluid Dynamics Chalmers University Of Technology* (2003). Print.

SolidWorks. "SOLIDWORKS TUTORIALS." *Dassault Systemes Solidworks*. N.p., 2014. Web. 18 Sept. 2014. <http://www.solidworks.com/sw/resources/solidworks-tutorials.htm>.

Tiukaev, V. N. "Fiberglass Reinforced." *The Great Soviet Encyclopedia*. 1979. Web. 20 Sept. 2014.

Ukhovskii, M.R, and V.I. Iudovich. "Axially Symmetric Flows of Ideal and Viscous Fluids Filling the Whole Space." *Elsevier Ltd.* 32.1 (1968): 59-69. Print.

Van Bussel, Gerard J.W, Dr. "The Science Of Making More Torque From Wind:Diffuser Experiments and Theory Revisited." *Journal of Physics:Conference*75th ser. (2007): 1-12. Print.

Van Bussel, Gerard J.W, Dr. “An Assessment of the Performance of Diffuser Augmented Wind Turbine (DAWT’S). *ASME:* 23 July 1999. Print.

Wind Power in the United States. Map illustrating installed wind generating capacity for U.S. states at end of 2013. Digital image. *Wikipedia*. N.p., 3 June 2014. Web. 25 Sept. 2014. <http://en.wikipedia.org/wiki/Wind_power_in_the_United_States>.

Widnall, Sheila. “Potential Flow Calculation of Axisymmetric Ducted Wind Turbine”. *Massachusetts Institute of Technology*. July,2009.1-19. Print

Wang, Sheng- Huan, and Shih-Hsiug Chen. "Blade Number Effect for a Ducted Wind Turbine." *Mechanical Science and Technology/Spring* 22 (2008): 1984-992. Print.

Yamin, Mat, A.K, Benjamin, S.F, and Roberts C.A. "Pulsating Flow in a Planar Diffuser Upstream of Automotive Catalyst Monoliths." *Int J of Heat and Fluid Flow (benjamin)* 40 (2013): 43-53. Print.

Appendix A

Axial Air Velocity Distribution at Test Wind Tunnel Sections

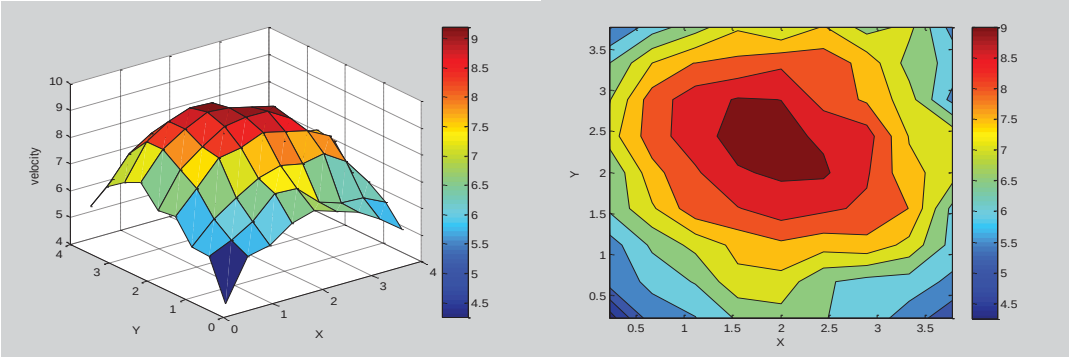

Figure A.1 Air velocity distribution in testing section1 (4 feet from the Fan) (air direction is blowing in reverse direction (backward)).

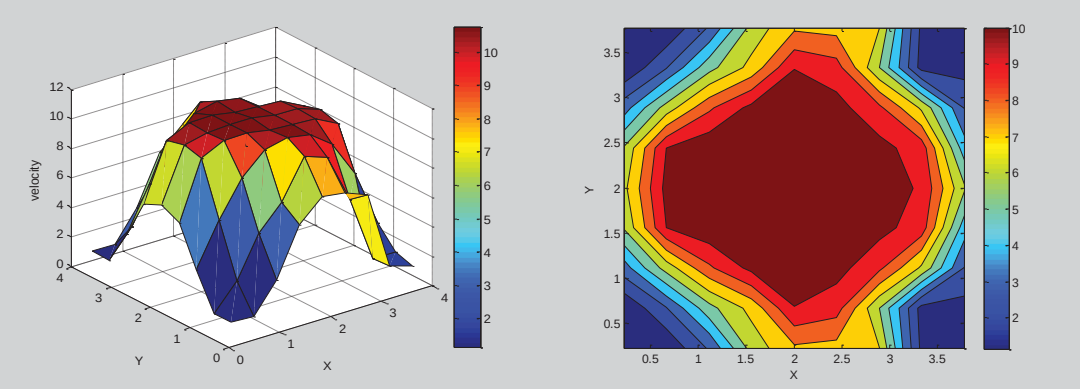

Figure A.2 Air velocity distribution in testing section2 (12 feet from the Fan) (air direction is blowing in reverse direction (backward)).

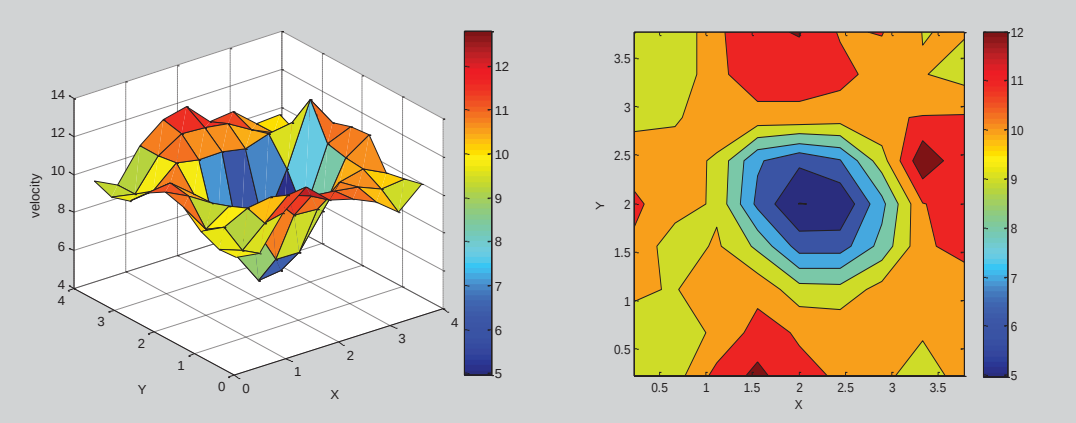

Figure A.3 Air velocity distribution in testing section1 (4 feet from the Fan) (air direction is blowing in forward direction).

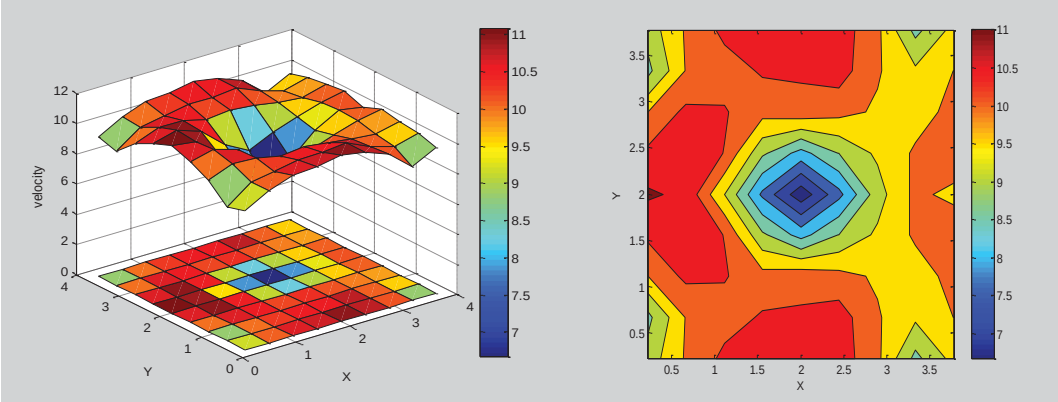

Figure A.4 Air velocity distribution in testing section2 (12 feet from the Fan) (air direction is blowing in forward direction).

Appendix B

Shroud Models' Configurations

Table A.1 Databases of the shroud models' geometries (M1,M2,M3,and M4).

AR=1.75		AR=2		AR=2.5		AR=3	
x	y	x	y	x	y	x	y
142.2258	212.9885	164.4796	229.8384	158.0399	245.154	170.5043	265.7251
133.0169	211.1323	155.3805	226.9368	151.0391	242.0935	163.9246	261.8411
123.7805	209.418	146.2348	224.1851	144	239.122	157.2961	258.0409
114.5188	207.8466	137.0471	221.577	136.9239	236.2399	150.6201	254.3249
105.2328	206.4254	127.8196	219.1137	129.8097	233.4529	143.8948	250.6988
95.92395	205.163	118.5526	216.8032	122.6574	230.7656	137.1196	247.1669
86.59458	204.0623	109.2468	214.6545	115.4678	228.1795	130.2951	243.7311
77.24794	203.1192	99.90462	212.6701	108.2429	225.6938	123.4235	240.3906
67.88757	202.3237	90.52991	210.8453	100.9856	223.3043	116.5081	237.1417
58.51626	201.6694	81.12735	209.1698	93.69881	221.0061	109.5524	233.9799
49.13626	201.1546	71.70029	207.6381	86.38454	218.7971	102.5587	230.9033
39.74944	200.7849	62.25108	206.2495	79.04413	216.6765	95.52827	227.9113
30.35781	200.5706	52.78106	205.0111	71.67797	214.6472	88.46127	225.0068
20.96384	200.5372	43.29105	203.9361	64.28608	212.7139	81.35715	222.1944
11.5715	200.7134	33.78135	203.0541	56.86756	210.8851	74.21396	219.4827
2.186043	201.1132	24.25372	202.3929	49.42042	209.1772	67.02775	216.8874
-7.18717	201.7377	14.71283	201.9641	41.94335	207.6054	59.79538	214.4237
-16.5446	202.5661	5.164357	201.7644	34.43733	206.1782	52.5168	212.1
-25.8842	203.5764	-4.38624	201.7686	26.90476	204.8986	45.19404	209.9196
-35.2047	204.75	-13.935	201.9562	19.34926	203.7619	37.83124	207.8784
-44.5066	206.0629	-23.4793	202.3075	11.77549	202.7541	30.43473	205.9628
-53.8005	207.4323	-33.0181	202.7845	4.186856	201.8652	23.0091	204.1635
-63.1056	208.7214	-42.5561	203.2771	-3.41384	201.0856	15.55829	202.4712
-72.4552	209.624	-52.1012	203.5886	-11.024	200.4051	8.08607	200.8761
-81.8355	210.0569	-61.6503	203.4467	-18.6404	199.7961	0.599156	199.3513
-90.9708	208.141	-71.1135	202.3518	-26.2575	199.1971	-6.88975	197.8363
-92.8953	200.383	-78.856	197.3851	-33.8685	198.5275	-14.3642	196.252
-87.1349	193.0004	-74.7199	189.148	-41.4514	197.5952	-21.7788	194.4103
-79.7684	187.1929	-67.3965	183.0583	-48.9995	196.4091	-29.1283	192.3208
-71.622	182.5266	-59.0047	178.5156	-56.354	194.4014	-36.1864	189.4392
-63.0222	178.7537	-50.1036	175.0667	-62.6374	190.2048	-41.9166	184.5141
-54.1475	175.6792	-40.9195	172.4549	-61.0012	183.4429	-39.4754	177.9995
-45.0869	173.2036	-31.5672	170.5269	-55.1482	178.5564	-33.0749	173.856
-35.8989	171.2514	-22.1126	169.1845	-48.4143	174.9687	-25.9567	171.1082
-26.6226	169.7737	-12.5985	168.3608	-41.2418	172.3469	-18.52	169.3723
-17.2859	168.7442	-3.05501	168.0134	-33.8403	170.4613	-10.9449	168.3948
-7.91096	168.1569	6.494162	168.1273	-26.3125	169.1617	-3.31518	168.0143
1.481247	168.0043	16.02714	168.6953	-18.7172	168.3407	4.323654	168.1171
10.87078	168.2736	25.52379	169.7029	-11.0879	167.9384	11.94558	168.6396
20.23972	168.9527	34.96575	171.1351	-3.44806	167.9043	19.53361	169.5289
29.57118	170.03	44.33619	172.9786	4.186119	168.204	27.07565	170.7489
38.8506	171.4904	53.62015	175.2175	11.80201	168.8121	34.56226	172.2727
48.06664	173.3085	62.80639	177.8287	19.38845	169.7161	41.98389	174.0868
57.21756	175.4311	71.89329	180.7677	26.9346	170.911	49.33038	176.1847

66.3113	177.7872	80.89456	183.9599	34.43006	172.3909	56.59209	178.5595
75.35451	180.3306	89.82314	187.3501	41.86571	174.1468	63.76111	181.2009
84.35139	183.0333	98.68724	190.9059	49.23332	176.1697	70.8303	184.0992
93.30549	185.8748	107.4924	194.605	56.52479	178.4515	77.79265	187.2453
102.2207	188.8361	116.2448	198.4276	63.73312	180.9841	84.64215	190.6304
111.0996	191.9046	124.949	202.3587	70.85212	183.7579	91.37383	194.244
119.9424	195.0754	133.6062	206.3923	77.8778	186.7602	97.98528	198.0732
128.7484	198.3472	142.2159	210.5262	84.81097	189.9705	104.4797	202.0978
137.5142	201.725	150.775	214.7639	91.66203	193.3528	110.8719	206.2831
146.2294	205.2314	159.2721	219.1243	98.44367	196.8723	117.1786	210.5962
154.8719	208.913	167.6807	223.653	105.1647	200.5062	123.4113	215.0155
163.3464	212.9607	175.9082	228.4991	111.8311	204.2395	129.5778	219.527
171.4788	217.6626	183.7044	234.0146	118.447	208.0614	135.6834	224.1204
178.5991	222.31	191.3234	239.7015	125.0171	211.9619	141.734	228.7861
169.6437	219.4818	182.5083	236.1346	131.5453	215.9319	147.7348	233.5158
160.5463	217.1517	173.5292	232.8916	138.0344	219.9654	153.689	238.3039
151.4033	214.9938	164.4796	229.8384	144.4852	224.0601	159.5977	243.148
142.2258	212.9885			150.8977	228.2145	165.4612	248.0467
				157.2709	232.4288	171.2785	253.0003
				163.6012	236.7073	177.0455	258.0123
				169.8792	241.0622	182.7513	263.0939
				176.0866	245.517	188.3749	268.2661
				182.1943	250.1073	193.8832	273.5607
				187.9831	255.0894	199.0276	279.2058
				193.5723	260.2988	203.9465	285.0524
				198.9751	265.6412	208.6641	291.0085
				192.3416	261.9336	202.5272	286.5264
				185.6588	258.2347	196.3403	282.0472
				178.7886	254.8912	189.9244	277.8981
				171.9248	251.5347	183.5165	273.7368
				165.0024	248.3007	177.0356	269.6901
				158.0399	245.154	170.5043	265.7251

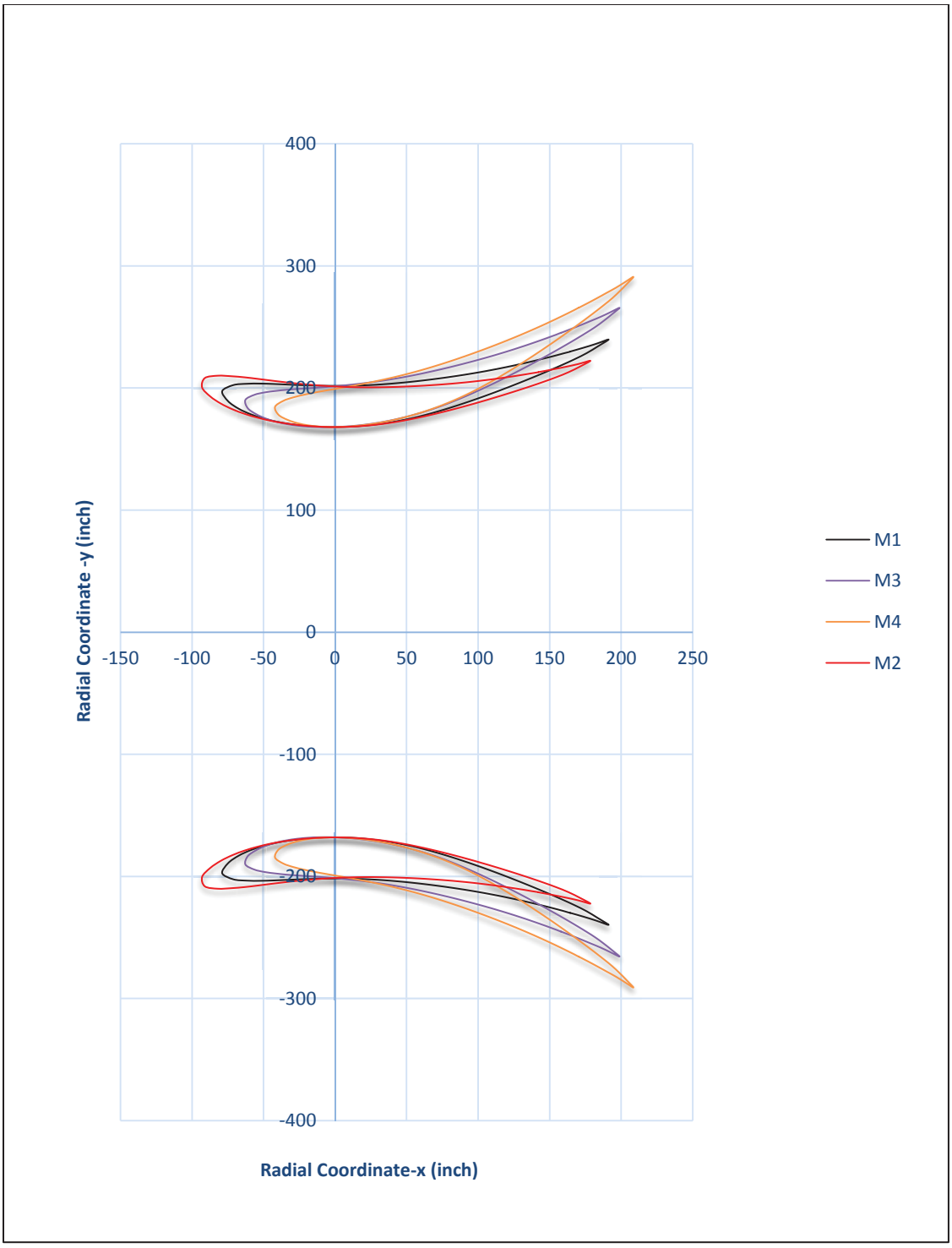

Figure A.5 shroud models (M1, M2, M3, and M4) (changing the angle of attack and keeping the length and throat radius constant)

Table A.2 Databases of the shroud models' geometries (M1, M5, and M6).

AR= 2		AR=3		AR=4		Experimental model	
x	y	x	y	x	y	x	y
164.4796	229.8384	282.0826	274.0528	385.3248	312.8681	4.613537	6.191777
155.3805	226.9368	266.4775	269.0766	364.0083	306.0706	4.372941	6.110603
146.2348	224.1851	250.7927	264.3574	342.5828	299.6242	4.13103	6.03346
137.0471	221.577	235.0358	259.8846	321.0589	293.5144	3.887874	5.9603
127.8196	219.1137	219.2106	255.66	299.4417	287.7435	3.643603	5.890961
118.5526	216.8032	203.3178	251.6975	277.7321	282.3308	3.398275	5.82547
109.2468	214.6545	187.3583	248.0125	255.9314	277.2971	3.151901	5.764043
99.90462	212.6701	171.3364	244.6093	234.0455	272.6483	2.904493	5.706917
90.52991	210.8453	155.2588	241.4797	212.0835	268.3732	2.65612	5.65416
81.12735	209.1698	139.1334	238.6062	190.0562	264.448	2.406878	5.605643
71.70029	207.6381	122.966	235.9793	167.9716	260.8597	2.156893	5.561096
62.25108	206.2495	106.7606	233.5979	145.835	257.6067	1.906256	5.520373
52.78106	205.0111	90.51951	231.4741	123.6497	254.7056	1.65503	5.483455
43.29105	203.9361	74.24416	229.6305	101.4175	252.1873	1.403258	5.450532
33.78135	203.0541	57.93502	228.1178	79.13924	250.1209	1.150958	5.421953
24.25372	202.3929	41.59515	226.9838	56.81897	248.5719	0.898124	5.398502
14.71283	201.9641	25.23251	226.2485	34.4676	247.5674	0.644815	5.380923
5.164357	201.7644	8.856872	225.906	12.09849	247.0995	0.391158	5.369523
-4.38624	201.7686	-7.52241	225.9131	-10.2756	247.1093	0.137301	5.364214
-13.935	201.9562	-23.8986	226.2348	-32.6454	247.5488	-0.1166	5.364324
-23.4793	202.3075	-40.2669	226.8373	-55.0046	248.3718	-0.37047	5.369312
-33.0181	202.7845	-56.626	227.6554	-77.3511	249.4892	-0.62423	5.378652
-42.5561	203.2771	-72.9837	228.5002	-99.6958	250.6432	-0.87784	5.391334
-52.1012	203.5886	-89.3535	229.0344	-122.057	251.373	-1.13142	5.40443
-61.6503	203.4467	-105.73	228.7911	-144.428	251.0406	-1.38519	5.412712
-71.1135	202.3518	-121.96	226.9134	-166.597	248.4757	-1.63907	5.40894
-78.856	197.3851	-135.238	218.3954	-184.735	236.8401	-1.89071	5.379818
-74.7199	189.148	-128.145	204.2688	-175.046	217.5431	-2.0965	5.247794
-67.3965	183.0583	-115.585	193.825	-157.889	203.277	-1.98654	5.028786
-59.0047	178.5156	-101.193	186.0343	-138.23	192.6349	-1.79184	4.866882
-50.1036	175.0667	-85.9276	180.1193	-117.377	184.555	-1.56884	4.746161
-40.9195	172.4549	-70.177	175.6401	-95.8618	178.4364	-1.33208	4.654413
-31.5672	170.5269	-54.1378	172.3336	-73.9522	173.9197	-1.08793	4.58498
-22.1126	169.1845	-37.9232	170.0313	-51.803	170.7748	-0.83926	4.533717
-12.5985	168.3608	-21.6064	168.6188	-29.5144	168.8453	-0.58796	4.498033
-3.05501	168.0134	-5.23934	168.023	-7.15691	168.0315	-0.33503	4.476133
6.494162	168.1273	11.13749	168.2184	15.21385	168.2983	-0.08124	4.466893
16.02714	168.6953	27.48654	169.1924	37.54661	169.6288	0.172657	4.469921
25.52379	169.7029	43.7733	170.9204	59.79433	171.9893	0.42609	4.485018
34.96575	171.1351	59.96626	173.3768	81.91391	175.3447	0.678576	4.511807
44.33619	172.9786	76.03657	176.5384	103.866	179.6634	0.929622	4.549889
53.62015	175.2175	91.95856	180.3779	125.6154	184.9083	1.178724	4.598896
62.80639	177.8287	107.713	184.8563	147.1359	191.0257	1.425521	4.658409
71.89329	180.7677	123.297	189.8967	168.4237	197.9109	1.669776	4.727839
80.89456	183.9599	138.7342	195.3712	189.5109	205.389	1.911397	4.805987
89.82314	187.3501	154.0468	201.1855	210.4279	213.3314	2.150695	4.89085
98.68724	190.9059	169.2486	207.2836	231.1936	221.6614	2.388068	4.980981
107.4924	194.605	184.3495	213.6276	251.8215	230.3274	2.623746	5.075522
116.2448	198.4276	199.3599	220.1832	272.3256	239.2823	2.857855	5.173873

124.949	202.3587	214.2876	226.9251	292.7168	248.4917	3.090549	5.2755
133.6062	206.3923	229.1346	233.8427	312.9978	257.9411	3.321962	5.380014
142.2159	210.5262	243.9002	240.9324	333.1677	267.6256	3.552128	5.487254
150.775	214.7639	258.579	248.2	353.219	277.5532	3.781031	5.597161
159.2721	219.1243	273.1516	255.6782	373.1251	287.7685	4.008587	5.709827
167.6807	223.653	287.5724	263.4448	392.8239	298.3776	4.2345	5.825759
175.9082	228.4991	301.6825	271.756	412.0983	309.7307	4.458054	5.946158
183.7044	234.0146	315.0531	281.2151	430.3626	322.6519	4.676798	6.075005
191.3234	239.7015	328.1196	290.9681	448.2113	335.9744	4.884072	6.221642
182.5083	236.1346	313.0017	284.8508	427.5603	327.6182	5.086617	6.37284
173.5292	232.8916	297.6026	279.2891	406.5251	320.0209	4.852274	6.278003
164.4796	229.8384	282.0826	274.0528	385.3248	312.8681	4.613537	6.191777

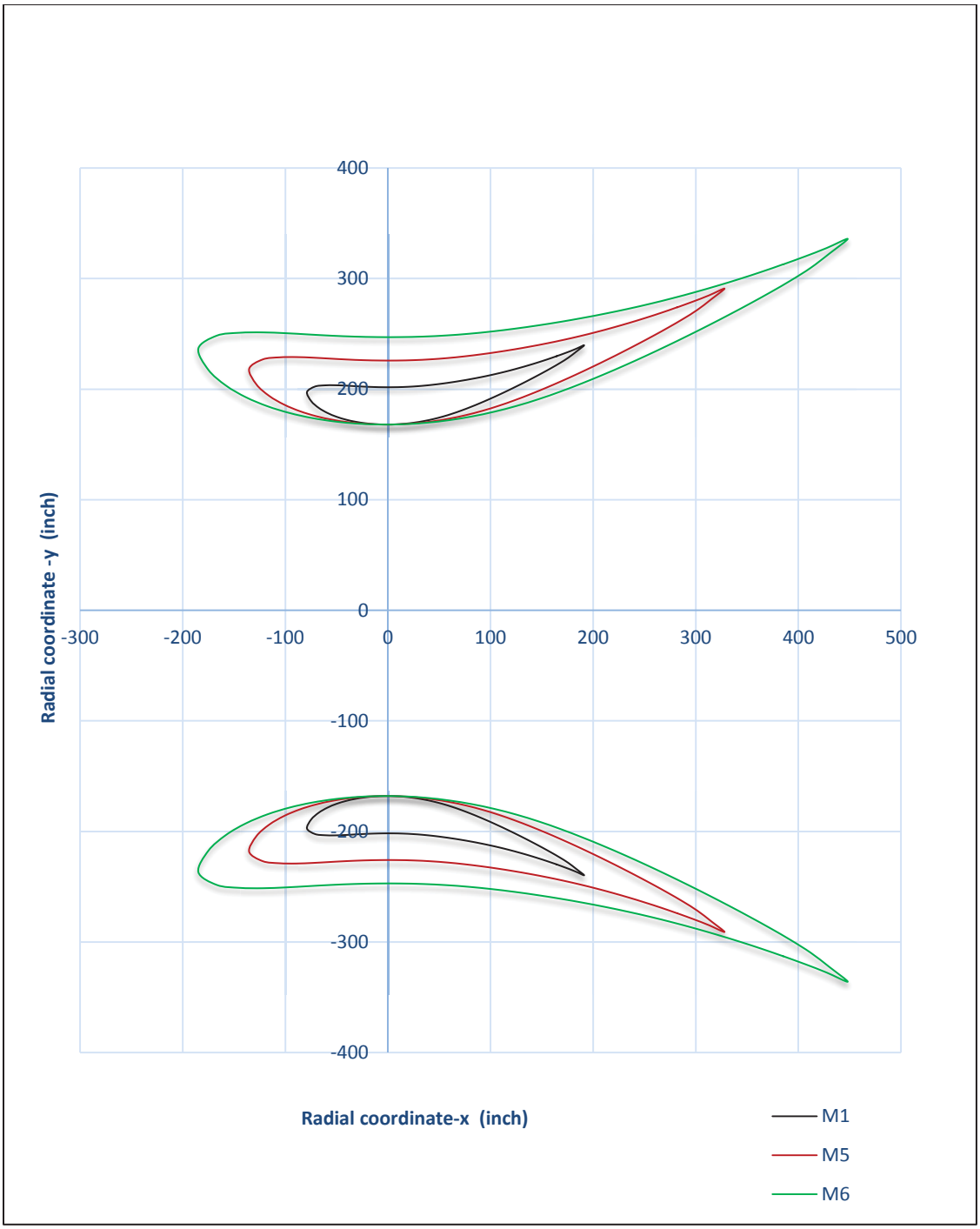

Figure A.6 shroud models (M1, M5, and M6) (changing the shroud length and keeping the angle of attack and throat radius constant)

Appendix C

Results of the velocity and pressure contours for six models

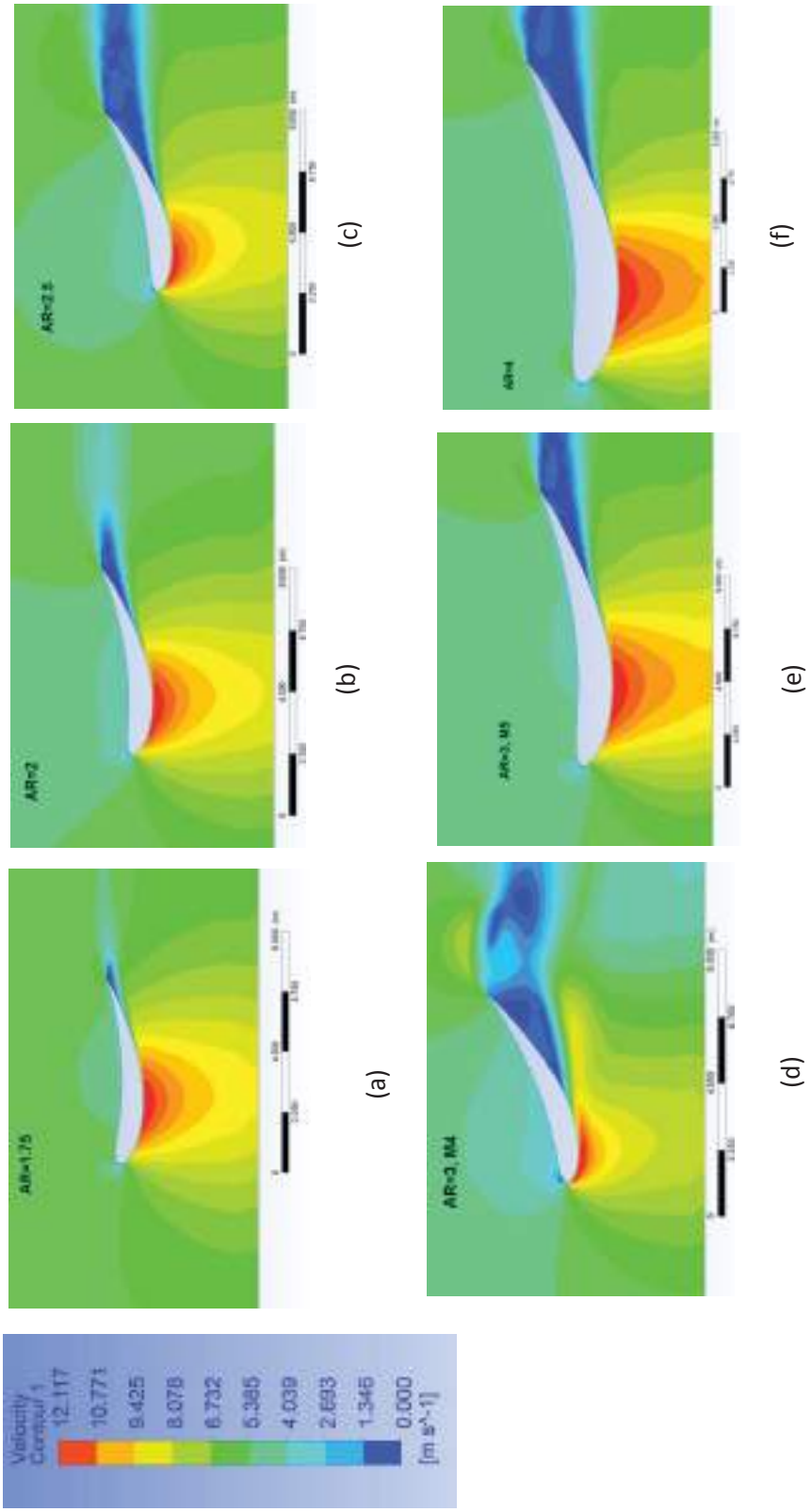

Figure A.7 Velocity contours for the models: (a)M2, Area ratio (AR=1.75), (b) M1,AR=2 , (c) M3,AR=2.5, (d) M4, AR=3, (e) M5, AR=3, (f) M6, AR=4

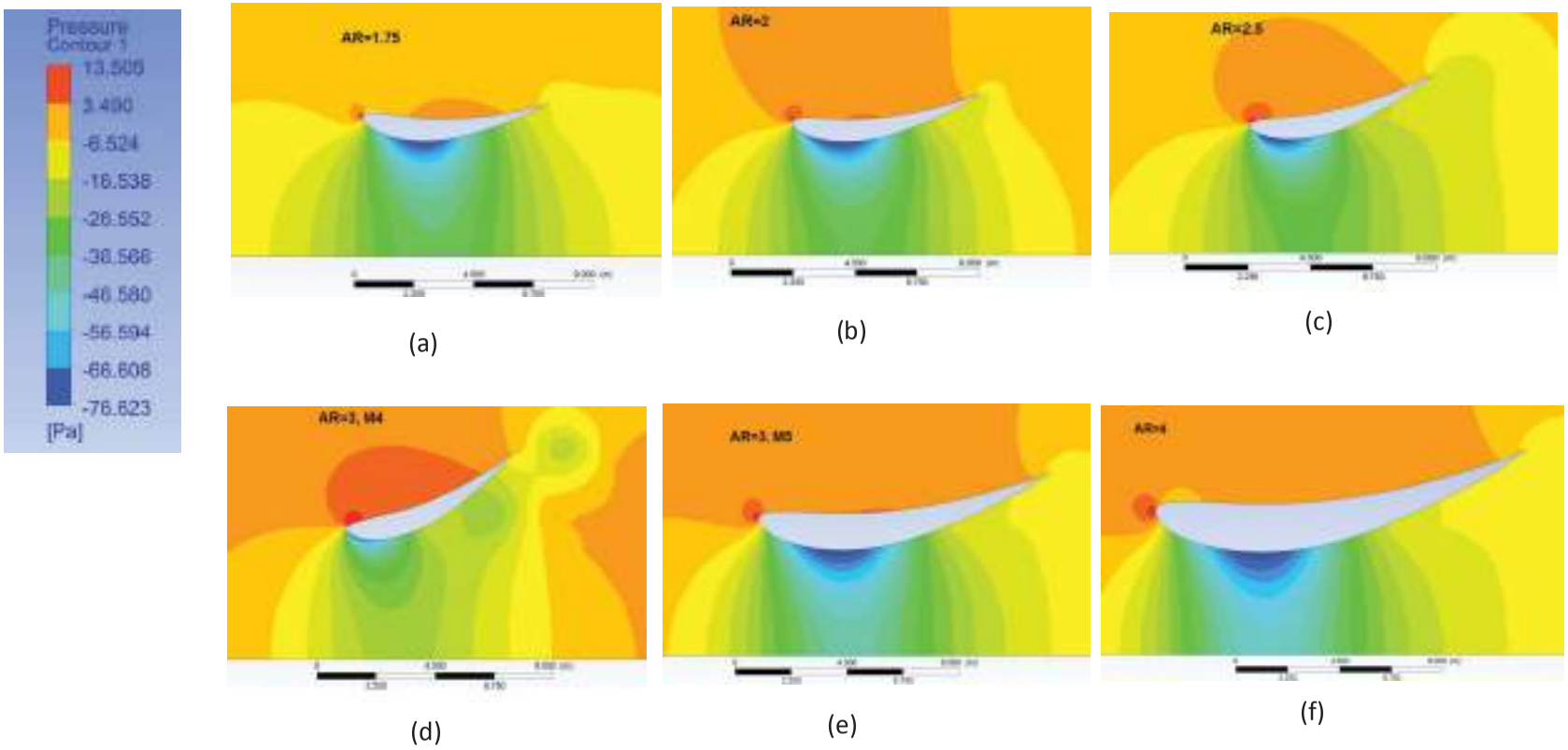

Figure A.8 Pressure contours for the models: (a)M2, Area ratio (AR=1.75), (b) M1,AR=2 , (c) M3,AR=2.5, (d) M4, AR=3, (e) M5, AR=3, (f) M6, AR=4

Appendix D Numerical Analysis Comparison for Grid Convergence

Table A.3 Grid convergence of model M1

			Grid1	Grid2	Grid3
Model M1	Final Gridding	# of Nodes	51584	58432	58705
		# of Elements	100021	113698	114244
		Run Time (min)	22	14.28	18.65
		# of Iterations	2000	1472	2000
	Results Comparison Numerical results	AF0	1.91 (1.57%)	1.9 (1.058%)	1.88
		γ	1.16 (1.301%)	1.13 (1.318%)	1.145
		C_d	0.35 (0.85%)	0.34 (2.05%)	0.347

Table A.4 Grid convergence of model M2

			Grid1	Grid2	Grid3
Model M2	Final Gridding	# of Nodes	51141	52757	69676
		# of Elements	99834	101704	135072
		Run Time (min)	>12	9.1	16.86
		# of Iterations	>2000	1423	1822
	Results Comparison Numerical results	AF0	1.83 (1.09%)	1.82 (1.105%)	1.81
		γ	1.194 (0.33%)	1.1996 (0.803%)	1.194
		C_d	0.235 (8.34%)	0.2319 (%7.115)	0.2154

Table A.5 Grid convergence of model M3

			Grid1	Grid2	Grid3
Model M3	Final Gridding	# of Nodes	48556	51624	58463
		# of Elements	99880	100100	113760
		Run Time (min)	>20	17	>32
		# of Iterations	>2000	1083	>2000
	Results Comparison Numerical results	AF0	1.785 (0.279%)	1.78 (0.56%)	1.79
		γ	1.06 (1.9%)	1.03 (0.966%)	1.04
		C_d	0.57 (1.59%)	0.5588 (0.392%)	0.561

Table A.6 Grid convergence of model M4

			Grid1	Grid2	Grid3
Model M4	Final Gridding	# of Nodes	63815	67675	73650
		# of Elements	125630	130868	145301
		Run Time (min)	>17	19	>24
		# of Iterations	>2500	2153	>2500
	Results Comparison Numerical results	AF0	1.77 (1.709%)	1.742 (0.114%)	1.74
		γ	0.94 (2.15%)	0.9077 (1.34%)	0.92
		C_d	0.61 (1.154%)	0.6 (0.4988%)	0.603

Table A.7 Grid convergence of model M5

			Grid1	Grid2	Grid3
Model M5	Final Gridding	# of Nodes	59989	71265	75325
		# of Elements	128008	139385	140210
		Run Time (min)	>25	20	>30
		# of Iterations	>2000	2008	>2500
	Results Comparison Numerical results	AF0	2.15 (2.83%)	2.11 (0.95%)	2.09
		γ	1.01 (2%)	1 (1.005%)	0.99
		C_d	0.51 (3.468%)	0.539 (2.06%)	0.528

Table A.8 Grid convergence of model M6

			Grid1	Grid2	Grid3
Model M6	Final Gridding	# of Nodes	69991	73863	77725
		# of Elements	139390	144603	153450
		Run Time (min)	>25	22	>30
		# of Iterations	>2500	2100	>2500
	Results Comparison Numerical results	AF0	2.175 (1.15%)	2.16 (0.46%)	2.15
		γ	0.88 (1.6%)	0.868 (0.23%)	0.866
		C_d	0.6028 (1.85%)	0.5908 (0.152%)	0.5917